EVAPORATION OF 2-DIMENSIONAL BLACK HOLES

FETHI M RAMAZANOĞLU

A DISSERTATION

PRESENTED TO THE FACULTY

OF PRINCETON UNIVERSITY

IN CANDIDACY FOR THE DEGREE

OF DOCTOR OF PHILOSOPHY

RECOMMENDED FOR ACCEPTANCE

BY THE DEPARTMENT OF

PHYSICS

ADVISER: FRANS PRETORIUS

JUNE 2012

Abstract

We present a detailed analysis of results from a new study of the quantum evaporation of Callan-Giddings-Harvey-Strominger (CGHS) black holes within the mean-field approximation. The CGHS model is a two dimensional model of quantum gravity which has been extensively investigated in the last two decades. Moreover, Ashtekar, Taveras and Varadarajan have recently proposed a solution to the information loss paradox within the context of this model, which has rekindled the interest in it. However, many aspects of black hole evaporation in this model has been overlooked because of lack of a solution for black holes with macroscopic mass. We show that this was due to, in part, limited numerical precision and, in part, misinterpretation of certain properties and symmetries of the model. By addressing these issues, we were, for the first time, able to numerically evolve macroscopic-mass black hole spacetimes of the CGHS model within the mean-field approximation, up to the vicinity of the singularity.

Our calculations show that, while some of the assumptions underlying the standard evaporation paradigm are borne out, several are not. One of the anticipated properties we confirm is that the semi-classical space-time is asymptotically flat at right future null infinity, $\mathcal{I}_{\mathrm{R}}^{+}$, yet incomplete in the sense that null observers reach a future Cauchy horizon in finite affine time. Unexpected behavior includes that the Bondi mass traditionally used in the literature can become negative even when the area of the horizon is macroscopic; an

improved Bondi mass remains positive until the end of semi-classical evaporation, yet the final value can be arbitrarily large relative to the Planck mass; and the flux of the quantum radiation at $\mathcal{I}_R^+$ is non-thermal even when the horizon area is large compared to the Planck scale. Furthermore, if the black hole is initially macroscopic, the evaporation process exhibits remarkable universal properties, which offer problems to attack to the mathematical relativity and geometric analysis communities. Our results also provide support for the full quantum scenario developed by Ashtekar et al.

Acknowledgements

I should start by thanking my advisor Frans Pretorius, who always had a solution whenever the progress of my research was stalled by a bug in the code, or some misconception about general relativity. His easygoing approach was crucial for me to get used to numerical calculations. His patience during the long period where our initial numerical attempts at solving the CGHS model failed gave me the opportunity to finally bring together the right tools to crack the problem, which eventually led to this thesis. His philosophy of putting physics, not the method (in our case numerics), to the forefront will continue to shape my research style in the future.

This work would not be possible without the guidance of Abhay Ashtekar. He reminded me how fruitful the interplay of numerical and analytical methods could be, and gave me the chance to work on a problem at the intersection of quantum mechanics and general relativity, a field I have always been fond of.

Steve Adler was my advisor at the beginning of my graduate career, and taught me a great deal about the foundations of quantum mechanics. I thank him for his mentorship and his continued support even after I changed my area of study. He was kind enough to be a reader for my dissertation.

My group mates Hans Bantilan, Theodor Brasoveanu and Will East made our research environment more lively. I need to mention Will a second time, he was always patient with

To my parents and teachers

Relation to Previous Work

Parts of Chapter 1 and Chapter 4, and most of Chapter 3 are based on [1], whose basic results can also be found in [2]. Chapter 2 is based on [3].

Contents

Chapter 1

Introduction

Here, we present the preliminary information that provides the context for the following chapters. We start with a summary of black hole evaporation and information loss as it was introduced by Hawking. After a short section that demonstrates how results in two dimensions can be related to the 4-dimensional case, we continue with the basics of the Callan-Giddings-Harvey-Strominger (CGHS) model, the specific 2-dimensional model we use to analyze black hole evaporation. We start with the classical action, and then have an interlude in Sec. 1.3.2 to explain our motivations in examining this model, and to give a summary of our results. This section is placed so that, readers from all backgrounds can have an idea about the basics of the black hole evaporation and gravity in two dimensions by this point. We continue our exposition of the CGHS model by providing a combination of previously known results and our novel contributions, to set the scene for the main discussion. Lastly, we have a second look at black hole evaporation, this time from an alternative direction that is better adapted to our work.

1.1   Black Hole Evaporation and Information Loss

Almost four decades ago, Hawking demonstrated that black holes can radiate particles with a thermal spectrum and evaporate away [4]. This result was against the common intuition

about black holes, and has led to tremendous amount of work in quantum mechanics, general relativity, and many theories which aspire to combine the two. In this section, we will give a summary of Hawking's original results. Today, Hawking radiation and related phenomena are standard parts of the curriculum of quantum field theory in curved spacetime courses, and pedagogical expositions can be found at introductory [5] or advanced [6] levels. We direct the interested reader to these sources, and will give a mostly conceptual explanation of the information loss problem.
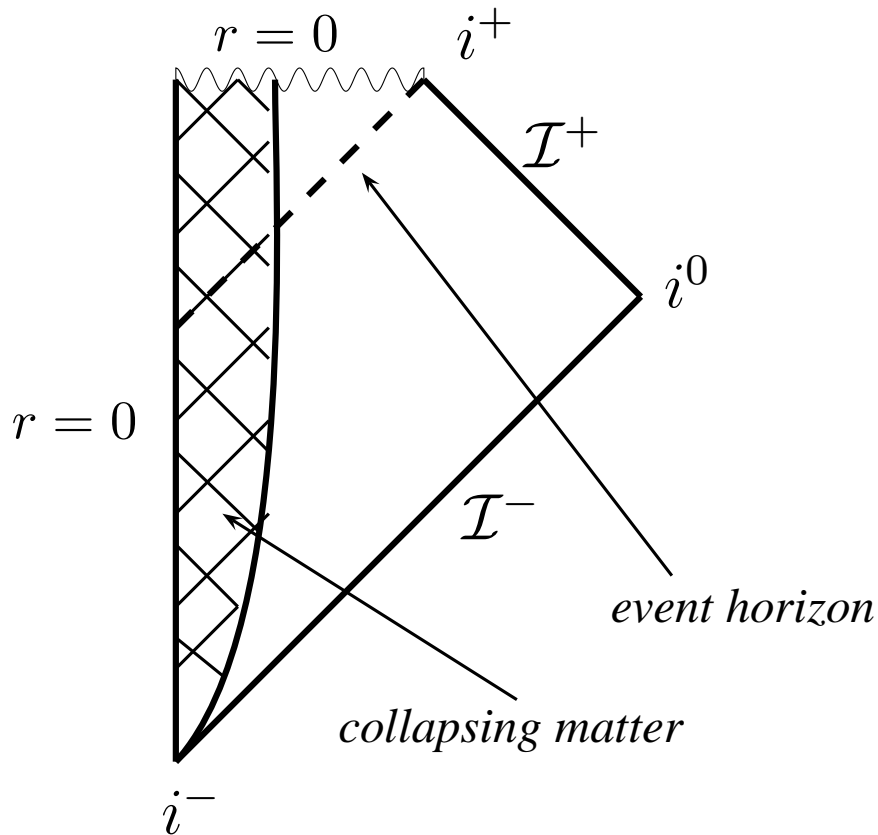
Figure 1.1: Penrose diagram of a black hole that forms from collapsing energy. The shaded region is the collapsing energy, outside of which we have a Schwarzschild solution. $i^{\pm}$ are the past and future time-like infinities, i^0 is the spacelike infinity, and $\mathcal{I}^{\pm}$ are the past and future null infinities. The past image of $\mathcal{I}^+$ does not cover all of the spacetime, which means there are trapped surfaces. The event horizon, the boundary of the trapped region is shown by a dashed line. Singularity at $r = 0$ is hidden behind the event horizon.

Following the original calculation [4], we begin by considering a spacetime where energy collapses to form a black hole. In the case of the spherically symmetric collapse,

the Penrose diagram for this spacetime is given in Fig. 1.1. On this fixed curved space-time, consider a quantum field ϕ satisfying $\nabla^a \nabla_a \phi = 0$ (∇ being the covariant derivative), which has a mode expansion

$$\phi = \sum_i \left(f_i a_i + \bar{f}_i a_i^\dagger \right) \tag{1.1}$$

where f_i satisfy the wave equation and form a complete orthonormal base at the past null infinity $\mathcal{I}^-$. $\mathcal{I}^-$ is a Cauchy surface, once we know the initial data on it, we know ϕ everywhere. Hence, Eq. 1.1 can be used to express ϕ everywhere.

We cannot repeat the exact same procedure for $\mathcal{I}^+$, since it is not a Cauchy surface. This is because interior of the event horizon is not in the past image of $\mathcal{I}^+$, hence we need to know the data on the event horizon as well. If we choose the solutions of the wave equation p_i that are purely outgoing, i.e. with no Cauchy data on event horizon, and q_i that area purely ingoing, i.e. they have zero Cauchy data on $\mathcal{I}^+$, one can say

$$\phi = \sum_i \left(p_i b_i + \bar{p}_i b_i^\dagger + q_i c_i + \bar{q}_i c_i^\dagger \right) \tag{1.2}$$

outside the horizon. Since either of the mode expansions is valid, we can express p_i in terms of f_i, and

$$b_i = \sum_j \left(\alpha_{ij} a_j - \bar{\beta}_{ij} a_j^\dagger \right) \tag{1.3}$$

for some α_{ij} and β_{ij}. The state with no particles coming in from $\mathcal{I}^-$ is defined as

$$a_i |0\rangle = 0 \quad \text{for all i} . \tag{1.4}$$

On the other hand, this same state is not necessarily annihilated by other annihilation operators associated with a different mode expansion. Specifically,

$$\langle 0 | b_i^\dagger b_i | 0 \rangle = \sum_j |\beta_{ij}|^2 . \tag{1.5}$$

3

which is in general nonzero. Remember that b_i can be interpreted as the annihilation operator from the point of view of $\mathcal{I}^+$, and $b_i^\dagger b_i$ is the number counting operator for the mode i. This has a simple interpretation: in curved spacetime, vacuum is observer dependent. Even if we start with a vacuum state in the past, this may lead to a state with particles in the asymptotic future.

When $|\beta_{ij}|^2$ is calculated, the expected number of particles with frequency ω observed in the distant future is given by,

$$\langle \hat{n}_\omega \rangle = \frac{\Gamma(\omega)}{e^{\frac{2\pi\omega}{\hbar\kappa}} - 1} \tag{1.6}$$

where κ is the surface gravity of the black hole. This is the emission spectrum of a black body with temperature $\frac{\hbar\kappa}{2\pi}$. $\Gamma(\omega)$ is called the *greybody factor* and can be thought of accounting for the fact that the radiation can scatter from the spacetime curvature and fall back into the black hole. The exact expression for $\Gamma(\omega)$ as well as slight modifications to the formula when charge and angular momentum are introduced are not crucial for our discussion and can be found in the detailed treatments we mentioned.

In 4 spacetime dimensions κ is inversely proportional to M, the mass of the black hole. Even though we fixed the background metric and ignored the backreaction, in a more realistic treatment, the black hole will lose mass due to Hawking radiation, and its temperature will rise. Radiated power will increase, leading to a runaway process where finally the black hole and the event horizon disappears in finite proper time. At this point, we are left with thermal radiation, which does not carry any information, however, in general, the matter that formed the black hole in the first place carried some information. Thus, *information is lost in the evolution of a black hole space time*. In both quantum field theory and general relativity, evolution is unitary, but something has been broken when we tried to combine the two. This is the celebrated *information loss problem*, which is sometimes also known as the information loss "paradox".

Information may very well be lost since we do not have an exact theory of quantum gravity, but many physicists found this possibility hard to digest and have been looking for

places where the missing information could have gone. There is no agreed upon resolution so far.

We should perhaps mention one possible shortcoming of Hawking's calculation: ignoring the backreaction. After all, information loss arises when the black hole shrinks, which is not explicitly captured in the fixed background calculation we summarized. However, this was foreseen in [4], where it is argued that the semiclassical picture of a fixed curved spacetime should hold until the curvature reaches the Planck scale. This would mean that, if quantum gravity or beyond-the-leading semiclassical corrections are to resolve the issue, they can do so only at the very last stages of the life of the black hole. By this point, almost all of the mass is lost, hence it is hard to imagine how such a small remnant can hold all the information about the matter that originally collapsed to form a macroscopic black hole.

We will give another short summary of black hole evaporation at the end of this chapter, in Sec. 1.4, which will be adapted to the 2-dimensional case.

1.2 General Relativity in Spherical Symmetry

In two dimensions, the Riemann tensor has only one independent component (e.g. R_{1010}) due to its inherent symmetries, which can be captured by the Ricci scalar

$$R_{abcd} = R \left(g_{ac} g_{bd} - g_{ad} g_{bc} \right) \tag{1.7}$$

A direct consequence of this fact is an Einstein tensor that vanishes identically

$$G_{ab} = R_{ab} - \frac{1}{2} R g_{ab} = 0 \, . \tag{1.8}$$

Hence, Einstein equations are not useful in two dimensions. However, there is no shortage of work on gravity in two dimensions, which go back many decades (for example, see [7] for a collection of different approaches).

Our main aim in analyzing two dimensional models is gaining insight into the 4-dimensional case, and an important case to connect the two is the spherically symmetric ($S-$wave) sector of the Einstein-Klein-Gordon system. Consider the spherical collapse of a massless scalar field f in 4 space-time dimensions. Mathematically, it is convenient to write the coordinate r which measures the physical radius of metric 2-spheres as $r = e^{-\phi}/\kappa$ where κ is a constant with dimensions of inverse length. The space-time metric $^4g_{ab}$ can then be expressed as

$$^4g_{ab} = \underline{g}_{ab} + r^2 s_{ab} := \underline{g}_{ab} + \frac{e^{-2\phi}}{\kappa^2} s_{ab}, \tag{1.9}$$

where s_{ab} is the unit 2-sphere metric and $\underline{g}_{ab}$ is the 2-metric in the r-t plane. In terms of these fields, the action for this Einstein-Klein-Gordon sector can be written as

$$
\begin{aligned}
\tilde{S}(\underline{g}, \phi, f) &= \frac{1}{8\pi\, G_4} \frac{4\pi}{\kappa^2} \int d^2x \sqrt{|\underline{g}|}\, e^{-2\phi}\, (\underline{R} + \mathbf{2\nabla^a\phi\nabla_a\phi} \\
&+\ \mathbf{2e^{-2\phi}\kappa^2}) - \tfrac{1}{2} \int d^2x \sqrt{|\underline{g}|}\, \mathbf{e}^{-\phi}\nabla^a f \nabla_a f
\end{aligned} \tag{1.10}
$$

where G_4 is the 4-dimensional Newton's constant, ∇ is the derivative operator and $\underline{R}$ the scalar curvature of the 2-metric $\underline{g}_{ab}$. The significance of the bold faced terms will be explained in the next section. The gravitational field is now coded in a 2-metric $\underline{g}_{ab}$ and a dilaton field ϕ, and the theory has a 2-dimensional gravitational constant G of dimension $[ML]^{-1}$ in addition to the constant κ of dimension $[L]^{-1}$ (κ^2 is sometimes regarded as the cosmological constant).[1]

An important connection to four dimensions from this effectively two dimensional model arises when we note that $e^{-2\phi}$ measures the area of spheres. Hence, once can deduce the location of the apparent horizon by the rate of change of ϕ. We will use these facts in the following analysis of the CGHS model as well.

---

[1]In this paper we set $c = 1$ but keep Newton's constant G and Planck's constant $\hbar$ free. Note that since $G\hbar$ is a *Planck number* in 2 dimensions, setting both of them to 1 is a physical restriction.

1.3 The Callan-Giddings-Harvey-Strominger Model

The Callan-Giddings-Harvey-Strominger (CGHS) model [8] is a 2-dimensional model of quantum gravity which has attracted attention due to the fact that it has black hole solutions with many of the qualitative features of four dimensional black holes, while being technically easier to investigate. Various properties of black holes in this model, and other models inspired by it, have been studied extensively using analytical and numerical methods [9, 10, 11]. Detailed pedagogical reviews can be found in [12].

In this section, we will start with the classical CGHS action and continue with the semiclassical results some of which were long known and some of which were dicovered by us [1] . CGHS model has recently come to the forefront in the investigation of the black hole information loss problem by Ashtekar, Taveras and Varadarajan [13], whose approach we follow in our notation and definition of variables.

1.3.1 The Classical CGHS Model

The CGHS action is given by [8]:

$$S(\underline{\mathbf{g}}, \phi, f) = \frac{1}{G} \quad \int d^2x \sqrt{|\underline{\mathbf{g}}|}\, e^{-2\phi}\left(\underline{\mathbf{R}} + 4\,\nabla^a\phi\nabla_a\phi + 4\kappa^2\right)$$
$$- \sum_{i=1}^{N} \tfrac{1}{2}\int d^2x \sqrt{|\underline{\mathbf{g}}|}\,\nabla^a f^{(i)}\nabla_a f^{(i)}\,. \tag{1.11}$$

where ∇ and $\underline{\mathbf{R}}$ are the covariant derivative operator and the scalar curvature of the 2-metric $\underline{\mathbf{g}}_{ab}$ respectively, ϕ is a dilatonic field, and f^i are N identical massless scalars. Note that this action is closely related to the one for the $S-$wave sector of general relativity and some comments are due on this similarity. The only difference is in some coefficients which appear bold faced in Eq. 1.10. This is why one expects that analysis of the CGHS model should provide useful intuition for evaporation of spherically symmetric black holes in 4 dimensions, which is confirmed by further study.

7

On the other hand, the two theories do differ in some important ways, which will be discussed in Sec. 3.5. Here, we only note one: since the dilaton field does not appear in the scalar field action of Eq. 1.11, dynamics of f decouples from that of the dilaton. This leads to analytical solutions for the classical CGHS equations, which is one of the reasons we investigate this model.

Now, since our space-time is topologically $\mathbb{R}^2$, the physical 2-metric $\underline{g}_{ab}$ is conformally flat. We can thus fix a fiducial flat 2-metric η^{ab} and write $\underline{g}^{ab} = \underline{\Omega}\eta^{ab}$, thereby encoding the physical geometry in the conformal factor $\underline{\Omega}$ and the dilaton field ϕ.

We start with the equation of motion for the f fields[2], which is simply the wave equation. Since the wave equation is conformally invariant,

$$\Box_{(\underline{g})} f = 0 \quad \Leftrightarrow \quad \Box_{(\eta)} f = 0 \,, \tag{1.12}$$

f is only subject to the wave equation in the fiducial flat space which can be easily solved, without any knowledge of the physical geometry governed by $(\underline{\Omega}, \phi)$. *This is a key simplification which is not shared by the scalar field f in the spherically symmetric gravitational collapse described by Eq. 1.10.* Denote by $z^{\pm}$ the advanced and retarded null coordinates of η so that $\eta_{ab} = 2\partial_{(a} z^{+} \, \partial_{b)} z^{-}$. Then a general solution to Eq. 1.12 on the fiducial Minkowski space (M^{o}, η) is simply

$$f(z^{\pm}) = f_{+}(z^{+}) + f_{-}(z^{-}) \tag{1.13}$$

where $f_{\pm}$ are arbitrary well behaved functions of their arguments. In the classical CGHS theory, one sets $f_{-} = 0$ and focuses on the gravitational collapse of the left moving mode f_{+}. As one might expect, the true degree of freedom lies only in f_{+}, i.e., f_{+} completely determines the geometry. But in the classical CGHS model, there is a further unexpected simplification: *the full solution can be expressed as an explicit integral involving f_{+}!*

---

[2] since all $f^{(i)}$ are identical, we will sometimes suppress the index

For later purposes, following [13], let us set

$$\underline{\Phi} := e^{-2\phi}$$

and introduce a new field $\underline{\Theta}$ via

$$\underline{\Theta} = \underline{\Omega}^{-1}\underline{\Phi} \quad \text{so that} \quad g^{ab} = \underline{\Theta}^{-1}\underline{\Phi}\,\eta^{ab}$$

Then the geometry is completely determined by the pair of fields $\underline{\Theta}, \underline{\Phi}$. The field equations obtained by varying Eq. 1.11 are given by

$$\partial_+\,\partial_-\,\underline{\Phi} + \kappa^2\underline{\Theta} = 0$$

$$\underline{\Phi}\partial_+\,\partial_-\ln\underline{\Theta} = 0\,. \tag{1.14}$$

Moreover, we also have constraint equations

$$-\partial_+^2\,\underline{\Phi} + \partial_+\,\underline{\Phi}\partial_+\,\ln\underline{\Theta} = GT_{++}$$

$$-\partial_-^2\,\underline{\Phi} + \partial_-\,\underline{\Phi}\partial_-\,\ln\underline{\Theta} = GT_{--}, \tag{1.15}$$

where T_{ab} is the scalar field stress-energy tensor. Constraint equations can be viewed as fixing the gauge condition $g_{++} = g_{--} = 0$. They are only needed to be imposed for the initial data, and are then preserved by the evolution equations.

These equations can be solved to express $\underline{\Theta}, \underline{\Phi}$ directly in terms of f_+. The resulting expressions for $\underline{\Theta}$ and $\underline{\Phi}$ are simpler in terms of 'Kruskal-like' coordinates $x^\pm$ given by

$$\kappa x^+ = e^{\kappa z^+}, \quad \text{and} \quad \kappa x^- = -e^{-\kappa z^-}\,. \tag{1.16}$$

Given any regular f_+, the full solution to the classical CGHS equations can now be
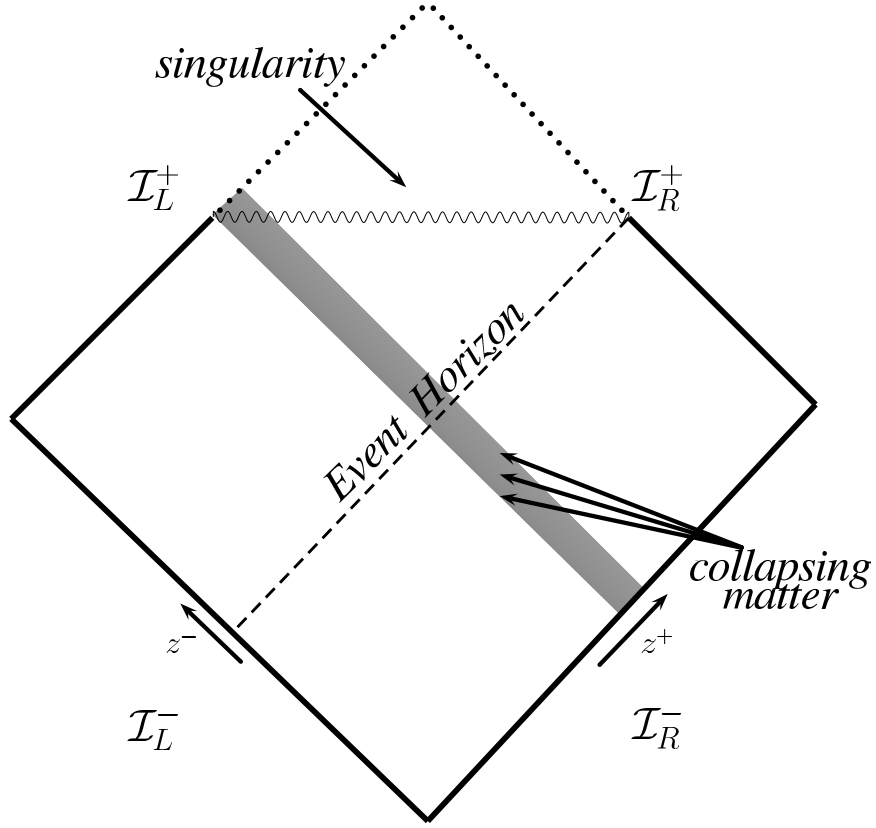
Figure 1.2: Penrose diagram of the CGHS black hole formed by the gravitational collapse of a left moving field f_+. The physical space-time is that part of the fiducial Minkowski space which is to the past of the space-like singularity.

written as

$$
\begin{aligned}
\underline{\Theta} &= -\kappa^2 x^+ x^- \\
\underline{\Phi} &= \underline{\Theta} - \frac{NG}{2}\int_0^{x^+} \mathrm{d}\bar{x}^+ \int_0^{\bar{x}^+} \mathrm{d}\bar{\bar{x}}^+ \ (\partial f_+/\partial \bar{\bar{x}}^+)^2 \,.
\end{aligned}
\tag{1.17}
$$

Note that, given any regular f, the fields $(\underline{\Theta}, \underline{\Phi})$ of Eq. 1.17 that determine the geometry are also regular everywhere on the fiducial Minkowski manifold M^o.

How can the solution then represent a black hole? It turns out that, for any regular f_+, the field $\underline{\Phi}$ of Eq. 1.17 vanishes along a space-like line ℓ_s. Along ℓ_s then, $\underline{\mathrm{g}}^{ab}$ vanishes, whence the covariant metric $\underline{\mathrm{g}}_{ab}$ fails to be well-defined. It is easy to verify that the Ricci scalar of $\underline{\mathrm{g}}_{ab}$ diverges there. This is the singularity of the physical metric $\underline{\mathrm{g}}$. *The physical*

space-time $(M, \mathbf{g}_{ab})$ *occupies only that portion of* M^o *which is to the past of this singularity* (see Fig. 1.2).

But does ℓ_s represent a *black hole* singularity? It is easy to check that $(M, \underline{\mathbf{g}}_{ab})$ admits a smooth null infinity $\mathcal{I}$ which has 4 components. The reason for the diamond-like conformal diagram rather than the triangular diagrams familiar from 4 dimensions is easy: In 4 dimensions, we usually suppress the angular coordinates, and the spatial coordinate r is in the interval $[0 \, \infty)$, on the other hand, in an intrinsically two dimensional model, the spatial coordinate is in the interval $(-\infty \, \infty)$ and can reach to two different infinities. $\mathcal{I}_{\mathrm{L}}^-$ and $\mathcal{I}_{\mathrm{R}}^-$ coincide with the corresponding $\mathcal{I}_{\mathrm{L}}^{o-}$ and $\mathcal{I}_{\mathrm{R}}^{o-}$ of Minkowski space-time (M^o, η) while $\mathcal{I}_{\mathrm{L}}^+$ and $\mathcal{I}_{\mathrm{R}}^+$ are proper subsets of the Minkowskian $\mathcal{I}_{\mathrm{L}}^{o+}$ and $\mathcal{I}_{\mathrm{R}}^{o+}$. Nonetheless, $\mathcal{I}_{\mathrm{R}}^+$ *is complete with respect to the physical metric* $\mathbf{g}_{ab}$ *and its past does not cover all of* M. Thus, there is indeed an event horizon with respect to $\mathcal{I}_{\mathrm{R}}^+$ hiding a black hole singularity. However, unfortunately $\mathcal{I}_{\mathrm{L}}^+$ is *not* complete with respect to $\underline{\mathbf{g}}_{ab}$. Therefore, strictly speaking we cannot even ask[3] if there is an event horizon —and hence a black hole— with respect to $\mathcal{I}_{\mathrm{L}}^+$! Fortunately, it turns out that for the analysis of black hole evaporation —and indeed for the issue of information loss in full quantum theory— only $\mathcal{I}_{\mathrm{R}}^+$ is relevant. *To summarize then, even though our fundamental mathematical fields* $(\underline{\Theta}, \underline{\Phi})$ *are everywhere regular on full* M^o, *a black hole emerges because physics is determined by the Lorentzian geometry of* $\mathbf{g}$.

To make our case more concrete, let us examine the case of a shock wave pulse given by

$$\frac{N}{2}(\partial f_+ / \partial x^+)^2 = M \delta(x^+ - x_0^+) \tag{1.18}$$

which leads to

$$\underline{\Phi} = \underline{\Theta} - \frac{GM}{\kappa} \left(\kappa x^+ - 1 \right) H \left(\kappa x^+ - 1 \right) \tag{1.19}$$

where H is the step function and where we chose $\kappa x_0^+ = 1$ (simply by shifting the coordi-

---

[3]Even in 4 dimensions, the black hole region is defined as $\mathcal{B} := M \setminus J^-(\mathcal{I}^+)$ *provided* $\mathcal{I}^+$ *is complete*. If we drop the completeness requirement, even Minkowski space would admit a black hole! See, e.g., [14].

nates such that $z_0^+ = 0$). The conformal factor $\underline{\Omega}$ vanishes when

$$\kappa x^+ = \frac{GM}{\kappa}\left(1 - \frac{1}{\kappa x^+}\right) \tag{1.20}$$

leading to the singularity in Fig. 1.2.

To analyze the Hawking evaporation, we once more change the coordinates to

$$e^{\kappa \underline{y}^+} = e^{\kappa z^+}$$
$$e^{\kappa \underline{y}^-} = e^{\kappa z^-} - \frac{GM}{\kappa} \tag{1.21}$$

which are the affine coordinates on $\mathcal{I}_R^+$, for which the metric is flat as $\underline{y}^+ \to \infty$. We start with the expression

$$\langle 0_z| : T_{--} :_z |0_z\rangle = 0 \ , \tag{1.22}$$

where $|0_z\rangle$ is the vacuum which is annihilated by the annihilation operators in z^- coordinates, and $: T_{--} :_z$ is the operator of the normal ordered energy-momentum tensor of the f field. The effect of a change of coordinates is given by [12]

$$: T_{--} :_{\underline{y}} = \left(\frac{dz^-}{d\underline{y}^-}\right)^2 : T_{--} :_z - \frac{N\hbar}{12}\left(\frac{dz^-}{d\underline{y}^-}\right)^{3/2}\left(\frac{d}{dz^-}\right)^2\left(\frac{dz^-}{d\underline{y}^-}\right)^{1/2} \tag{1.23}$$

which finally leads to

$$F^{\text{Haw}} = \langle 0_z| : T_{--} :_{\underline{y}} |0_z\rangle = \frac{N\hbar\kappa^2}{48}\left[1 - \left(1 + \frac{GM}{\kappa}e^{\kappa\underline{y}^-}\right)^{-1}\right] \ , \tag{1.24}$$

The straightforward interpretation of this expression is that if we send in the vacuum state, from $\mathcal{I}_L^-$ prepared with respect to the affine coordinates there, $z^\pm$, this will be interpreted as a flux of energy by an observer on $\mathcal{I}_R^+$, the Hawking radiation. The details of the fact that this flux is thermal and an alternative derivation of the expression for the flux through the conformal anomaly can be found in [12]. Note that this flux is constant at late

times due to the fact that the surface gravity of a black hole in our 2-dimensional model is an absolute constant. This is in contrast to the case in 4 dimensions, where surface gravity increases with decreasing black hole mass.

Although a black hole does result from gravitational collapse in the CGHS model, it follows from the explicit solution Eq. 1.17 that one does not encounter all the rich behavior associated with the classical spherical collapse in 4 dimensions. In particular there are no critical phenomena [15, 16], essentially because there is no threshold of black hole formation: a black hole results no matter how weak the infalling pulse f_+ is. However, the situation becomes more interesting even in this simple model once one allows for quantum evaporation and takes into account its back reaction.

1.3.2   Motivation and Outline of the Results

Now that we have an idea of black hole evaporation and gravity in two dimensions, it is a good time to give a summary of our results. The basic idea, as we will show in the next chapter, is adding the leading order corrections to the fixed-background evaporation calculation of the CGHS model, and investigating the changes introduced by this. We will see that, at this semiclassical level, also called the mean-field approximation (MFA) level, our job is still solving two coupled partial differential equations similar to Eq. 1.14, but this time with non-vanishing right hand sides, thus, we will not be working with quantum states except for a few instances where we give some conceptual explanations.

No closed form solution is known for the CGHS evolution equations at the MFA level, and we will be led to use numerical methods. Our work is the final one in a long line of numerical studies, but all past work had the shortcoming of not being able to analyze macroscopic-mass black holes, and for the most part, not being aware of the distinction between the macroscopic and microscopic-mass regimes, which we will explain shortly. To make this distinction clear, we first give further analytic analysis of the CGHS equations, and clarify certain misconception in the literature in sections 1.3.3, 1.3.4 and 1.3.5. In these

13

sections, we also give some novel results that we later use to extract information about the semiclassical spacetime, once we have our numerical solution. We have seen in the previous chapter that, the classical CGHS model is considerably simpler than the spherically symmetric sector of the 3+1-dimensional Einstein-Klein-Gordon system, which was an initial motivation to work on it. Even with these simplifications, at the MFA level, solving the equations numerically and capturing all the important physics is a very challenging task. We spend a whole chapter, Chapter. 2, to give the details of our methods and explain why we needed them.

Most of the the physical results that we extract from the numerical solution are in Chapter. 3. One major result we should mention is the fact that, at the MFA level, the standard black hole evaporation paradigm seems to be broken (Sec. 3.3). The radiation from the black hole is not thermal, even at times not close to the end-point of the singularity. $\mathcal{I}_R^+$ is not complete, which manifests itself with the fact that the affine parameter $\underline{y}^+$ is finite at the end-point of the singularity (see Eq. 1.21 for contrast). Overall, the picture is in close agreement with the information loss resolution scenario of Ashtekar et al [13], which we summarize in Sec. 1.4. We have also discovered a phenomena we named *universality*, which is the fact that as long as the black hole forms *promptly* and the infalling energy is macroscopic, the physics on $\mathcal{I}_R^+$, hence the radiated energy, is independent of the shape of the infalling energy profile, and only depends on the total infalling mass. Moreover, physics on $\mathcal{I}_R^+$ is identical near the end-point of the singularity, even for different initial-mass black holes. In short, all macroscopic black holes eventually behave in the same *universal* way from the point of view of an observer on $\mathcal{I}_R^+$. Aside from these major points, we also clarify the definition of the black hole mass and radiated energy in the CGHS model, and describe the nature of the Cauchy horizon at the end-point of the singularity. We should mention that not all of our findings are different from the expectations in the field, and we also report, for example, the asymptotic flatness of the metric near the future null infinity (Sec. 3.2)

In Chapter. 4, we will give a final summary and interpret our results further, specifically,

14

we will try to establish connections to the 3+1-dimensional case. Universality, the way we have just summarized it, gives the impression that the infalling information is indeed lost in the radiated energy from the black hole. However, we also claimed that our results support the resolution of the information loss paradox. A careful analysis of these two issues, and a discussion of their separate nature in the CGHS model will be discussed in Sec. 4.2. Here we will only mention that, the analysis is based on the differences of the causal structures of 1+1-dimensional (Fig.1.1) and 3+1-dimensional (Fig. 1.2) spacetimes. This discussion also gives us a guide about how to approach the spherically symmetric sector of the 3+1-dimensional spacetime in future studies.

1.3.3   The Semi-Classical CGHS Model

To incorporate back reaction, one can use semi-classical gravity where matter fields are allowed to be quantum but geometry is kept classical. Here, we will implement this idea using the mean field approximation of [13, 17] where one ignores the quantum fluctuations of geometry —i.e., of quantum fields $(\hat{\Theta}, \hat{\Phi})$— but keeps track of the quantum fluctuations of matter fields. The validity of this approximation requires a large number of matter fields $\hat{f}^{(i)}$, with $i = 1, \ldots N$ (whence it is essentially the large N approximation [8, 12]). Then, there is a large domain in space-time where quantum fluctuations of matter can dominate over those of geometry. Back reaction of the quantum radiation modifies classical equations with terms proportional to $NG\hbar$. However, dynamics of the physical metric g is again governed by PDEs on classical fields, (Θ, Φ), which we write without an under-bar to differentiate them from solutions $(\underline{\Theta}, \underline{\Phi})$ to the classical equations ($N\hbar = 0$). In the domain of applicability of the mean-field approximation, they are given by expectation values of the quantum operator fields: $\Theta = \langle\hat{\Theta}\rangle$ and $\Phi = \langle\hat{\Phi}\rangle$. The difference from the classical case is that the coefficients of the PDEs and components of the metric g_{ab} now contain $\hbar$.

In the mean-field approximation, we capture the idea that it is only the left moving modes of $\hat{f}^{(i)}$ that undergo gravitational collapse by choosing the initial state appropriately:
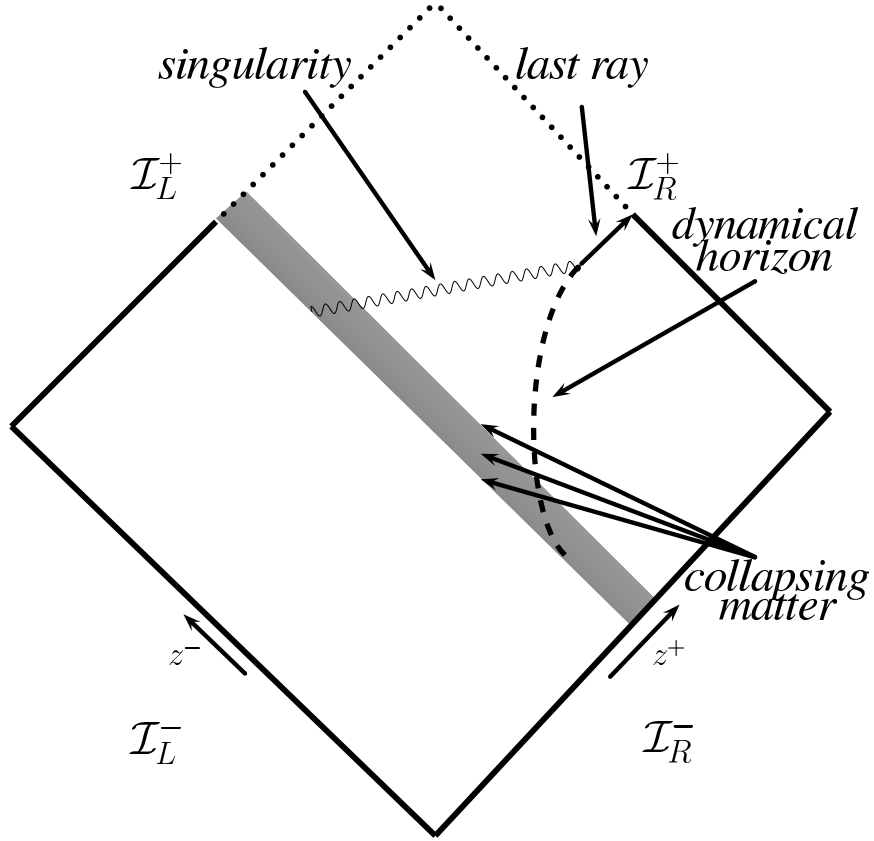
Figure 1.3: Penrose diagram of an evaporating CGHS black hole in the mean field approximation. Because of quantum radiation the singularity now ends in the space-time interior and does not reach $\mathcal{I}_{\mathrm{L}}^{+}$ or $\mathcal{I}_{\mathrm{R}}^{+}$(compare with Fig. 1.2.) Space-time admits a generalized dynamical horizon whose area steadily decreases. It meets the singularity at its (right) end point. The physical space-time in this approximation excludes a future portion of the fiducial Minkowski space (bounded by the singularity, the last ray and the future part of the collapsing matter).

we let this state be the vacuum state for the right moving modes $\hat{f}_{-}^{(i)}$ and a coherent state peaked at any given classical profile f_{+}^{o} for *each* of the N left moving fields $\hat{f}_{+}^{(i)}$. This specification at $\mathcal{I}^{-}$ defines a (Heisenberg) state $|\Psi\rangle$. Dynamical equations are obtained by taking expectation values of the quantum evolution equations for (Heisenberg) fields in this state $|\Psi\rangle$ and ignoring quantum fluctuations of geometry but not of matter. Technically, this is accomplished by substituting polynomials $P(\hat{\Theta}, \hat{\Phi})$ in the geometrical operators with polynomials $P(\langle\hat{\Theta}\rangle, \langle\hat{\Phi}\rangle) := P(\Phi, \Theta)$ of their expectation values. For the matter fields $\hat{f}^{(i)}$, on the other hand, one does not make this substitution; one keeps track of the quantum

16

fluctuations of matter. These lead to a conformal anomaly: While the trace of the stress-tensor of scalar fields vanishes in the classical theory due to conformal invariance, the expectation value of this trace now fails to vanish. Therefore equations of motion of the geometry acquire new source terms of quantum origin which modify its evolution.

To summarize, then, in the mean-field approximation the dynamical objects are again just smooth fields $f^{(i)}, \Theta, \Phi$ (representing expectation values of the corresponding quantum fields). While there are N matter fields, geometry is still encoded in the two basic fields Θ, Φ which determine the space-time metric g^{ab} via $g^{ab} = \Omega \eta^{ab} := \Theta^{-1} \Phi \, \eta^{ab}$. Dynamics of $f^{(i)}, \Theta, \Phi$ are again governed by PDEs but, because of the trace anomaly, equations governing Θ, Φ acquire quantum corrections which encode the back reaction of quantum radiation on geometry. More details can be found in [13].

The basic quantitative difference in the semiclassical case comes from the trace anomaly. In the classical theory, the trace of the energy-momentum tensor T^a_a vanishes. Due to one-loop quantum contributions, however, it is nonzero at the semi-classical level, and for N scalar fields is given by

$$\langle \hat{T}^a_a \rangle = \frac{N\hbar}{24} R \Rightarrow \langle \hat{T}_{+-} \rangle = \bar{N}\hbar \, \partial_+ \, \partial_- \ln \Phi \Theta^{-1} \, . \tag{1.25}$$

where R is the Ricci scalar and $\bar{N} = N/24$.

As in 4-dimensional general relativity (and the classical CGHS model), there are two sets of PDEs: Evolution equations and constraints which are preserved in time. As in the classical theory, it is simplest to fix the gauge and write these equations using the advanced and retarded coordinates $z^\pm$ of the fiducial Minkowski metric. The evolution equations are given by

$$\Box_{(\eta)} f^{(i)} = 0 \quad \Leftrightarrow \quad \Box_{(g)} f^{(i)} = 0 \tag{1.26}$$

for matter fields and

$$\partial_+ \, \partial_- \, \Phi + \kappa^2 \Theta = G \, \langle \hat{T}_{+-} \rangle \quad \equiv \quad \bar{N} G \hbar \, \partial_+ \, \partial_- \, \ln \Phi \Theta^{-1} \tag{1.27}$$

$$\Phi \partial_+ \, \partial_- \ln \Theta = -G \, \langle \hat{T}_{+-} \rangle \quad \equiv \quad -\bar{N} G \hbar \, \partial_+ \, \partial_- \, \ln \Phi \Theta^{-1} \tag{}$$

$$\tag{1.28}$$

for the geometrical fields where, $\bar{N} = N/24$. The constraint equations tie the geometrical fields Θ, Φ to the matter fields $f^{(i)}$. They are preserved in time. Therefore we can impose them just at $\mathcal{I}^-$ where they take the form:

$$-\partial_-^2 \, \Phi + \partial_- \, \Phi \partial_- \, \ln \Theta \, = \, G \, \langle \hat{T}_{--} \rangle \, \hat{=} \, 0 \tag{1.29}$$

and

$$-\partial_+^2 \, \Phi + \partial_+ \, \Phi \partial_+ \, \ln \Theta \, = \, G \, \langle \hat{T}_{++} \rangle \, \hat{=} \, 12 \bar{N} G \, (\partial_+ f_+^o)^2 \tag{1.30}$$

where $\hat{=}$ stands for 'equality at $\mathcal{I}^-$.'

We should mention that for any given finite N, there is nonetheless a region in which the quantum fluctuations of geometry are simply too large for the mean field approximation to hold. This is reflected in the fact that a singularity persists in this approximation, although it is now weakened. Evolution equations cannot be solved in closed form any more, hence devising numerical approaches to the solution was a major part of our analysis. To demonstrate the weakening of the singularity, let us recast the evolution equations to give

$$(\Phi - 2\bar{N} G \hbar)\partial_+ \, \partial_- \, \Phi = -\kappa^2 (\Phi - \bar{N} G \hbar)\Theta - \bar{N} G \hbar \, \Phi^{-1} \partial_+ \Phi \partial_- \Phi$$

$$\partial_+ \, \partial_- \, \ln \Theta = -\frac{\bar{N} G \hbar}{\Phi - \bar{N} G \hbar} \partial_+ \, \partial_- \, \ln \Phi \, . \tag{1.31}$$

The mixed derivative of the fields diverges when Φ now assumes a *non-zero* value $NG\hbar/12$,

18

unless the right hand side vanishes. The right hand side of the first equation does not vanish at the critical value of Φ, and the divergence indeed occurs which has been also seen in all previous numerical studies [12]. However, at the singularity, the conformal factor does not diverge, being $\Theta\Phi^{-1}$, whence g^{ab} is invertible. Furthermore, g^{ab} is also C^0 across this singularity but not C^1. Finally, because of back-reaction, the strength of the singularity diminishes as the black hole evaporates and the singularity ends in the interior of space-time; in contrast to the classical singularity, it does not reach $\mathcal{I}_R^+$ (see Fig. 1.3). It is the dynamics of g_{ab} that exhibit novel features.

We will conclude this discussion of the field equations with a few remarks, and a description of our initial conditions. Because $\hat{f}_-^{(i)}$ are all in the vacuum state, it follows immediately that, as in the classical theory, all the right moving fields vanish; $f_-^{(i)} = 0$ also in the mean-field theory. Similarly, because $\hat{f}_+^{(i)}$ are in a coherent state peaked at some classical profile f_+^o, it follows that, for all i, $f_+^{(i)}(z^+) = f_+^o(z^+)$ (on the entire fiducial Minkowski manifold M^o). Thus, as far as matter fields are concerned, there is no difference between the classical and mean-field theory. Similarly, as in the classical theory, we can integrate the constraint equations to obtain initial data on two null hypersurfaces. We will assume that $f_+^{(o)}$ vanishes to the past of the line $z^+ = z_o^+$. Let I_L^- denote the line $z^+ = z_o^+$ and I_R^- the portion of the line $z^- = z_o^- \ll -1/\kappa$ to the future of $z^+ = z_o^+$. We will specify initial data on these two surfaces. The solution to the constraint equations along these lines is not unique and, as in the classical theory we require additional physical input to select one. We will again require that Φ be in the dilaton vacuum to the past of I_L^- and by continuity on I_L^-. Following the CGHS literature, we will take it to be $\Phi = e^{\kappa(z^+ - z^-)}$. [4] *Thus, the initial values of semi-classical Θ, Φ coincide with those of classical $\underline{\Theta}, \underline{\Phi}$:*

$$\Theta \,\hat{=}\, e^{\kappa(z_o^+ - z^-)} \quad \text{on all of } I_L^- \text{ and } I_R^- \tag{1.32}$$

[4] Strictly, since $\hat{\Phi}$ is an operator on the tensor product of N Fock spaces, one for each $\hat{f}^{(i)}$, the expectation value is $Ne^{\kappa(z^+ - z^-)}$. But this difference can be compensated by shifting z^-. We have chosen to use the convention in the literature so as to make translation between our expressions and those in other papers easier.

and

$$\Phi \; \hat{=} \; \Theta \quad \text{on } I_L^- \text{ and,}$$

$$\Phi \; \hat{=} \; \Theta - 12\bar{N}G\int_{-\infty}^{z^+}\mathrm{d}\bar{z}^+ \, e^{\kappa\bar{z}^+} \int_{-\infty}^{\bar{z}^+}\mathrm{d}\bar{\bar{z}}^+ \, e^{-\kappa\bar{\bar{z}}^+} \, (\tfrac{\partial f_+^{(o)}}{\partial \bar{\bar{z}}^+})^2$$

$$\text{on } I_R^- \tag{1.33}$$

(see Eq. 1.17). The difference in the classical and semi-classical theories lies entirely in the evolution equations (1.27) and (1.28). In the classical theory, the right hand sides of these equations vanish whence one can easily integrate them. In the mean-field theory, this is not possible and one has to take recourse to numerical methods. Finally, while our analytical considerations hold for any regular profile f_+^o, to begin with we will follow the CGHS literature in Sec. 3.2 and Sec. 3.3 and specify f_+^o to represent a collapsing shell as we did for the classical equations:

$$12\bar{N} \left(\frac{\partial f_+^o}{\partial z^+}\right)^2 = M_{\mathrm{ADM}}\, \delta(z^+) \tag{1.34}$$

so the shell is concentrated at $z^+ = 0$. In the literature this profile is often expressed, using x^+ in place of z^+, as:

$$12\bar{N} \left(\frac{\partial \tilde{f}_+^o}{\partial x^+}\right)^2 = M_{\mathrm{ADM}}\, \delta(x^+ - \frac{1}{\kappa}) \tag{1.35}$$

where $\tilde{f}^{(o)}(x^+) = f^{(o)}(z^+)$. In Sec. 3.4 we will also discuss results from a class of smooth matter profiles.

1.3.4 Singularity, horizons and the Bondi mass

The classical solution Eq. 1.17 has a singularity ℓ_s where Φ vanishes. As remarked in section 1.3.3 , in the mean-field theory, a singularity persists but it is shifted to $\Phi = 2\bar{N}G\hbar$ [12]. The metric $g^{ab} = \Theta^{-1}\Phi\,\eta^{ab}$ is invertible and continuous there but not C^1. Thus the singularity is weakened relative to the classical theory. Furthermore, its spatial extension is

diminished. As indicated in Fig.1.3, the singularity now originates at a finite point on the collapsing shell (i.e. does not extend to $\mathcal{I}_{\mathrm{L}}^{+}$) and it ends in the space-time interior (i.e., does not extend to $\mathcal{I}_{\mathrm{R}}^{+}$).

What is the situation with horizons? Recall from Sec. 1.2 that, in the spherically symmetric reduction from 4 dimensions, $r^2 = e^{-2\phi}/\kappa^2 := \Phi/\kappa^2$ and each round 2-sphere in 4-dimensional space-time projects down to a single point on the 2-manifold M. Thus, in the CGHS model we can think of Φ as defining the 'area' associated with any point. (It is dimensionless because in D space-time dimensions the area of spatial spheres has dimension $[L]^{D-2}$.) Therefore it is natural to define a notion of trapped points: A point in the CGHS space-time (M, g) is said to be *future trapped* if $\partial_+\Phi$ and $\partial_-\Phi$ are both negative there and *future marginally trapped* if $\partial_+\Phi$ vanishes and $\partial_-\Phi$ is negative there [12, 18]. In the classical solution resulting from the collapse of a shell Eq. 1.34, all the marginally trapped points lie on the event horizon and their area is a constant; we only encounter an isolated horizon [19] (see Fig.1.2). The mean-field theory is much richer because it incorporates the back reaction of quantum radiation. In the case of a shell collapse, the field equations now imply that a marginally trapped point first forms at a point on the shell and has area [2]

$$
\begin{aligned}
\mathbf{a}_{\mathrm{initial}} &:= \left. (\Phi - 2\bar{N}G\hbar) \right|_{\mathrm{initial}} \\
&= -\bar{N}G\hbar + \bar{N}G\hbar \left(1 + \frac{M_{\mathrm{ADM}}^2}{\bar{N}^2\hbar^2\kappa^2} \right)^{\frac{1}{2}}
\end{aligned}
\tag{1.36}
$$

As time evolves, this area *shrinks* because of quantum radiation [12]. The world-line of these marginally trapped points forms a *generalized dynamical horizon* (GDH), 'generalized' because the world-line is time-like rather than space-like [19]. (In 4 dimensions these are called marginally trapped tubes [20].) The area finally shrinks to zero. This is the point at which the GDH meets the end-point of the (weak) singularity [10, 12, 21] (see Fig.1.3). It is remarkable that all these interesting dynamics occur simply because, unlike in the

classical theory, the right sides of the dynamical Eqs. 1.27, 1.28 are non-zero, given by the trace-anomaly.

We will see in section 3.2 that while the solution is indeed asymptotically flat at $\mathcal{I}_R^+$, in contrast to the classical solution, $\mathcal{I}_R^+$ *is no longer complete.* More precisely, the space-time (M, g) now has a future boundary at the last ray —the null line to $\mathcal{I}_R^+$ from the point at which the singularity ends— and the affine parameter along $\mathcal{I}_R^+$ *with respect to g_{ab} has a finite value* at the point where the last ray meets $\mathcal{I}_R^+$. Therefore, in the semi-classical theory, *we cannot even ask if this space-time admits an event horizon.* While the notion of an event horizon is global and teleological, the notion of trapped surfaces and GDHs is quasi-local. As we have just argued, these continue to be meaningful in the semi-classical theory. What forms and evaporates is the GDH.

Next, let us discuss the structure at null infinity [13, 17]. As in the classical theory, we assume that the semi-classical space-time is asymptotically flat at $\mathcal{I}_R^+$ in the sense that, as one takes the limit $z^+ \to \infty$ along the lines $z^- = \mathrm{const}$, the fields Φ, Θ have the following behavior:

$$
\begin{aligned}
\Phi &= A(z^-)\, e^{\kappa z^+} + B(z^-) + O(e^{-\kappa z^+}) \\
\Theta &= \underline{A}(z^-)\, e^{\kappa z^+} + \underline{B}(z^-) + O(e^{-\kappa z^+}),
\end{aligned}
\tag{1.37}
$$

where $A, B, \underline{A}, \underline{B}$ are some smooth functions of z^-. Note that the leading order behavior in Eq. 1.37 is the same as that in the classical solution. The only difference is that $B, \underline{B}$ are not required to be constant along $\mathcal{I}_R^+$ because, in contrast to its classical counterpart, the semi-classical space-time is non-stationary near null infinity due to quantum radiation. Therefore, as in the classical theory, $\mathcal{I}_R^+$ can be obtained by taking the limit $z^+ \to \infty$ along the lines $z^- = \mathrm{const}$. The asymptotic conditions (1.37) on Θ, Φ imply that curvature —i.e., the Ricci scalar of g_{ab}— goes to zero at $\mathcal{I}_R^+$. We will see in section 3.2 that these conditions are indeed satisfied in semi-classical space-times that result from collapse of matter from

$\mathcal{I}_{\mathrm{R}}^{-}$.

Given this asymptotic fall-off, the field equations determine $\underline{A}$ and $\underline{B}$ in terms of A and B. The metric g_{ab} admits an *asymptotic* time translation t^{a} which is unique up to a constant rescaling and the rescaling freedom can be eliminated by requiring that it be (asymptotically) unit. The function $A(z^{-})$ determines the affine parameter y^{-} of t^{a} via:

$$e^{-\kappa y^{-}} = A(z^{-}).\tag{1.38}$$

Thus y^{-} can be regarded as the unique asymptotic time parameter with respect to g_{ab} (up to an additive constant). Near $\mathcal{I}_{\mathrm{R}}^{+}$ the mean-field metric g can be expanded as:

$$\mathrm{d}S^{2} = -\left(1 + Be^{\kappa(y^{-}-y^{+})} + O(e^{-2\kappa y^{+}})\right)\mathrm{d}y^{+}\,\mathrm{d}y^{-}\tag{1.39}$$

where $y^{+} = z^{+}$.

Finally, equations of the mean-field theory imply [13, 17] that there is a balance law at $\mathcal{I}_{\mathrm{R}}^{+}$:

$$\frac{\mathrm{d}}{\mathrm{d}y^{-}}\Big[\frac{\mathrm{d}B}{\mathrm{d}y^{-}} \;+\; \kappa B \,+\, \bar{N}\hbar G\,\Big(\frac{\mathrm{d}^{2}y^{-}}{\mathrm{d}z^{-2}}\,\Big(\frac{\mathrm{d}y^{-}}{\mathrm{d}z^{-}}\Big)^{-2}\Big)\Big]$$
$$= \;-\frac{\bar{N}\hbar G}{2}\,\Big[\frac{\mathrm{d}^{2}y^{-}}{\mathrm{d}z^{-2}}\,\Big(\frac{\mathrm{d}y^{-}}{\mathrm{d}z^{-}}\Big)^{-2}\,\Big]^{2}.\tag{1.40}$$

In [13], this balance law was used to introduce a new notion of Bondi mass and flux. The left side of (1.40) led to the definition of the Bondi mass:

$$M_{\mathrm{Bondi}}^{\mathrm{ATV}} = \frac{\mathrm{d}B}{\mathrm{d}y^{-}} + \kappa B \,+\, \bar{N}\hbar G\,\Big(\frac{\mathrm{d}^{2}y^{-}}{\mathrm{d}z^{-2}}\,\Big(\frac{\mathrm{d}y^{-}}{\mathrm{d}z^{-}}\Big)^{-2}\Big),\tag{1.41}$$

while the right side provided the Bondi flux:

$$F^{\mathrm{ATV}} = \frac{\bar{N}\hbar G}{2}\,\Big[\frac{\mathrm{d}^{2}y^{-}}{\mathrm{d}z^{-2}}\,\Big(\frac{\mathrm{d}y^{-}}{\mathrm{d}z^{-}}\Big)^{-2}\,\Big]^{2},\tag{1.42}$$

so that we have:

$$\frac{dM_{\text{Bondi}}^{\text{ATV}}}{dy^-} = -F^{\text{ATV}}.$$

(1.43)

By construction, as in 4 dimensions, the flux is manifestly positive so that $M_{\text{Bondi}}^{\text{ATV}}$ decreases in time. Furthermore, it vanishes on an open region if and only if $y^- = C_1 z^- + C_2$ for some constants C_1, C_2, i.e. if and only if the asymptotic time translations defined by the physical, mean field metric g and by the fiducial metric η agree at $\mathcal{I}_R^+$, or, equivalently, *if and only if the asymptotic time translations of g on $\mathcal{I}_L^-$ and $\mathcal{I}_R^+$ agree*. Finally, note that $g^{ab} = \eta^{ab}$, $f_\pm = 0$, $\Phi = \Theta = \exp \kappa(z^+ - z^-)$, is a solution to the full mean-field equations. As one would expect, both $M_{\text{Bondi}}^{\text{ATV}}$ and F^{ATV} vanish for this solution.

The balance law is just a statement of conservation of energy. As one would expect, $\hbar$ appears as an overall multiplicative constant in Eq. 1.42; in the classical theory, there is no flux of energy at $\mathcal{I}_R^+$. If we set $\hbar = 0$, $M_{\text{Bondi}}^{\text{ATV}}$ reduces to the standard Bondi mass formula in the classical theory (see e.g., [18]). Previous literature [8, 12, 18, 21, 22, 23, 24] on the CGHS model used this classical expression also in the semi-classical theory. Thus, in the notation we have introduced here, the traditional definitions of mass and flux are given by

$$M_{\text{Bondi}}^{\text{Trad}} = \frac{dB}{dy^-} + \kappa B,$$

(1.44)

and

$$F^{\text{Trad}} = F^{\text{ATV}} + \bar{N}\hbar G \frac{d}{dy^-} \Big(\frac{d^2 y^-}{dz^{-2}} \Big(\frac{dy^-}{dz^-} \Big)^{-2} \Big).$$

(1.45)

We will see in Sec. 3.3 that numerical simulations have shown that $M_{\text{Bondi}}^{\text{Trad}}$ can become negative and large even when the horizon area is large, while $M_{\text{Bondi}}^{\text{ATV}}$ remains positive throughout the evaporation process.

1.3.5 Scaling and the Planck regime

Finally, we note a scaling property of the mean-field theory, which Ori recently and independently also uncovered [25] and which is also observed in other quantum gravitational systems [26]. We were led to it while attempting to interpret numerical results which at first seemed very puzzling; it is thus a concrete example of how useful the interplay between numerical and analytical studies can be. Let us fix $z^{\pm}$ and regard all fields as functions of $z^{\pm}$. Consider any solution $(\Theta, \Phi, N, f_+^{(i)})$ to our field equations, satisfying boundary conditions (1.32) and (1.33). Then, given a positive number λ, $(\tilde{\Theta}, \tilde{\Phi}, \tilde{N}, \tilde{f}_+^{(i)})$ given by[5]

$$\tilde{\Theta}(z^+, z^-) = \lambda\Theta(z^+, z^- + \frac{\ln\lambda}{\kappa}), \quad \tilde{N} = \lambda N$$

$$\tilde{\Phi}(z^+, z^-) = \lambda\Phi(z^+, z^- + \frac{\ln\lambda}{\kappa}), \quad \tilde{f}_+^{(i)}(z^+) = f_+^{(i)}(z^+)$$

is also a solution satisfying our boundary conditions, where, as before, we have assumed that all scalar fields have an identical profile f_+^o. Note that f_+^o is completely general; we have not restricted ourselves, e.g., to shells. Under this transformation, we have

$$\bar{g}^{ab} \rightarrow \bar{g}^{ab}$$

$$y^- \rightarrow y^- - \frac{1}{\kappa}\ln\lambda$$

$$M_{\text{ADM}} \rightarrow \lambda M_{\text{ADM}}$$

$$M_{\text{Bondi}}^{\text{ATV}} \rightarrow \lambda M_{\text{Bondi}}^{\text{ATV}}$$

$$F^{\text{ATV}} \rightarrow \lambda F^{\text{ATV}}$$

$$\mathbf{a}_{\text{GDH}} \rightarrow \lambda\,\mathbf{a}_{\text{GDH}} \tag{1.46}$$

where $\mathbf{a}_{\text{GDH}}$ denotes the area of the generalized dynamical horizon. This symmetry implies that, *as far as space-time geometry and energetics are concerned, only the ratios M/N*

---

[5]The shift in z^- is needed because we chose to use the initial value $\Theta = e^{\kappa}(z^+ - z^-)$ on I_{L}^- as in the literature rather than $\Theta = Ne^{\kappa(z^+-z^-)}$. See footnote 4.

matter, not separate values of M and N themselves (where M can either be the ADM or the Bondi mass). Thus, for example, whether for the evaporation process a black hole is 'macroscopic' or 'Planck size' depends on the ratios M/N and $\mathbf{a}_{\mathrm{GDH}}/N$ rather than on the values of M or $\mathbf{a}_{\mathrm{GDH}}$ themselves.

We will set

$$
\begin{aligned}
M^\star &= M_{\mathrm{ADM}}/\bar{N} \\
M^\star_{\mathrm{Bondi}} &= M^{\mathrm{ATV}}_{\mathrm{Bondi}}/\bar{N}, \text{ and} \\
m^\star &= M^\star_{\mathrm{Bondi}}|_{\text{last ray}}
\end{aligned}
\tag{1.47}
$$

(We use $\bar{N} = N/24$ in these definitions because the dynamical equations feature $\bar{N}$ rather than N.) We will need to compare these quantities with the Planck mass. Now, in 2 dimensions, G, $\hbar$ and c do not suffice to determine Planck mass, Planck length and Planck time uniquely because $G\hbar$ is dimensionless. But in 4 dimensions we have unambiguous definitions of these quantities and, conceptually, we can regard the 2-dimensional theory as obtained by its spherical reduction. In 4 dimensions, (using the c=1 units used here) the Planck mass is given by $M^2_{\mathrm{Pl}} = \hbar/G_4$ and the Planck time by $\tau^2_{\mathrm{Pl}} = G_4\,\hbar$. From Eqs. 1.10 and 1.11, it follows that G_4 is related to the 2-dimensional Newton's constant G via $G = G_4\kappa^2$. Therefore we are led to set

$$
M^2_{\mathrm{Pl}} = \frac{\hbar\kappa^2}{G}, \quad \text{and} \quad \tau^2_{\mathrm{Pl}} = \frac{G\hbar}{\kappa^2}\,.
\tag{1.48}
$$

When can we say that a black hole is macroscopic? One's first instinct would be to say that the ADM mass should be much larger than M_{Pl} in (1.48). But this is not adequate for the evaporation process because the process depends also on the number of fields N. In the external field approximation where one ignores the back reaction, we know that at late times the black hole radiates as a black body at a fixed temperature $T_{\mathrm{Haw}} = \kappa\hbar$. [6]

___
[6]Note that this relation is the same as that in 4 dimensions because the classical CGHS black hole is

The Hawking energy flux at $\mathcal{I}_R^+$ is given by $F^{\mathrm{Haw}} = \bar{N}\kappa^2\hbar/2$. Therefore the evaporation process will last much longer than 1 Planck time if and only if $(M_{\mathrm{ADM}}/F^{\mathrm{Haw}}) \gg \tau_{\mathrm{pl}}$, or, equivalently

$$M^\star \gg G\hbar\, M_{\mathrm{Pl}}. \tag{1.49}$$

(Recall that $G\hbar$ is the Planck number.) So, a necessary condition for a black hole to be macroscopic is that $M^\star$ should satisfy this inequality. In section 3.3 we will see that, in the mean-field theory, quantum evaporation reveals universality already if $M^\star \gtrsim 4\, G\hbar\, M_{\mathrm{Pl}}$.

1.4 Another Look at the Information Loss Problem

Here, we give an alternative view of black hole evaporation, that is well suited for 2 dimensions. It originates from the work of Ashtekar, Taveras and Varadarajan (ATV from here on).

Consider the spacetime in Fig. 1.2. In summary, we send some energy from $\mathcal{I}_R^-$ which collapses and forms a singularity. We do not send any energy from $\mathcal{I}_L^-$, that is, quantum mechanically, we send in the vacuum state. We are working with a curved spacetime, so to be more specific, we send in a state which is annihilated with respect to the annihilation operators associated with the affine coordinates on $\mathcal{I}_L^-$, namely $z^\pm$ (we called it $|0_z\rangle$ in Sec. 1.3.1). However, once observers interpret this quantum state on $\mathcal{I}_R^+$, they use the coordinates $y^\pm$. In these coordinates, there are different annihilation operators, which do not annihilate $|0_z\rangle$. This means, what was prepared as vacuum is now interpreted as a state with particles which manifests itself as the Hawking radiation, Eq. 1.24. Even more importantly for our case, note that the affine coordinate y^- becomes infinite at the last ray, meaning that the physical spacetime ends on the last ray. The upper corner of the Penrose diagram in Fig. 1.2 whose boundary are the dotted lines is not part of the physical spacetime

stationary to the future of the collapsing matter with surface gravity κ. However, there is also a *key* difference: now κ is just a constant, independent of the mass of the black hole. Therefore, unlike in 4 dimensions, the temperature of the CGHS black hole is a universal constant in the external field approximation. Therefore, when back reaction is included, one does not expect a CGHS black hole to get hotter as it shrinks.

manifold, even though it is a part of the fiducial manifold M^o. However, part of the state $|0_z\rangle$ is related to the degrees of freedom living on this missing piece, hence, one needs to take a partial trace over them to interpret $|0_z\rangle$ on $\mathcal{I}_R^+$. Partial tracing turns the pure state into a mixed state, hence information is lost, which can be seen from the thermal nature of the Hawking radiation [12].

A possible scenario in a theory of exact quantum gravity would be the resolution of the singularity. Even though there would possibly be strong quantum effects in the vicinity of the classical singularity, the physical spacetime would continue beyond it. The physical manifold would coincide with M^o, that is, there is no "missing piece", unlike the classical case. The affine coordinates still would not agree, hence there would be Hawking radiation, but since there is no partial tracing, the evolution would be unitary and there will be no information loss.

Unfortunately, we do not have an exact quantum gravity theory for the CGHS model. Our aim regarding the information loss problem is finding a middle ground with the MFA equations as conjectured in [13]. We have already seen that there is still a singularity at the semiclassical level, but it is weakened (see Fig. 1.3). On the singularity, the metric is invertible and the fields are continuous, which means there is a possibility that the physical spacetime manifold continues beyond the singularity and the last ray, that is $\mathcal{I}_R^+$ coincides with $\mathcal{I}_R^{o+}$ (remember that the former is a proper subset of the latter in the classical case). This means there is again no need for partial tracing, hence information is conserved, even after the leading quantum contributions.

The quantitative manifestation of this scenario is having a finite value of y^- at the last ray, which means the portion of the null infinity before the last ray is not complete. Hence, an important piece of information we will try to discover in the following discussion will be the finiteness of y^- at the last ray. This is a necessary but not sufficient condition, since we also need $y^-(z^-)$ to be a well behaved function for the Bogolubov transformations to also be well behaved. Nevertheless, establishing the finiteness of y^- is an important indication

that the recipe of ATV resolves the information loss problem.

Chapter 2

Numerical Methods

We have seen that, although the full quantum equations for the CGHS model are too complicated to solve, in the mean field approximation (MFA) the model reduces to a coupled set of non-linear partial differential equations, possessing a well-posed characteristic initial value formulation. Unfortunately, even for these equations, analytical solutions are not known except in special limiting cases. Therefore, to explore black hole formation and evaporation, numerical methods are essential.

Numerical studies of the CGHS model already had a quite rich literature before our work [9, 10, 11]. These studies had elucidated the basic spacetime picture presented in Fig. 1.3. However, they missed the crucial fact that the CGHS model has two distinct regimes in the parameter space, $M \gg (N/24)M_{\mathrm{Pl}}$ and $M \ll N/24M_{\mathrm{Pl}}$ (see Sec. 1.3.5), where M is the initial mass of the black hole that forms and N is the number of f fields. These two regimes have radically different physical properties and interpretations, their numerical analysis also presents considerably different levels of challenge. The basic point is that, in the macroscopic mass case, all of the interesting physics is confined to a tiny region in the vicinity of the last ray, where a high numerical accuracy is needed. Existing numerical studies of the CGHS model focused on the intermediate mass range $M \sim N/24$, for example $\frac{M}{24N} = 1$ in [10] and $\frac{M}{24N} = 2.5$ in [11] (M_{Pl} set to 1). This

case is considerably easier to solve numerically, but the price is that many of the interesting phenomena of the black hole evaporation cannot be observed. Even though our main aim is solving the macroscopic mass black hole spacetimes, we also solve spacetimes with sub-Planck masses for completeness, and also to present the contrast between the two cases.

Since macroscopic CGHS black holes were not numerically studied before, and due to the challenges we summarized above, we had to use a combination of numerical techniques to achieve roundoff level accuracy in our code. An outline of the rest of the chapter is as follows. In Sec. 2.1 we describe the variable definitions and conventions we use, the analytical equations that we discretize, and the initial data we use for the numerical solution. In Sec. 2.2, we describe some of the issues that would cause naive discretization of the equations to fail to uncover the full spacetime, and how to overcome them; this includes regularization of otherwise asymptotically-divergent field variables, compactification of the coordinates, the particular discretization scheme, and use of Richardson extrapolation ideas to increase the accuracy of the solution. In Sec. 2.2 we also discuss setting initial conditions near $\mathcal{I}$, and how we extract the desired asymptotic properties of the solution. In Sec. 2.3 we describe various tests to demonstrate we have a stable, convergent numerical scheme to solve the CGHS equations.

2.1 CGHS Model in the MFA as an Initial Value Problem

Recall that at the semiclassical level, the analysis of the CGHS model is reduced to solving the evolution equations

$$\partial_+ \partial_- \Phi + \kappa^2 \Theta = \bar{N} G \hbar \partial_+ \partial_- \ln \Phi \Theta^{-1}$$

$$\Phi \partial_+ \partial_- \ln \Theta = -\bar{N} G \hbar \partial_+ \partial_- \ln \Phi \Theta^{-1}$$

for the geometric fields together with the *constraint equations*

$$
\begin{aligned}
-\partial_-^2\,\Phi + \partial_-\,\Phi\partial_-\,\ln\Theta &= G\,\langle \hat{T}_{--}\rangle \,\hat{=}\, 0 \\
-\partial_+^2\,\Phi + \partial_+\,\Phi\partial_+\,\ln\Theta &= G\,\langle \hat{T}_{++}\rangle \,\hat{=}\, 12\bar{N}G\,(\partial_+ f_+^o)^2
\end{aligned}
\tag{2.1}
$$

In a characteristic initial value problem, we specify initial data on a pair of intersecting, null hypersurfaces $z^+(z^-) = z_0^+$ and $z^-(z^+) = z_0^-$, to the causal future of their intersection point (z_0^+, z_0^-) as we mentioned in Sec. 1.3.3 (see [27] for a review). Thus one can see where the constraint equations Eq. 2.1 receive their name: for example, if we specify the scalar field f (hence T_{++}, T_{--}) and metric field Θ on these surfaces as initial data, we are *not* free to choose Φ, which is then given by integrating Eq. 2.1. The constraint equations are *propagated* by the evolution equations Eq. 1.14, namely, if the constraints are satisfied on the initial hypersurfaces, solving for the fields to the causal future using Eq. 1.14 guarantees the constraints are satisfied for all time. *This is exactly true at the analytical level, though in a numerical evolution this property of the field equations will in general only be satisfied to within the truncation error of the discretization scheme.*

To present our numerical methods, we will exclusively consider the case of the left-moving shock wave we introduced in Sec. 1.3.1 and 1.3.3

$$
12\bar{N}\,\left(\frac{\partial f_+^o}{\partial z^+}\right)^2 = M\,\delta(z^+)
\tag{2.2}
$$

and no incoming matter from the left ($f_- = 0$). This choice reduces the problem to evolving the fields Φ and Θ according to (1.14) with the asymptotic initial conditions

$$
\begin{aligned}
\Theta(z^{\pm}) &= e^{\kappa(z^+-z^-)} \\
\Phi(z^{\pm}) &= e^{\kappa(z^+-z^-)} - \frac{GM}{\kappa}(e^{\kappa z^+} - 1)\,,
\end{aligned}
\tag{2.3}
$$

for $z^+ > 0$, $z^- \to -\infty$, which we had derived. Both fields are trivially given by $e^{\kappa(z^+-z^-)}$

for $z^+ < 0$. *With these restrictions, any space-time is defined by the two quantities M and N.*

In the next chapter, we will also be discussing initial data with extended profiles (rather than a $\delta-$function). In terms of numerical methods, this does not bring any other difficulties, and we will not be elaborating on these calculations here.

Remember that when the evaporation has proceeded to the point where the dynamical horizon meets the singularity (see Fig. 1.3), it becomes naked, i.e. visible to observers at $\mathcal{I}_R^+$. The MFA equations cannot be solved beyond this Cauchy horizon, which we call the *last ray*. It should be possible to mathematically extend the spacetime beyond the last ray, in particular as the geometry does not appear to be singular here (except at the point the dynamical horizon meets the last ray) as we showed in Sec. 1.3.3. However, since the fields are not differentiable on the singularity, one needs a prescription about the relationship between the derivative of the fields on the two sides of the singularity to have such an extension. There is not a universally agreed upon prescription, hence currently there is no unambiguous way to evolve the fields beyond the singularity and the last ray. Even though we give this short discussion of what might happen beyond the last ray, *we do not explore this issue*, and will only calculate the fields in the region before the last ray.

In all our simulations we use $G = \hbar = \kappa = 1$. We showed the scaling symmetry of the CGHS model in Sec. 1.3.5, hence we will only use a single value of $N = 24$ ($\bar{N} = 1$), which covers all the physical parameter space as M changes. Hence, by macroscopic mass, we mean $M \gg 1$, and by sub-Planck-scale mass, we mean $M \ll 1$.

2.2 The Numerical Calculation

2.2.1 Compactification of the Coordinates

Rather than discretizing the equations with respect to the z^+, z^- coordinates, we introduce a compactified coordinate system $z_c^+ \in [0, \frac{1}{2}]$ and $z_c^- \in [0, 1]$. Use of compact coordinates is
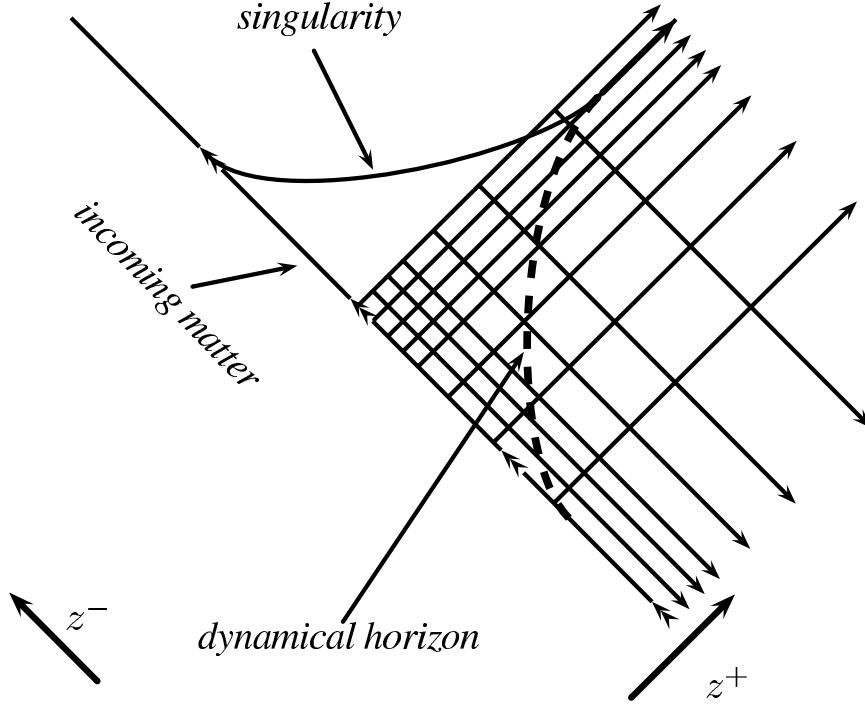
Figure 2.1: A schematic view of the positions of the grid lines on the uncompactified space. Lines are concentrated near the last ray, where we need higher resolution. They become distant as one approaches the null infinities.

important for a couple of reasons, and essential for the $M \gg 1$ case. First, to understand the asymptotic structure of the spacetime approaching $\mathcal{I}_R^+$, it is useful to have the computational domain include $\mathcal{I}_R^+$. We have seen that most of the physics of the CGHS black holes can be extracted from the field values near this region (see Sec. 1.3.4). Second, the uncompactified coordinate z^- is adapted to the flat metric near $\mathcal{I}_L^-$; however, it turns out that most of the interesting features of black hole evaporation near the dynamical horizon occur in an exponentially small region $\Delta z^- \sim \kappa^{-1} e^{-GM/\kappa}$ before the last ray. One can think of this as essentially due to gravitational redshift. Classically (without evaporation), the redshift causes arbitrarily small lengths scales near the horizon to be expanded to large scales near $\mathcal{I}_R^+$. This can be easily seen from Eq. 1.21 where $\frac{dy^-}{dz^-} \to \infty$ as $y^- \to \infty$.

Naively one might have expected that evaporation changes this pictures completely (as suggested by the Penrose diagram in Fig. 1.3). Instead, what we find is that although there

is not an arbitrarily large redshift once back-reaction is included, there is still an exponential growth of scales, with the growth rate proportional to the mass of the black hole as indicated above.

Thus, a uniform discretization in z^- that is able to resolve both the early dynamics near $\mathcal{I}_R^-$, yet can adequately uncover the exponentially small scales (as measured in z^-) of the late-time evaporation, will (for large M) result in a mesh too large to be able to solve the equations using contemporary computer systems. To overcome this problem, we introduce a non-uniform compactification in z^-, schematically illustrated in Fig. 2.1, that provides sufficient resolution to resolve the spacetime near the last ray, yet does not over-resolve the region near $\mathcal{I}_R^-$. Specifically, the transformation from z^- to z_c^- we use is as follows. First, we relate the uncompactified z^- to an auxiliary (non-compact) coordinate $\bar{z}^-$ by

$$z^- = \bar{z}^- \left(\frac{\bar{z}^- - L_R^{-1/2}}{\bar{z}^- - L_R^{1/2}} \right) + z_{s,est}^- \tag{2.4}$$

where $z^- \in (-\infty, z_{s,est}^-]$ and $\bar{z}^- \in (-\infty, 0]$. $z_{s,est}^-$ is an estimate of the z^- coordinate of the last ray. This is also the earliest time in z^- that we will encounter the spacetime singularity, and at present we do not continue the computation past this point (the compactification functions can readily be adjusted to cover $z^- \in (-\infty, \infty)$). In these coordinates, the region near the last ray ($z^- \approx z_{s,est}^-$, $\bar{z}^- \approx 0$) is resolved by a factor of L_R more than the regions away from the last ray. Next, we convert the auxiliary $\bar{z}^-$ to a compact coordinate z_c^-

$$\bar{z}^- = -e^{-S \tan(\pi z_c^- - \pi/2)} + L_c(z_c^- - 1), \ . \tag{2.5}$$

where S and L_c are constants. This way, the last ray is located near $z_c^- = 1$. The relation between $\bar{z}^-$ and z_c^- is forced to be linear near the last ray through the L_c term, which we will explain next.

Our grid is based on the compact coordinate $\Delta z_c^\pm$, and it is a uniform grid, i.e. it

has a fixed step size $\Delta z_c^- = h$ in the compactified coordinate z_c^-. This corresponds to $\Delta z^- \approx L_c/L_R \, h$ in uncompactified coordinates near $z_c^- = 1$. Hence, we can see that, in order to resolve tiny scales in z^-, we want a high value for L_R and a very small one for L_c. Note that, if there is no linear term with L_c in Eq. 2.5, Δz^- would become arbitrarily small near the last ray (near $z_c^- \approx 1$), which would make taking finite differences impossible due to catastrophic cancellation.

For the highest mass macroscopic black hole discussed here, $M = 16$, we set $L_R = 10^9$, while for the lowest mass of $M = 2^{-10}$, we use $L_R = 10^2$. We use $L_c = 4.096 \times 10^{-9}$, which can be adjusted together with L_R to obtain the desired resolution near the last ray. Note that $\Delta z^- \approx 10^{-18} h$ for the highest mass case; such a disparity in scales would have been difficult to achieve if we had used z^- as our coordinate even *with* a standard adaptive mesh refinement algorithm. We choose S to be between 1 and 5, the particular value of which is not essential.

In the $+$ direction, for $M \gtrsim 1$, we compactify the coordinates using

$$z^+ = M \tan(\pi z_c^+) \qquad M \gtrsim 1 \,, \tag{2.6}$$

with the factor of M ensuring that the singularity is not too close to the $\mathcal{I}_R^+$ edge of the mesh, where the resolution in z^+ is lower due to compactification. For $M \ll 1$, the singularity appears very close to $z^+ = 0$, so to resolve this region, we employ

$$z^+ = C_{z_c^+} \tan^p(\pi z_c^+) \qquad M \ll 1 \,, \tag{2.7}$$

where $C_{z_c^+}$ and p are appropriate constants that again keep the singularity near the middle of the range of z_c^+. For $M = 2^{-10}$, we use $C_{z_c^+} = \frac{1}{7000}$ and $p = 7$.

Even though we presented specific functions to relate the compactified and uncompactified coordinates, none of these are essential. As long as the region near $\mathcal{I}^+$ (any other region where length scales are small) are resolved, and numerical issues are avoided (as in

the use of L_c), any compactification scheme would perform similarly.

2.2.2 Regularization of the Fields

It is clear from Eq. 2.3 that the fields diverge exponentially at $\mathcal{I}_R^-$ and analytical results show that they also diverge at $\mathcal{I}_R^+$ (see Sec. 1.3.4). For a numerical solution then, we define regularized field variables which are finite everywhere

$$
\begin{aligned}
\Phi &= e^{\kappa(z^+-z^-)}\,(1+\bar{\phi}) - M(e^{\kappa z^+} - 1)\\
&= e^{\kappa(z^+-z^-)}\,(1+\bar{\phi}+\bar{\phi}_0)\\
\Theta &= e^{\kappa(z^+-z^-)}\,(1+\bar{\theta})\,,
\end{aligned}
\tag{2.8}
$$

with $\bar{\phi}_0 = -M\,e^{\kappa z^-}(1-e^{-\kappa z^+})$. Aside from removing the divergent component $e^{\kappa(z^+-z^-)}$, this definition also removes the exact classical solution $M(e^{\kappa z^+} - 1)$ from Φ. The reason for doing this came from preliminary studies which showed that deviations in Φ from its classical values were small compared to the classical metric for macroscopic black holes in most of the computational domain. In terms of the new variables, Eq. 1.14 read

$$
\begin{aligned}
&(1+\bar{\theta})^2(1+\bar{\phi}+\bar{\phi}_0)^2\\
&\times \left[\partial_+\partial_-\bar{\phi} - \kappa\partial_+\bar{\phi} + \kappa\partial_-\bar{\phi} - \kappa^2\bar{\phi} + \kappa^2\bar{\theta}\right] - Q(\bar{\phi},\bar{\theta}) = 0
\end{aligned}
\tag{2.9}
$$

and

$$
(1+\bar{\phi}+\bar{\phi}_0)^3\left[(1+\bar{\theta})\partial_+\partial_-\bar{\theta} - \partial_+\bar{\theta}\partial_-\bar{\theta}\right] + Q(\bar{\phi},\bar{\theta}) = 0
\tag{2.10}
$$

with

$$
\begin{aligned}
Q(\bar{\phi}, \bar{\theta}) \;=\; & \frac{NG\hbar}{24} e^{\kappa(z^- - z^+)} \\
\times \Bigg\{ \quad & (1+\bar{\theta})^2 \big[(1+\bar{\phi}+\bar{\phi}_0)\,\partial_+\partial_-(\bar{\phi}+\bar{\phi}_0)\big] \\
- \; & (1+\bar{\theta})^2 \big[\partial_+(\bar{\phi}+\bar{\phi}_0)\,\partial_-(\bar{\phi}+\bar{\phi}_0)\big] \\
- \; & (1+\bar{\phi}+\bar{\phi}_0)^2 \big[(1+\bar{\theta})\partial_+\partial_-\bar{\theta} - \partial_+\bar{\theta}\partial_-\bar{\theta}\big] \Bigg\}
\end{aligned}
\tag{2.11}
$$

There have been numerical studies without regularization (for example [10]) where the initial data was not specified on $\mathcal{I}_R^-$, but rather on a line of $z^- = const \ll -\frac{1}{\kappa}$, where the classical solution that we use on $\mathcal{I}_R^-$ is still valid as initial data to high numerical accuracy, and is finite. We wanted to represent as big a part of the physical spacetime as possible in our computational grid, including $\mathcal{I}_R^-$, hence chose to regularize the fields. This becomes even more important when one tries to analyze the asymptotic quantities near $\mathcal{I}_R^+$, since the fields diverge there as well, which makes the extraction of the asymptotic quantities much harder for the actual Φ and Θ.

2.2.3 Discretization and Algebraic Manipulation

We discretize the compactified coordinate domain as depicted in Fig. 2.2. A field $\alpha(z_c^+, z_c^-)$ is represented by a discrete mesh of values $\alpha_{i,j}$, where the indices i, j are integers, and related to the null coordinates through

$$
\begin{aligned}
z_c^- \;&= ih \qquad 0 \le i \le n_p \\
z_c^+ \;&= jh \qquad 0 \le j \le \tfrac{n_p}{2} \,,
\end{aligned}
\tag{2.12}
$$

where $h = n_p^{-1}$ is the step size in both of the compactified null coordinates. In order to solve the evolution equations numerically, we convert the differential equations to difference

equations by using standard, second order accurate ($\mathcal{O}(h^2)$), centered stencils:

$$\alpha\big|_{i-\frac{1}{2},j-\frac{1}{2}} \approx \frac{\alpha_{i,j} + \alpha_{i-1,j} + \alpha_{i,j-1} + \alpha_{i-1,j-1}}{4}$$

$$\partial'_+\alpha\big|_{i-\frac{1}{2},j-\frac{1}{2}} \approx \frac{\alpha_{i,j} + \alpha_{i-1,j} - \alpha_{i,j-1} - \alpha_{i-1,j-1}}{2h}$$

$$\partial'_-\alpha\big|_{i-\frac{1}{2},j-\frac{1}{2}} \approx \frac{\alpha_{i,j} - \alpha_{i-1,j} + \alpha_{i,j-1} - \alpha_{i-1,j-1}}{2h}$$

$$\partial'_+\partial'_-\alpha\big|_{i-\frac{1}{2},j-\frac{1}{2}} \approx \frac{\alpha_{i,j} - \alpha_{i-1,j} - \alpha_{i,j-1} + \alpha_{i-1,j-1}}{h^2},$$

(2.13)

where we have introduced the notation

$$\partial'_\pm \equiv \frac{\partial}{\partial z_c^\pm} = \frac{\partial z^\pm}{\partial z_c^\pm}\frac{\partial}{\partial z^\pm} = \frac{\partial z^\pm}{\partial z_c^\pm}\partial_\pm \ . \tag{2.14}$$

Once discretized, Eq. 2.9 and Eq. 2.10 give two polynomial equations which can be numerically solved for $\bar{\theta}_{i,j}$ and $\bar{\phi}_{i,j}$, if the field values are known at the grid points $(i, j-1), (i-1, j), (i-1, j-1)$. This way, knowing the boundary conditions at $z^+ = 0$ $(j = 0)$ and $z^- = -\infty$ $(i = 0)$, we can calculate the field values at all points of the grid one by one, starting at $(1, 1)$.

Instead of solving for the two variables simultaneously (e.g. using a two dimensional Newton's method), we sum the equations (2.9, 2.10), which allows us to explicitly express $\bar{\phi}_{i,j}$ in terms of a rational function of $\bar{\theta}_{i,j}$. We then insert this expression for $\bar{\phi}_{i,j}$ into (2.9)[1]. This way, we obtain a single variable, 10th order polynomial equation for $\bar{\theta}_{i,j}$. We solve this equation numerically using Newton's method, and then calculate $\bar{\phi}_{i,j}$ directly using the aforementioned rational function. One advantage of these analytic manipulations before the numerical solution is that, more techniques are available for finding the roots of a polynomial in one variable, compared to a set of generally nonlinear equations. For instance, we also implemented Laguerre's method, which gave similar results to Newton's

---

[1] any other independent linear combination of the equations can also be used
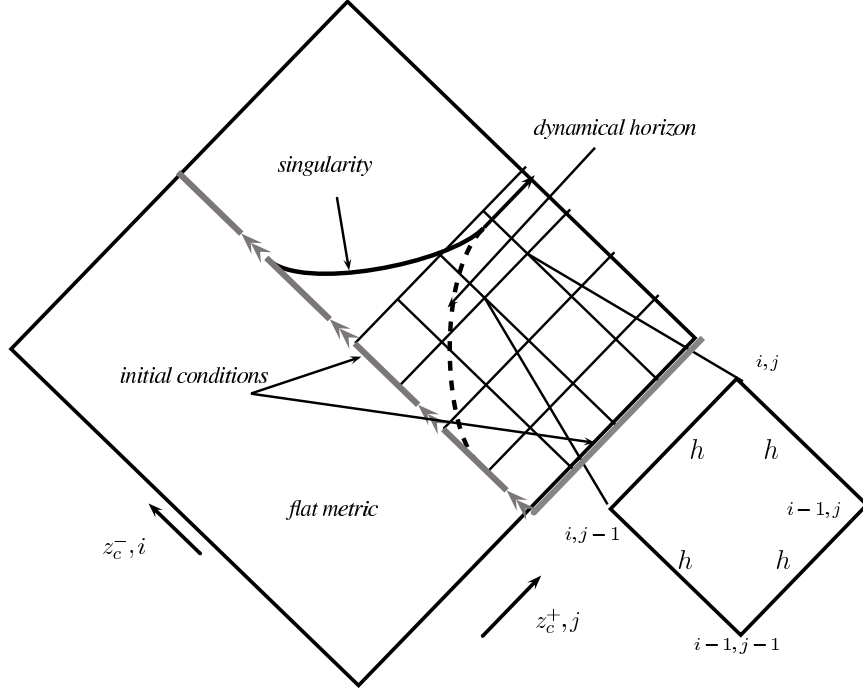
Figure 2.2: The grid structure for the numerical calculation. We use a fixed-step-size mesh based on the compactified coordinates $z_c^{\pm}$, where the step sizes in both directions are equal. The emphasis on the regions where the fields rapidly change is attained using the compactification of the coordinates (see Fig. 2.1). The flat region before the matter pulse and the region beyond the last ray are not covered by the mesh.

method, in terms of robustness and computation time.

2.2.4 Richardson extrapolation with intermittent error removal

For any function α numerically calculated on a null mesh of step size h in both directions, and with central differences as in Eq. 2.13, we have the Richardson expansion

$$\alpha_h = \alpha + c_2 h^2 + c_4 h^4 + c_6 h^6 + \mathcal{O}(h^8) \tag{2.15}$$

where α is the exact solution, α_h is the numerically obtained solution and c_i are *error functions*. α, α_h, and c_i are all functions of $z^{\pm}$ (we omit the explicit dependence for clarity), and α, c_i are independent of h. Note that we cannot *prove* such an expansion exists for

the class of non-linear equations we are solving, in particular if no assumptions on the smoothness of the initial data are made. Furthermore, we know the solutions generically develop singularities, thus the above series can only have a limited radius of convergence for generic initial data. Nevertheless, we will *assume* the expansion exists, and then, via convergence tests, check whether the solutions we obtain are consistent with the expansion.

The use of second order finite difference stencils is responsible for the leading order quadratic convergence of the above expansion. However, using numerical solutions obtained on meshes with different discretization scales, one can obtain higher order convergence by using the well known Richardson extrapolation. For example, a fourth order convergent solution $\alpha_{h,h/2}$ can be obtained from the following superposition of two approximate second order convergent solutions $\alpha_{h/2}$ and α_h : $\alpha_{h,h/2} = (4\alpha_{h/2} - \alpha_h)/3 = \alpha + \mathcal{O}(h^4)$. In theory (for sufficiently smooth solutions), $2n$-th order convergence can be obtained by an appropriate superposition of n second order accurate solutions, each obtained with a different mesh spacing. As we describe in more detail below, we use four successively finer meshes to obtain solutions that converge to $\mathcal{O}(h^8)$ on the points of the coarsest mesh.

Fields in the CGHS model present singular behavior, and since the position where the singularity first appears on the grid is a (convergent) function of the mesh size, the method of superposing solutions of different meshes breaks down at the first time the singularity appears on *any* of the superposed meshes. Typically, the singularity first appears on the coarsest mesh, and thus our domain of integration is fundamentally restricted by our proximity to the singularity on the coarsest mesh. Many of the physical phenomena we are interested in occur in this region, thus a direct use of Richardson extrapolation for solutions over the entire computational domain does not significantly improve our results. To circumvent this problem, as described in more detail in the next few paragraphs, we instead break up the computational domain into a series of short strips in z_c^- (see Fig. 2.3). In each strip we evolve 4 meshes, apply Richardson extrapolation to the solution obtained at the

41

end of the evolution, then use this corrected solution as initial data for all four meshes on the next, adjacent strip. In this way the mismatch in the location of the singularity amongst the four resolutions is confined to be less than the size of the strip, which we can adjust as needed.

Our Richardson extrapolation algorithm proceeds as follows. We divided the entire grid into L equal regions along z_c^- such that grid points i along the corresponding direction with $\frac{l}{L}n_p \leq i \leq \frac{l+1}{L}n_p$, $0 \leq l \leq L$ comprise the lth region. Note that regions coincide at the boundaries, and here indices i and the total number of points n_p are relative to the coarsest mesh—for finer meshes these numbers should be scaled as appropriate so that the lth strip spans the *same coordinate volume* for each resolution. In the lth region

1. We evolve the fields independently on four successively finer meshes of step size $h, h/2, h/4$ and $h/8$, and stop the evolution at the end of the region ($i = \frac{l+1}{L}n_p$).

2. At points coincident with the coarsest resolution, we calculate the appropriate superposition of the four meshes to give $\mathcal{O}(h^8)$ accurate values of the fields ($\bar{\phi}$ and $\bar{\theta}$), and store these values on the coarsest mesh as our result.

3. On the last ($i = \frac{l+1}{L}n_p$) line of the region l, we also calculate the functions $c_k(z^{\pm})$ to accuracy $\mathcal{O}(h^{8-k})$ on the coarsest mesh. We then interpolate the functions c_k to the three finer meshes using successive degree four Lagrange interpolating polynomials. *Using these interpolated c_k values, we correct the field values on the finer meshes using Eq. 2.15, that is we have the highest possible accuracy, not only on the coarsest level, but on all four levels.* A Lagrange polynomial of degree 4 introduces an error of order $\mathcal{O}(h^5)$, so through the c_2 term an error of $\mathcal{O}(h^7)$ will be introduced into the finer mesh solutions. A higher order interpolating polynomial could reduce the error, though we found that a global $\mathcal{O}(h^7)$ scheme is sufficient for our purposes.

4. We use the $\mathcal{O}(h^7)$ accurate field values on the last ($i = \frac{l+1}{L}n_p$) line as the initial data for the next (($l + 1)^{th}$) region, and repeat the procedure for this region starting from

Step 1.

By updating the fields to more accurate values at the end of each region, the accuracy of the position of the singularity in the coarsest mesh is improved significantly, and the problem of the breakdown of the superposition near the singularity is overcome.

We are not aware of any studies on the theoretical stability and accuracy of this modified Richardson extrapolation method, though our convergence and independent residual analysis, described in Sec. 2.3, shows that it works quite well, giving (for the most part) the expected order of convergence.

Implementing this method, we are able to reduce the truncation error down to the level of round-off error using "modest" resources on a single, desktop style CPU. More precisely, we used 80-bit long double precision, which theoretically has a round-off error at the level of $\sim 10^{-19}$ with the compilers we used. However our Newton iteration only converged if we set the accuracy of the iteration to $\sim 10^{-16}$, which was the ultimate source of the error in the calculated regularized field values. When we say "round-off error" then, we will mean this latter value rather than the value of $\sim 10^{-19}$ one might expect from 80-bit precision.

2.2.5   Evolution near $\mathcal{I}$

The boundary conditions on $z^+ = 0$ are those of the vacuum and translate to

$$\bar{\phi}(z^+ = 0, z^-) = \bar{\theta}(z^+ = 0, z^-) = 0 . \tag{2.16}$$

For the $\mathcal{I}_R^-$ boundary, (2.3) translates to

$$\bar{\phi}(z^+, z^- = -\infty) = \bar{\theta}(z^+, z^- = -\infty) = 0 . \tag{2.17}$$

The $e^{\kappa z^-}$ factors in the evolution equations Eq. 2.12 are interpreted as 0 if $e^{\kappa z^-}$ is less than the smallest magnitude floating point number allowed by machine precision, which occurs for $z^- < z^-_{prec}$ for some z^-_{prec}, thus, in the region $z^- < z^-_{prec}$, the evolution equations are trivially solved by the initial conditions $\bar{\theta} = \bar{\phi} = 0$. This means it would make no difference if we imposed the $\mathcal{I}^-_R$ boundary conditions on some other constant $z^- < z^-_{prec}$ line rather than at $z^- = -\infty$. Moreover, even if we impose the $\mathcal{I}^-_R$ boundary conditions on a constant z^- line with $z^- > z^-_{prec}$, the error introduced is exponentially small [10] and negligible compared to the truncation error for a certain range of $|z^-|$. Our numerical method described in Sec. 2.2.3 sometimes fails to produce a solution for the fields in the early stages of the evolution near $\mathcal{I}^+_R$ if we begin the evolution in the region $z^- < z^-_{prec}$. We surmise the failure occurs near the line $z^- = z^-_{prec}$. In such cases of failure, we begin the evolution at $z^- \sim -5 \times 10^3$. This means we could not include $\mathcal{I}^-_R$ on our computational domain, but as we explained, this introduces a completely negligible error.

A related problem is that Newton's method also sometimes cannot converge to a solution for $\bar{\theta}$ near $\mathcal{I}^+_R$, even well before the last ray. In such cases, we evolved the equations as close to $\mathcal{I}^+_R$ as possible. We were able to evolve the fields sufficiently close to $\mathcal{I}^+_R$ to extract all the important asymptotic behavior, as described in the next section.

2.2.6 Asymptotic Behavior

We have seen how to calculate various physical quantities from the values of the fields on $\mathcal{I}^+_R$ in Sec. 1.3.4. Asymptotic coefficients of Eq. 1.40 are related to the regularized fields through

$$
\begin{aligned}
A(z^-) &= e^{-\kappa z^-}\left(1 + \bar{\phi}(z^+ = \infty, z^-)\right) - M \\
B(z^-) &= \lim_{z^+ \to \infty} e^{\kappa z^+}\left(\bar{\phi}(z^+ = \infty, z^-) - \bar{\phi}(z^+, z^-)\right) + M
\end{aligned}
\tag{2.18}
$$

As mentioned in the previous section, we are not able to calculate the fields exactly on

44

$\mathcal{I}_R^+$, and evaluating the above on a line of constant z^+ will introduce an error of the order $e^{-\kappa z^+}$. However, it is adequate to evaluate the above limits at sufficiently large z^+ such that this error is less than the truncation error. It turns out the Newton iteration only breaks down well into the region where the truncation error dominates (see the end of the previous section), which enables us to compute A to high accuracy.

To calculate the limit in B numerically, we need (at least) two values of z^+ for each value of z^-. To minimize the error, naively, it is most desirable to pick as large z^+ values as possible . However, B is expressed as the asymptotically diverging factor $e^{\kappa z^+}$ multiplied by an asymptotically vanishing one, and calculating this via finite precision numerics introduce a large relative round-off error for the vanishing factor, due to catastrophic cancellation. We thus evaluate B using two $z^+ = const$ lines, one of them is the line we calculated A on, the other is chosen such that κz^+ is large enough that the fields are in the asymptotic region but it is also sufficiently away from the other $z^+ = const$ line that catastrophic cancellation is not a major issue. Particular values of z^+ are not important.

Once we have A and B, to obtain M_B and the ATV Bondi flux through Eq. 1.40, we use nine-point finite difference stencils to calculate the first and second derivatives with respect to z_c^- and apply the chain rule to obtain derivatives with respect to z^-. Nine-point stencils have an accuracy of $\mathcal{O}(h^8)$, keeping the theoretical accuracy of our numerical integration scheme.

Note that since B is sub-leading relative to A in the asymptotic expansion Eq. 2.18, A, hence y^-, can be calculated more accurately. Thus, in practice we calculate the Bondi mass M_B by numerically integrating the ATV flux rather than directly evaluating the left hand side of Eq. 1.40.

2.3 Numerical Tests

In this section we present a few sample solutions to the CGHS model in the mean field approximation, and results from an array of tests we performed to ensure we are solving the equations correctly.

2.3.1 Sample evolutions

We calculated numerical solutions for initial black hole masses M ranging from 2^{-10} to 16 (Eq. 2.3). Here, we present the results for $M = 8$ as the macroscopic case for uniformity of exposition. All cases show similar convergence behavior for the regularized fields, though as we approach $M = 16$, derived physical quantities start to show irregular convergence patterns due to catastrophic cancellation. This is expected, since we already mentioned that there is a dilution of scales near the last ray that becomes exponentially stronger with increasing M. The fact that $M = 8$ is sufficiently large to be categorized as "macroscopic" will be established in the next chapter, when we discuss the universality of the solutions. Spacetimes with $M > 16$ cannot be numerically solved near the last ray in our scheme, but we will again see in the next chapter that even $M \sim 6$ is adequate to understand all the physics of CGHS black holes with MFA.

The regularized fields $\bar{\theta}$ and $\bar{\phi}$ from solutions with two values of $M \gg 1$ and $M \ll 1$ are shown in Figs. 2.4 and 2.5. As discussed before, a central issue with the numerical calculations is to ensure that we get close to the last ray and the singularity, as many of the interesting phenomena occur in this region. It is analytically known that the singularity of the CGHS model occurs when $\Phi = \frac{N}{12}$. Moreover, $\Phi - \frac{N}{12}$ evaluated on the dynamical horizon (determined by $\partial_+ \Phi = 0$) can be interpreted as the quantum corrected area of the black hole [10]. This way, we can test our proximity to the singularity by checking the value of the area near the singularity—see Fig.2.6. For $M \gg 1$, the part of our compactification scheme which emphasizes the region near the last ray is crucial. In this case, the area when

the GDH forms for the first time is roughly M. If the region near the last ray is not properly resolved, one sees only *a few percent* of drop in the area, at which point the singularity is encountered on the numerical grid. With our numerical methods, we could see the area of the GDH decrease to a tiny fraction of unity, signaling that we are very close to the last ray in terms of proper distances.

As explicitly seen in Fig.2.6, had we used a uniform mesh in uncompactified $z^{\pm}$ coordinates, a mesh spacing of order $h \lesssim 10^{-M}$ would have been needed. Covering a sufficient region of the spacetime to reveal the asymptotics would require a net coordinate range $\Delta z^{\pm}$ of order unity, implying a mesh of order 10^M points along both directions, which is of course impractical to achieve on contemporary computers for larger M. This important aspect of the problem was not clear in earlier studies, as they usually focused on $M \sim 1$ [10, 11]. We will see in the next chapter that the $M < 1$ solutions are drastically different from the $M > 1$ solutions, in terms of their physical interpretation as well.

2.3.2 Convergence of the Fields

We compute convergence factors by comparing solutions that are obtained using different mesh spacings. Note that we are always using the Richardson extrapolation scheme described in Sec. 2.2, thus in the following when we refer to a solution computed with mesh spacing h, h is the step size of the coarsest one of the four meshes used in the numerical integration.

First, we define

$$\Delta_h f \equiv f_h - f_{h/2} \tag{2.19}$$

where f_h denotes the numerical solution of a function f obtained on a grid with mesh spacing h. $\Delta_h f$ is thus an estimate, to $O(h^n)$, of the truncation error in f, where n is the

rate of convergence of the algorithm. From the Richardson expansion we then get

$$n = \log_2 \left[\frac{\Delta_{2h} f}{\Delta_h f} + O(h) \right] = \log_2 \left[\frac{f_{2h} - f_h}{f_h - f_{h/2}} + O(h) \right], \qquad (2.20)$$

where the next-to-leading order term is of $O(h)$ because of the order of interpolating polynomial we use. From the above, we define an estimated convergence factor n_e via

$$n_e \equiv \log_2 \frac{f_{2h} - f_h}{f_h - f_{h/2}} \qquad (2.21)$$

In Figs. 2.7 and 2.8, we show plots of n_e for high and low mass cases respectively. An "issue" we have with the convergence behavior of the CGHS equations is it seems artificially high for coarser meshes. One reason for this may be that the central difference scheme Eq. 2.13 we use solves the homogeneous part of the wave equation ($\partial_+ \partial_- f = 0$) *exactly* (to within round-off), irrespective of the step size. Furthermore, with our choice of variables and regularization scheme, it is only the non-linear quantum corrections that introduce non-trivial evolution, and initially the effects of this will be small. Though regardless, in the limit of zero h we should approach the expected convergence behavior; as shown in these figures, we *do* see this trend, though we have not quite reached the limiting behavior. This is because the truncation error becomes comparable to the machine roundoff error, the case of highest accuracy achievable in numerical computation, before the limit is reached.

As mentioned, reasons for the anomalous convergence behavior may be the compactification and special initial data we choose, namely regularized fields that are initially adapted to the classical solution. To check this, we evolved a test case where we imposed the initial conditions for $M = 11$, $N = 11$ at $z_c^+ = 0.25$ rather than $\mathcal{I}_R^-$. Note that this is not a physically correct solution as it will violate the constraints, though it is mathematically perfectly valid non-trivial initial data for the evolution equations. We set the domain of computation to $z_c^- \in [0.25, 0.5]$ and $z_c^+ \in [0.0, 0.25]$ to avoid any singular behavior. Using four meshes

48

for the Richardson extrapolation in this test, the truncation error was again reduced down to round-off level for even the coarser meshes, so for this test alone, we only employed three successively finer meshes in the extrapolation scheme; hence the resulting truncation error is expected to scale as h^6. The result is shown in Fig. 2.9, where we see the expected convergence. We also tested two-mesh Richardson extrapolation for the same case, and obtained the expected h^4 convergence.

2.3.3 Convergence of Physical Quantities on $\mathcal{I}_R^+$

The physical quantities we are interested in, including $y^-(z^-)$, F_{ATV} and M_B, are all functions of the fields, thus in theory they should inherit the convergence behavior of the fields. Some of these quantities require computing first and second derivatives of the fields, and so to maintain the theoretical convergence factor of 7, one should use 9-point finite difference stencils. However, catastrophic cancellation plagues the numerical derivatives near the last ray, as the regularized fields vary extremely slowly in this region, and this seems to be the limiting factor in the accuracy in which we can compute physical quantities. Though in general we do not need high order convergence of derived quantities to achieve high accuracy. A case-and-point is M_B, obtained by integrating F_{ATV}. F_{ATV} is dominated by round-off near the last ray in most cases, though, once integrated over y^-, this region contributes insignificantly to M_B. Furthermore, simple trapezoidal integration is adequate to achieve quite accurate estimates of M_B, as illustrated in Fig. 2.10.

2.3.4 Independent Residuals

As a final test of the code, we compute independent residuals of the differential equations (2.9) and (2.10). Specifically, we calculate the derivatives using three-point stencils centered at the mesh points, rather than the cell centered differences used for the solution. Three- point stencils limit the convergence of the independent residual to quadratic order, regardless of the convergence of the numerically calculated fields themselves. We observe

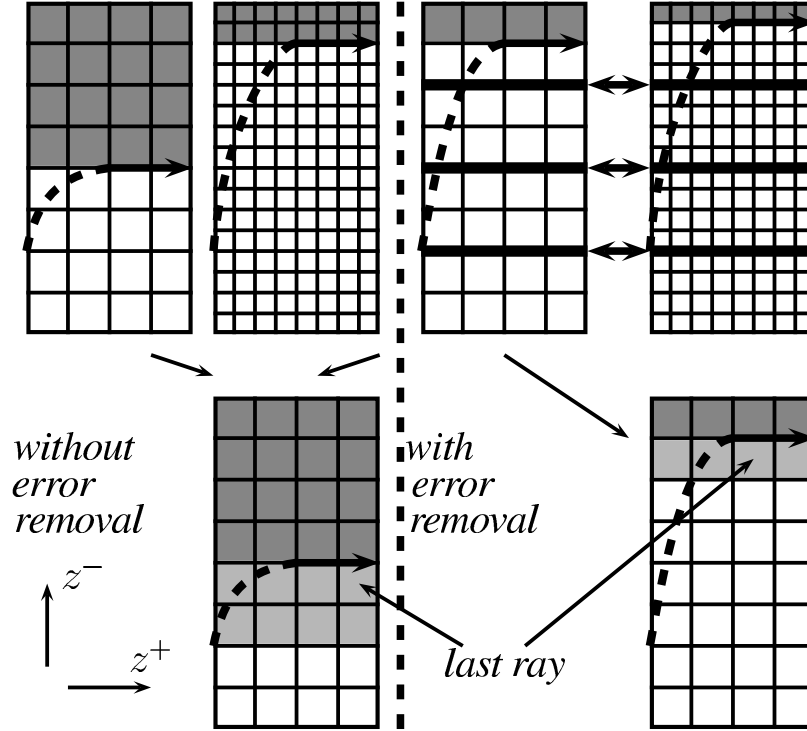the expected quadratic convergence in all cases.

Figure 2.3: Richardson extropolation without (left) and with (right) intermittent error removal for two meshes. The thick dashed line is the dynamical horizon, joining onto the last ray (horizontal arrow) where it meets the spacetime singularity. Left: Numerical solutions are evolved independently over the whole mesh (top two meshes) and the results are superposed (bottom mesh) according to the Richardson extrapolation after all evolutions are finished. The superposition is only meaningful where both of the meshes give meaningful results, i.e. before the last ray. The calculated position of the last ray depends on the numerical error, and typically occurs earlier in z^- for coarser meshes. The final superposition will also only be accurate where the truncation error is small on all meshes; approaching the singularity the truncation error grows without bound, hence there is some finite region (smaller with increasing resolution) before the last ray (light gray) where the Richardson extrapolation breaks down. Right: We determine several $z^- = constant$ *error removal lines* (dark horizontal lines), that divide the computational domain into regions. We evolve the fields in each mesh independently until the first error removal line is reached (at the end of the first region) and stop. We apply Richardson extrapolation to this region and update all the values on the coarsest mesh with the more accurate ones. Moreover, on the error removal line we also updated all finer meshes with the more accurate Richardson extrapolated values, using polynomial interpolation. We then restart the numerical evolution from the error removal line, continuing independently in each mesh until the next error removal line is reached, where the the procedure is repeated. In the end, this effectively provides a more accurate calculation of the position of the last ray on all meshes, enlarging the region of spacetime where a more accurate solution can be obtained through Richardson extrapolation.
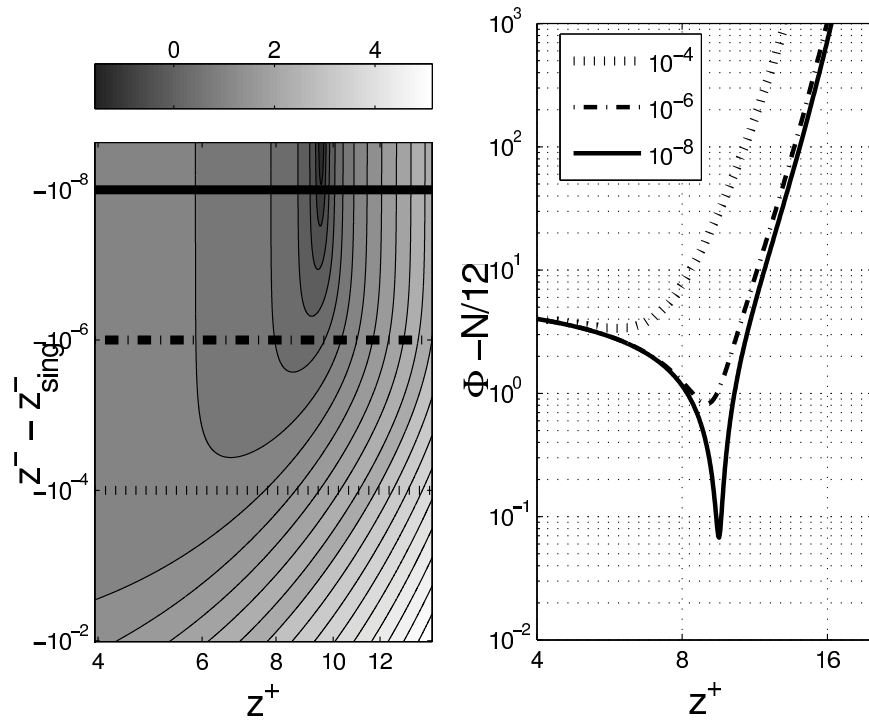
Figure 2.4: Φ for $M = 8$, $N = 24$. Left: Base-10 logarithm of $\Phi - \frac{N}{12}$. Right: $\Phi - \frac{N}{12}$ at lines of constant $z_{sing}^- - z^- = 10^{-4}, 10^{-6}, 10^{-8}$. This shows that Φ approaches $N/12$ at the location of the spacetime singularity, from where the last ray emanates. Specifically, here $\Delta z^- \sim 10^{-8}$ of the last ray.
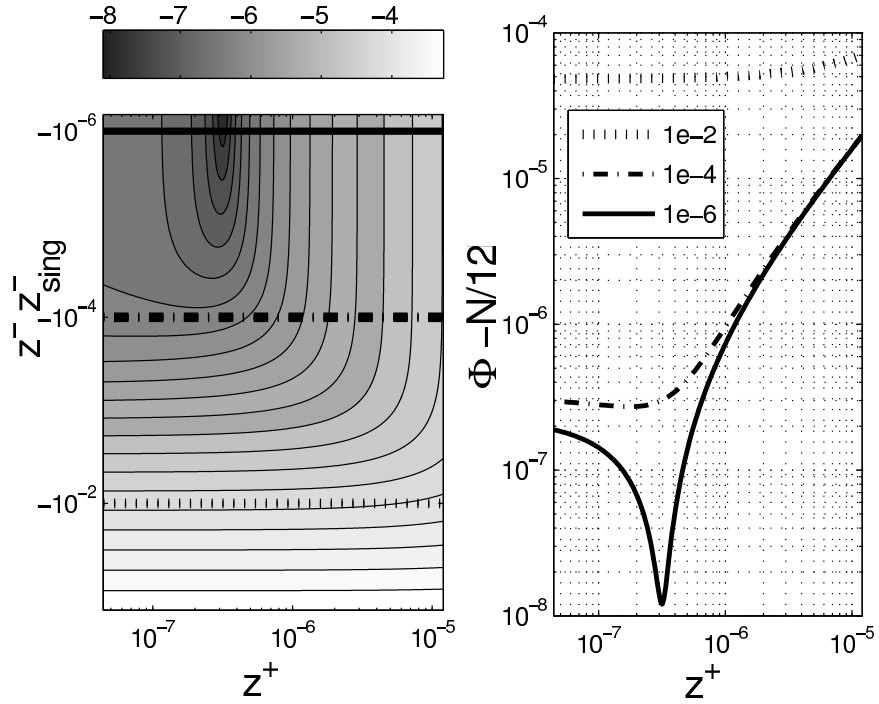
Figure 2.5: Φ for $M = 2^{-10}$, $N = 24$. Left: Base-10 logarithm of $\Phi - \frac{N}{12}$ Right: $\Phi - \frac{N}{12}$ at lines of constant $z^-_{sing} - z^- = 10^{-2}, 10^{-4}, 10^{-6}$. Again, as in Fig. 2.4, this shows that Φ approaches $N/12$, and we are close to the location of the last ray. Note that the field values are generally quite different from the $M = 8$ case, and the singularity appears very close to $z^+ = 0$, which necessitated the special compactification scheme explained in Sec. 2.2.1.
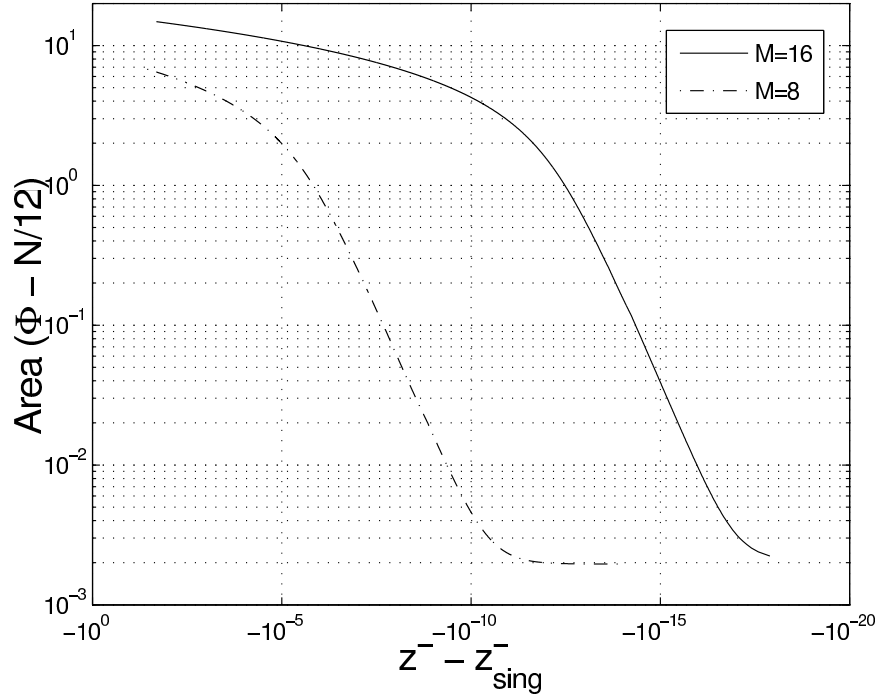
Figure 2.6: Area of the black hole ($\Phi - \frac{N}{12}$) vs. the uncompactified distance from the last ray in a log-log plot for $M = 8, 16$ and $N = 24$. Note that in terms of the uncompactified coordinates, we have to be within $\Delta z^- \sim 10^{-8}$ of the last ray in order to be truly close to the singularity for $M = 8$, and within $\Delta z^- \sim 10^{-16}$ for $M = 16$. This exponential trend is general and severely limits the upper value of M we can use in numerical calculations if we want to reach regions "close" to the singularity.
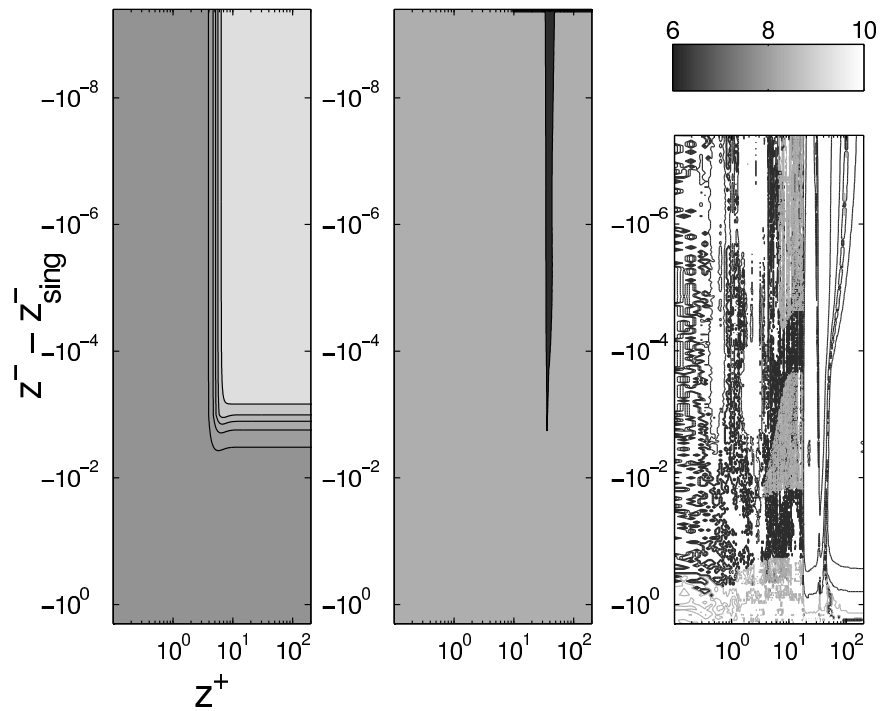
Figure 2.7: Convergence of $\bar{\phi}$ for the $M = 8$, $N = 24$ case: $n_e(z^{\pm})$ for $h = 2^{-10}$ (left) is mostly in the range $9 - 10$, and for $h = 2^{-11}$ (middle) is around 8. For $h = 2^{-12}$ (right) we reach machine round-off, and thus lose convergence, hence the "noisy" pattern.
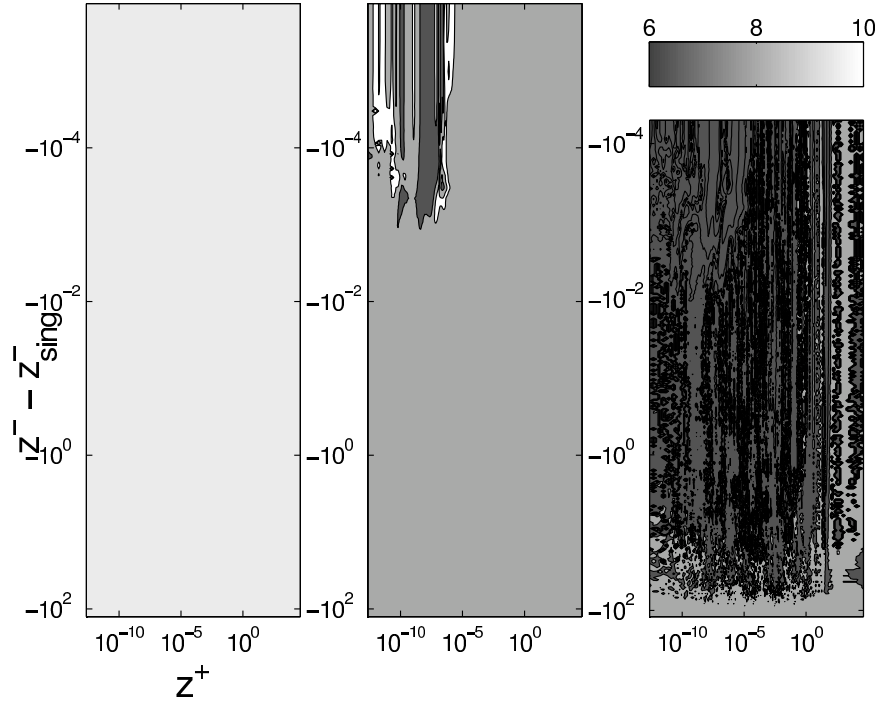
Figure 2.8: Convergence of $\bar{\phi}$ for the $M = 2^{-10}$, $N = 24$ case: $n_e(z^{\pm})$ for $h = 2^{-10}$ (left) is around 10, and for $h = 2^{-11}$ (middle) is around 8. Again, as with the $M = 8$ case in Fig. 2.7, for $h = 2^{-12}$ (right) machine round-off error begins to dominate the error, hence the "noisy" pattern. This effect is already visible in certain regions of the $h = 2^{-11}$ case. For lower mass black holes, round-off is reached with coarser meshes relative to the higher mass black holes.
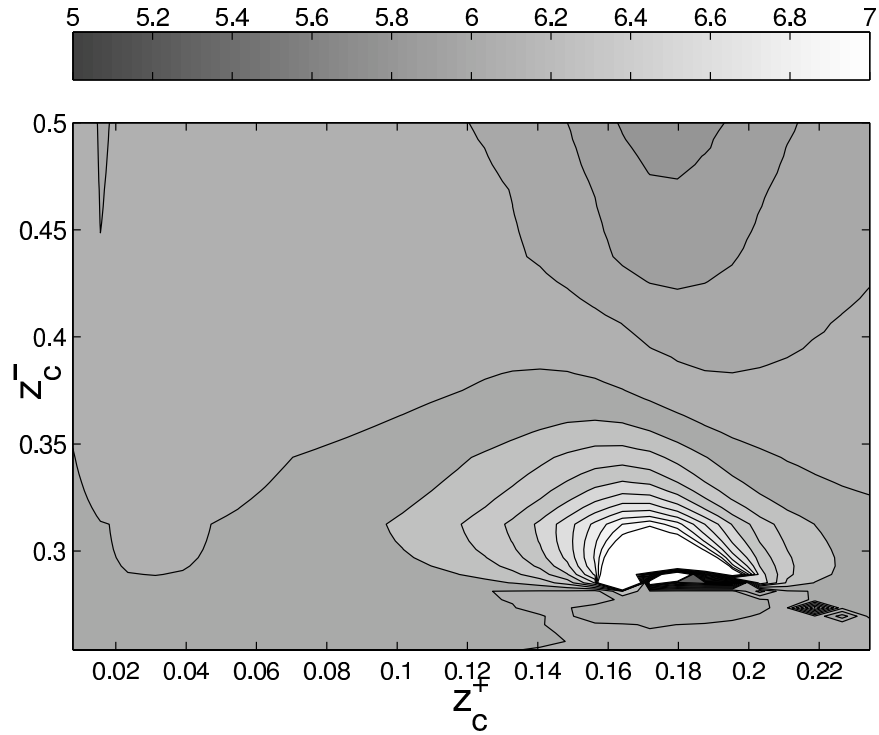
Figure 2.9: The convergence factor n_e of $\bar{\phi}$ for $h = 2^{-8}$ where as a test we imposed the (unphysical) initial conditions for $M = 11$, $N = 11$ at $z_c^+ = 0.25$ rather than $\mathcal{I}_R^-$. We only evolved the fields in the region $z_c^- \in [0.25, 0.5]$, $z_c^+ \in [0.0, 0.25]$. This solution is not physically relevant, though tests the behavior of the numerical code away from any of the null infinities or singularities. Here, for each base resolution, three meshes where used in the Richardson extrapolation scheme, which should give $O(h^6)$ convergence, and does to good approximation as shown in the figure.
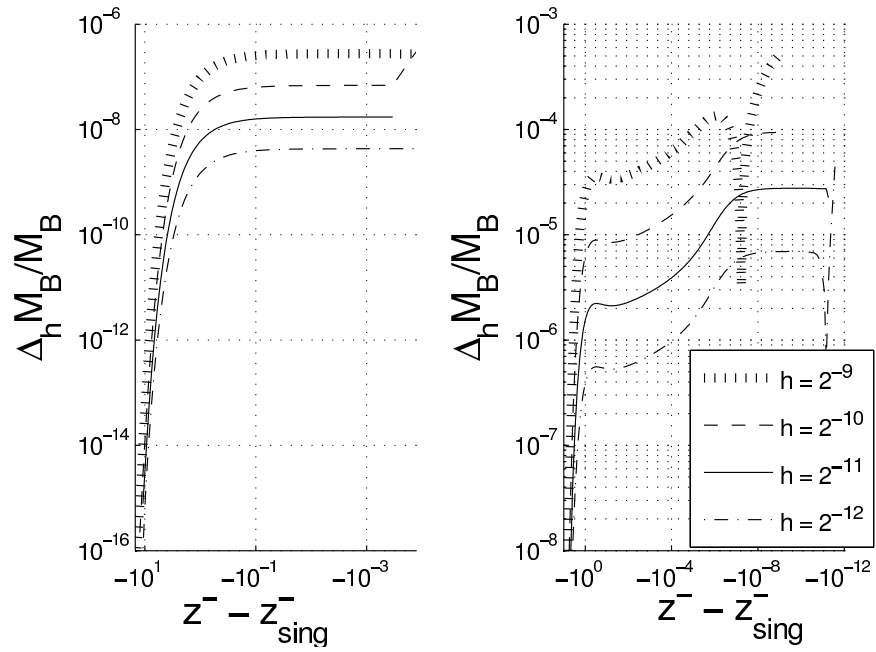
Figure 2.10: $\left| \frac{\Delta_h M_B}{M_B} \right|$ for various values of h for $M = 2^{-10}$ (left) and $M = 8$ (right). For most of the range, there is clear quadratic convergence. The dominant error here is from the trapezoidal integration method, and not a reflection of the truncation error from the numerical calculation of the fields.

Chapter 3

Physics of the CGHS Black Hole Evaporation

Recall that, all physical predictions of the mean-field theory arise from the set of 5 equations Eq. 1.26 – 1.30. The only difference from the classical theory lies in the fact that, because of the trace anomaly, right hand sides of the dynamical equations Eq. 1.27) and Eq. 1.28 are no longer zero. But this difference has very significant ramifications. In particular, it is no longer possible to obtain explicit analytical solutions; one has to take recourse to numerics.[1]

We have established in Chap. 2 that our numerical methods solve the CGHS equation with the mean-field approximation accurately and to a high precision. Now, we can start answering questions about black hole evaporation.

---

[1]There are variants of the CGHS model that are explicitly soluble, for example the RST (Russo-Susskind-Thorlacius) model [28], and the Bilal-Callan model [29]. However, results obtained in these models are not likely to be generic even in 2 dimensions because of their extra symmetries [10, 24]. More importantly, it was pointed out in [10, 12, 30] that the RST model is inconsistent even in the large N limit, and the Bilal-Callan model has a Hamiltonian that is unbounded from below. Thus though they exhibit many features of general 2D semi-classical black hole evaporation, they are physically less interesting than the CGHS model.

3.1 Overview

Let us first recall the standard paradigm. Literature on the quantum evaporation of CGHS black holes uses a certain definition of Bondi mass $M_{\text{Bondi}}^{\text{Trad}}$. Essentially every preceding paper assumed that: i) The semi-classical approximation is excellent until the horizon shrinks to Planck size; ii) Throughout this long phase, $M_{\text{Bondi}}^{\text{Trad}}$ is non-negative and the process is quasi-static; iii) Consequently, during this phase the quantum flux at $\mathcal{I}_{\text{R}}^{+}$ is given by the Hawking thermal flux and the semi-classical approximation holds; and iv) At the end of this phase the Bondi mass is also of Planck size. This depiction is reminiscent of the argument we mentioned in Sec. 1.1, namely, the fixed background metric picture holds until the mass of the black hole decreases to Planck scale. It is then difficult to imagine how purity of the incoming quantum state could be preserved in the outgoing state. However, our results show that several features of this scenario fail to be borne out by detailed calculations in the semi-classical theory. In particular, we will show the following results for a prompt[2] collapse of data with large ADM mass:

- The traditional Bondi mass, $M_{\text{Bondi}}^{\text{Trad}}$, in fact becomes *negative* (and large) even while the horizon area is macroscopic.

- The definition of $M_{\text{Bondi}}^{\text{Trad}}$ is taken directly from the classical theory where the black hole is static. Now, in 4 dimensions one knows [31] that the formula for the Bondi mass has to be modified in non-stationary space-times (from $\oint \Psi_2^o \, \mathrm{d}^2 V$ to $\oint (\Psi_2^o - \sigma \dot{\bar{\sigma}}) \, \mathrm{d}^2 V$). Indeed if one were to ignore this modification, one would find that neither the Bondi mass nor the Bondi flux is always positive. We have already showed that a quantum corrected Bondi mass, $M_{\text{Bondi}}^{\text{ATV}}$, is proposed in [13], in the CGHS mean-field theory (which, in particular, reduces to $M_{\text{Bondi}}^{\text{Trad}}$ in the classical theory). This mass remains *positive* throughout the evaporation process of the mean-field approximation.

- Although the horizon area goes to zero at the end of the evaporation process in the

---

[2]The meaning of a prompt collapse will be discussed in Chapter 4

mean-field approximation, $M_{\mathrm{Bondi}}^{\mathrm{ATV}}$ is *not* of Planck size at that time (i.e., at the point where the 'last ray' of Fig. 1.3 intersects $\mathcal{I}_{\mathrm{R}}^+$). For all black holes with large initial ADM mass, as the horizon area shrinks to zero $M_{\mathrm{Bondi}}^{\mathrm{ATV}}$ approaches a *universal* value $\approx 0.864\bar{N}$ in Planck units, with $\bar{N} = N/24$. This end point Bondi mass is macroscopic since N is necessarily large in the semi-classical theory.

- Dynamics *during* the evolution process also shows a *universal behavior*. For example, one can calculate $M_{\mathrm{Bondi}}^{\mathrm{ATV}}$ as a function of the horizon area $\mathbf{a}_{\mathrm{hor}}$. There is a transient phase immediately after the horizon is first formed, though after that the plot of $M_{\mathrm{Bondi}}^{\mathrm{ATV}}$ against $\mathbf{a}_{\mathrm{hor}}$ joins a universal curve all the way to zero area.

- The flux of energy radiated across $\mathcal{I}_{\mathrm{R}}^+$ departs from the thermal flux when $M_{\mathrm{Bondi}}^{\mathrm{ATV}}$ and even $\mathbf{a}_{\mathrm{hor}}$ are macroscopic.

- Although the Ricci scalar of the mean-field metric g diverges at the (weak) singularity, it is regular on the last ray and goes to zero as one approaches $\mathcal{I}_{\mathrm{R}}^+$ along this ray. Thus, contrary to a wide spread belief, there is no 'thunderbolt' curvature singularity in the semi-classical theory.

We will see in Chap. 4 that our results strongly suggest that the S matrix from $\mathcal{I}_{\mathrm{L}}^-$ to $\mathcal{I}_{\mathrm{R}}^+$ is likely to be unitary. However, *because of the universality* of physical quantities at $\mathcal{I}_{\mathrm{R}}^+$, it is very unlikely that information in the infalling matter at $\mathcal{I}_{\mathrm{R}}^-$ will be recovered in the outgoing state at $\mathcal{I}_{\mathrm{R}}^+$. This is in sharp contrast with a wide-spread expectation; indeed, mechanisms for information recovery have been suggested in the past (see e.g. [22]). This expectation illustrates the degree to which universality was unanticipated in much of the CGHS literature.

In the following two sections, we will consider a collapsing $\delta-$function shock wave, as in Eq. 1.34, which will be followed by a discussion on initial data with extended profiles.

3.2 Shell Collapse: Anticipated Behavior
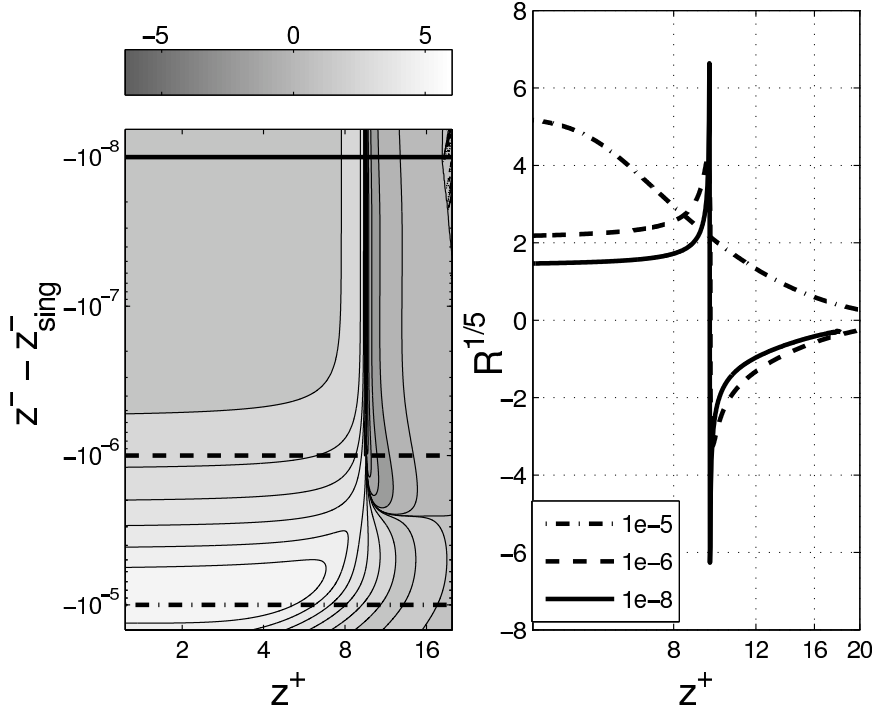
Figure 3.1: The Ricci scalar R for $M^\star = 8$. Left: 2D contour plot of $R^{1/5}$ showing the increase in R as the singularity (dark vertical region near the middle) is approached and the asymptotically flat region ($R \to 0$) near $\mathcal{I}_R^+$ ($z^+ \to \infty$). Right: $R^{1/5}$ as a function of z^+ on the lines $z^- - z^-_{\mathrm{sing}} = -10^{-5}, -10^{-6}, -10^{-8}$ (marked on the left panel as horizontal lines), showing a double peak, indicating the divergent behavior of $\partial_+\partial_-\Phi$ at the singularity. The fact that the peak is narrow rules out a strong thunderbolt singularity. Note that the dark color at the region of the singularity is due to the high density of contour lines, and not directly due to negative values of R. While naive numerical calculation of R very close to $\mathcal{I}_R^+$ does not yield reliable results due to catastrophic cancelation, it is already very small in the high z^+ values shown here, and the trend towards 0 is clear.

Asymptotic flatness at $\mathcal{I}_R^+$: First, Θ, Φ do indeed satisfy the asymptotic conditions Eq. 1.37. This was also noted in the recent approximate solution to the CGHS equations by Ori [25]. The simulations provide values of the functions $A(z^-), B(z^-)$ and $y^-(z^-)$. As a consistency check on the simulation, we verified the balance law Eq. 1.40 by calculating separately the right and left sides of this equation as close to the last ray as the numerical solution gave reliable (convergent) results. We also computed the scalar curvature R of the mean-field metric g, and it does go to zero at $\mathcal{I}_R^+$—see Fig. 3.1 for an example.
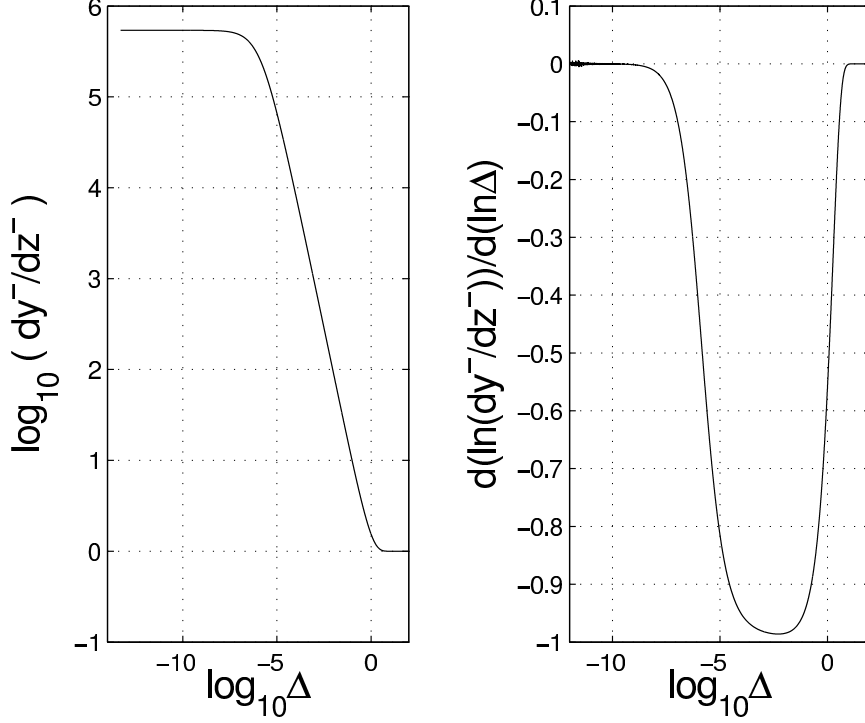
Figure 3.2: Left: Plot of $\log_{10}(\mathrm{d}y^-/\mathrm{d}z^-)$ vs $\log_{10}\Delta$ for $M^\star = 8$, $\bar{N} = 1$, where $\Delta = \left(z^-_{\mathrm{sing}} - z^-\right)$. Right: Slope of the curve on the left. If locally the function on the left behaves as $\sim (\kappa\Delta)^{-p}$, the curve on the right shows $-p$. In the distant past (rightmost region in both plots), y^- tends to z^-. The intermediate region is similar to that in the classical solution where $(\mathrm{d}y^-/\mathrm{d}z^-) \sim (\kappa\Delta)^{-1}$. As the last ray is further approached (leftmost region), we see that $(\mathrm{d}y^-/\mathrm{d}z^-)$ increases much slower than $(\kappa\Delta)^{-1}$, leading to a finite value for y^- at the last ray.

Finiteness of y^- at the last ray: In the classical solution, the affine parameters $\underline{y}^-$ along $\mathcal{I}^+_{\mathrm{R}}$ and z^- along $\mathcal{I}^-_{\mathrm{L}}$ defined by $\underline{g}$ are related by

$$e^{-\kappa\underline{y}^-} = e^{-\kappa z^-} - \frac{GM}{\kappa} \ . \tag{3.1}$$

Hence $\underline{y}^- = \infty$ at $\kappa z^- = -\ln(GM/\kappa)$. This is the point at which the singularity and the event horizon meet $\mathcal{I}^+_{\mathrm{R}}$ (see Fig 1.2). Thus, in the classical solution $\mathcal{I}^+_{\mathrm{R}}$ is complete but, in a precise sense, smaller than $\mathcal{I}^-_{\mathrm{L}}$. For a test quantum field $\hat{f}_-$ on the classical solution, one then has to trace over modes residing on the part of $\mathcal{I}^-_{\mathrm{L}}$ which is missing from $\mathcal{I}^+_{\mathrm{R}}$. This fact is directly responsible for pure states on $\mathcal{I}^-_{\mathrm{L}}$ to evolve to mixed states on $\mathcal{I}^+_{\mathrm{R}}$, i.e.,

for the non-unitarity of the S-matrix [13, 17] of the test field (recall Sec. 1.4). What is the situation in the mean-field theory? Our analysis shows that, as generally expected, the affine parameter w.r.t. the mean field metric g takes a *finite* value at the last ray on $\mathcal{I}_{\mathrm{R}}^{+}$; a necessary condition for unitarity of the S-matrix is met.

Our numerical solution cannot reach the last ray, since it is in the future of the singularity. The best we can do is getting as close to it as possible, before the singularity causes our numerical evolution to stop. To establish the finiteness of $\underline{y}^{-}$, we need to know the functional behavior of $\underline{y}^{-}(z^{-})$ in the vicinity of the last ray[3]. Let us return to the classical solution $\underline{g}$ and set

$$\kappa z_{\mathrm{sing,cl}}^{-} = -\ln(GM/\kappa) \quad \text{and} \quad \Delta_{\mathrm{cl}} = z_{\mathrm{sing,cl}}^{-} - z^{-} . \tag{3.2}$$

(The subscript 'sing,cl' just highlights the fact that this is the point at which the classical singularity meets $\mathcal{I}_{\mathrm{R}}^{+}$.) Then we have

$$\underline{y}^{-} = z^{-} - \frac{1}{\kappa} \ln\left(1 - e^{-\kappa\Delta_{\mathrm{cl}}}\right) . \tag{3.3}$$

When Δ_{cl} tends to zero, $\underline{y}^{-}$ is dominated by the leading order term $-(1/\kappa)\ln(-\kappa\Delta_{\mathrm{cl}})$ which diverges at $\Delta_{\mathrm{cl}} = 0$. This logarithmic divergence is coded in the power -1 in the expression of the derivative $(\mathrm{d}\underline{y}^{-}/\mathrm{d}z^{-})$:

$$\frac{\mathrm{d}\underline{y}^{-}}{\mathrm{d}z^{-}} = (\kappa\,\Delta_{\mathrm{cl}})^{-1} + \text{finite terms} . \tag{3.4}$$

If we had $(\kappa\,\Delta_{\mathrm{cl}})^{-p}$ on the right side rather than $(\kappa\,\Delta_{\mathrm{cl}})^{-1}$, then $\underline{y}^{-}$ would have been finite at the future end of $\mathcal{I}_{\mathrm{R}}^{+}$ of $\underline{g}$ for $p < 1$ (as then $\underline{y}^{-} = (\kappa\,\Delta_{\mathrm{cl}})^{1-p}/(1-p) +$ finite terms).

In the mean-field theory, the last ray starts at the end point of the singularity and meets $\mathcal{I}_{\mathrm{R}}^{+}$ of g at its future end point. We will denote it by the line $z^{-} = z_{\mathrm{sing}}^{-}$. Following the

---

[3]Note that quantities with an under bar are those of the the classical case, and the ones without it correspond to the MFA calculation

above discussion, to show that the affine parameter y^- w.r.t. g is finite at $z^- = z^-_{\text{sing}}$ we focus on the behavior of $(\mathrm{d}y^-/\mathrm{d}z^-)$ near this future end point of $\mathcal{I}^+_{\text{R}}$. More precisely, we analyze the functional behavior of $(\mathrm{d}y^-/\mathrm{d}z^-)$ and determine a local p extracted from the logarithmic derivative of $(\mathrm{d}y^-/\mathrm{d}z^-)$ with respect to $\Delta \equiv z^-_{\text{sing}} - z^-$. Results in Fig. 3.2 show that $(\mathrm{d}y^-/\mathrm{d}z^-)$ grows much slower near the last ray in the mean-field theory than it does in the classical theory. In fact, over the entire range of $\mathcal{I}^+_{\text{R}}$ the local estimate of p is strictly less that 1, and asymptotes to 0 approaching the last ray. This implies that y^- is finite at the last ray in the mean-field theory.

Note that the above analysis is only valid if we have determined the location of the singularity with sufficient accuracy such that the numerical uncertainty in its location is much smaller than the range in Δ where we extract the asymptotic behavior of the function. From convergence studies, we estimate our precision in determining z^-_{sing} to be at the order of 10^{-13}, and hence all the values in Fig. 3.2 are sufficiently far from the last ray to provide a reliable measure of the power p.

3.3   Shell collapse: Unforeseen Behavior

The numerical calculations also revealed a number of surprises which we now discuss.

Bondi mass for large $\bar{N}$: Scaling properties discussed in section 1.3.5 imply that if the Bondi mass at the last ray is non-zero, it will be macroscopic for a sufficiently large N. This expectation is borne out (in particular the Bondi mass *is* non-zero) in all our simulations with large M_{ADM} and large $\bar{N}$. Fig.   3.3 summarizes the result of a simulation where $N = 720$ and $M_{\text{ADM}} = 360$ (so $\bar{N} = 30$ and $M^\star = 12$). The Bondi mass, $M^{\text{Trad}}_{\text{Bondi}}$, that has been commonly used in the literature [8, 12, 18, 21, 22, 23, 24] becomes negative even far from the last ray when the horizon area is still macroscopic, and has a macroscopic negative value at the last ray.[4] On the other hand, the more recent $M^{\text{ATV}}_{\text{Bondi}}$ [13, 17] remains strictly

---

[4]After this work was completed, Javad Taghizadeh Firouzjaee pointed out to us that the fact that the traditional Bondi mass can become negative was already noticed in [23]. Again though, in our terminology
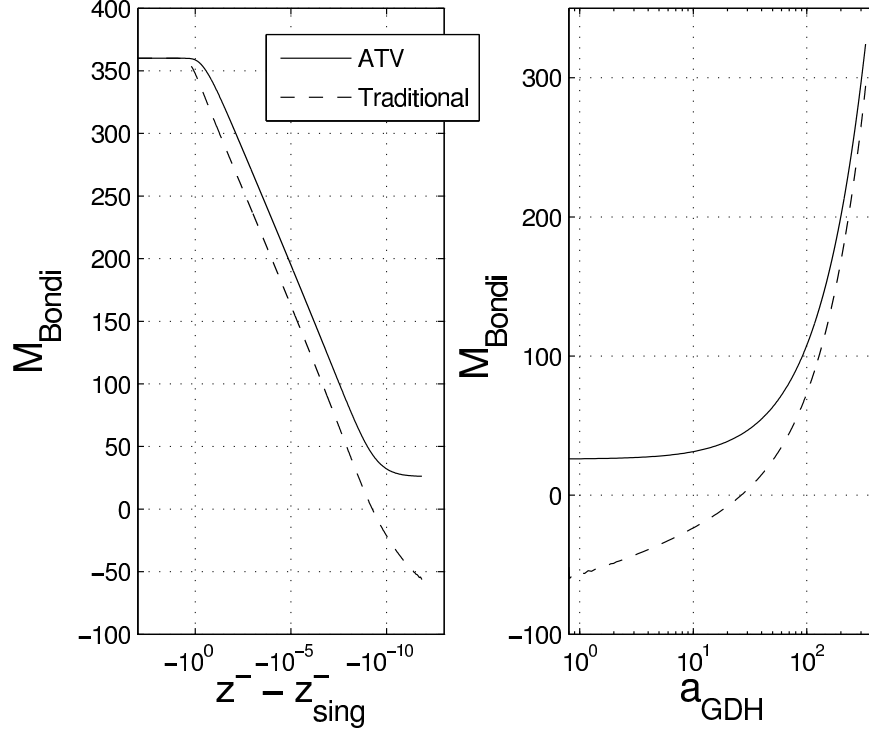
Figure 3.3: The ATV Bondi mass $M_{\text{Bondi}}^{\text{ATV}}$ (solid lines) and the traditional Bondi mass $M_{\text{Bondi}}^{\text{Trad}}$ (dashed lines) are plotted against $z^- - z_{\text{sing}}^-$ (left) and the horizon area (right). This simulation corresponds to $M_{\text{ADM}} = 360$, $N = 720$ (so $M^\star = 12$). For high values of N, both formulas give a large non-zero Bondi mass at the last ray. $M_{\text{Bondi}}^{\text{Trad}}$ becomes negative when the area is still macroscopic. On the other hand $M_{\text{Bondi}}^{\text{ATV}}$ remains strictly positive all the way to the last ray, where the generalized dynamical horizon (GDH) shrinks to zero area.

positive. As one would expect from the scaling relations, because N is large, $M_{\text{Bondi}}^{\text{ATV}}$ is also macroscopic at the last ray.

Universality of the end state: Fig 3.4 shows a plot of $m^\star$, the value of $(M_{\text{Bondi}}^{\text{ATV}}/\bar{N})$ at the last ray, against $M^\star = (M_{\text{ADM}}/\bar{N})$, for several values of the initial $M^\star > 1$. The curve that fits the data, shown in the figure, is

$$m^\star = \alpha \left(1 - e^{-\beta(M^\star)^\gamma}\right) \tag{3.5}$$

the numerical simulation in that work corresponds to a microscopic black hole with $M^\star = 1\, M_{\text{Pl}}$.

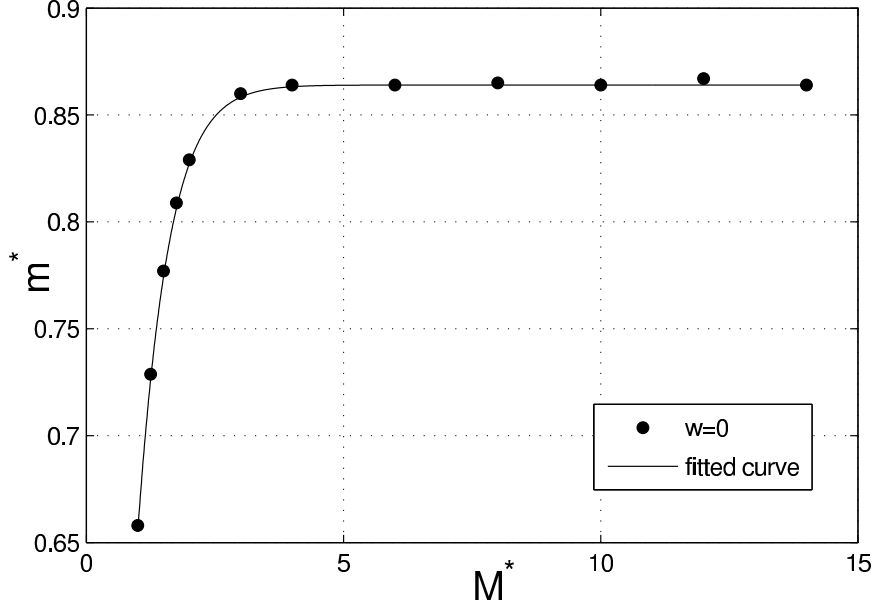Figure 3.4: The value of $m^\star$ (i.e. $M^{\text{ATV}}_{\text{Bondi}}/\bar{N}$ at the last ray) is plotted against $M^\star$ (which equals $M_{\text{ADM}}/\bar{N}$) for $M^\star \geq 1$. For Macroscopic $M^\star$ (actually, already for $M^\star \gtrsim 4$!) $m^\star$ has a universal value, approximately 0.864.

with specific values for the constants α, β, γ

$$\alpha \approx 0.864, \ \beta \approx 1.42, \ \gamma \approx 1.15\,.$$

It is visually clear from the plot that there is a qualitative difference between $M^\star \gtrsim 4$ and $M^\star \lesssim 4$. Physically this can be understood in terms of $\mathbf{a}_{\text{initial}}$, the area of the first marginally trapped surface: Eq. 1.36 implies that $\mathbf{a}^\star_{\text{initial}} = \mathbf{a}_{\text{initial}}/\bar{N}$ can be greater than a Planck unit only if $M^\star$ is larger than 3. It is therefore not surprising that $M^\star = 4$ should serve as the boundary between macro and Planck regimes. Indeed, as Fig 3.4 shows, if $M^\star \gtrsim 4$, the value of the end point Bondi mass is universal, $m^\star \approx 0.864$. For $M^\star \lesssim 4$ on the other hand, the value of $m^\star$ depends sensitively on $M^\star$. This could have been anticipated because if $M^\star \leq 3$, what evaporates is a GDH which *starts out* with one Planck unit or less of area $\mathbf{a}^\star$. *Thus, in the mean-field approximation it is natural to regard CGHS black holes with $M^\star \gtrsim 4$ as macroscopic and those with $M^\star \lesssim 4$ as microscopic.*

Finally, for macroscopic black holes, the end-value of the traditional Bondi-mass is also universal: $M_{\text{Bondi}}^{\text{Trad}} < \mathbf{a}_{\text{hor}}$ and $(M_{\text{Bondi}}^{\text{Trad}}/\bar{N}) \to -2.0$ as $\mathbf{a}_{\text{hor}} \to 0$.

As noted in Chap. 2, there have been a number of previous numerical studies of the CGHS model [21, 10, 23, 24]. They clarified several important dynamical issues. However they could not unravel universality because they all focused on cases where the black hole is microscopic already at its inception: $M^\star \leq 2.5$ in [21], $M^\star = 1$ in [10] and [23] and $M^\star = 0.72$ in [24]. This limitation was not noticed because the scaling symmetry and its significance was not appreciated.
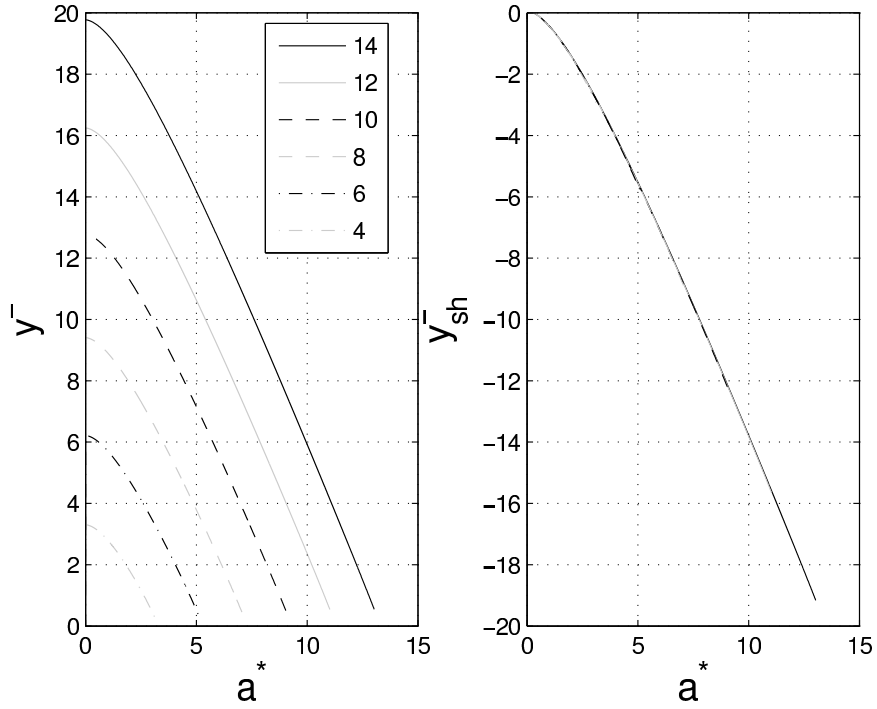
Figure 3.5: Left: The affine parameter y^- (defined in Eq. (1.38)) of the physical metric g is plotted against the rescaled area $\mathbf{a}^\star := (\mathbf{a}_{\text{GDH}}/\bar{N})$ of the generalized dynamical horizon (given by $(\Phi/\bar{N} - 2)$) at the horizon for values of $M^\star$ from 4 to 14. Even though the curves are very similar in shape, they do not coincide. Right: Once the shifting freedom in y^- is utilized, we see that a properly shifted version y_{sh}^- is universal with respect to $\mathbf{a}^\star$ for all macroscopic $M^\star$ values. y_{sh}^- can be used as a universal coordinate similar to the horizon area.

Dynamical universality of y^-: The horizon area $\mathbf{a}_{\text{GDH}}$ (more precisely, its negative) provides an invariantly defined time coordinate to test dynamical universality of other physical

quantities. Let us begin with y^-, the affine parameter along $\mathcal{I}_R^+$ with respect to the physical metric g defined in Eq. 1.38. Fig. 3.5, left, shows the plot of y^- against $\mathbf{a}^\star := (\mathbf{a}_{\mathrm{GDH}}/\bar{N})$ for various values of $M^\star$. These plots show that the time dependence of y^- for various values of M^* is very similar but not identical. Recall, however, that there is some freedom in the definition of the affine parameter. In particular, in each space-time we can shift it by a constant, and the particular value of the constant can vary from one space-time to the next (e.g. depend on the ADM mass). This shift does not affect any of our considerations, including the balance law Eq. 1.40.

Let us define y_{sh}^- by shifting each y^- so that each solution reaches the same small non-zero value of the horizon area, $\mathbf{a}^\star = \epsilon$, at the same y_{sh}^-. It turns out that this shift has the remarkable feature that, for initially macroscopic black holes, all shifted curves now coincide for *all* values of $\mathbf{a}^\star$. Thus, we have a universal, monotonic function of $\mathbf{a}^\star$ plotted in Fig. 3.5, right. Hence y_{sh}^- also serves as an invariant time coordinate. In fact it has an advantage over $\mathbf{a}_{\mathrm{GDH}}$: whereas $\mathbf{a}^\star$ is defined only after the first marginally trapped surface is formed (see Fig 1.3), y_{sh}^- is well defined throughout the mean-field space-time (M, g).

Dynamical Universality of F^{ATV} and $M_{\mathrm{Bondi}}^{\mathrm{ATV}}$: We can repeat the procedure used above for y^- to investigate if dynamics of other physical quantities such as the Bondi flux $F^\star := (F^{\mathrm{ATV}}/\bar{N})$ and the Bondi mass $M_{\mathrm{Bondi}}^\star := (M_{\mathrm{Bondi}}^{\mathrm{ATV}}/\bar{N})$ are also universal. Note, however, that unlike y^-, there is no 'shift' (or indeed any other) freedom in the definitions of F^{ATV} and $M_{\mathrm{Bondi}}^{\mathrm{ATV}}$. So, if there is universality, it should emerge directly, *without any adjustments*, in the plots of $F^\star$ and $M_{\mathrm{Bondi}}^\star$ against $\mathbf{a}^\star = (\mathbf{a}_{\mathrm{GDH}}/\bar{N})$ or y_{sh}^-.

Let us begin with the Bondi flux. Recall, first, that in the external field approximation [12, 32], the energy flux is very small in the distant past, rises steeply at $\kappa y^- \approx -\ln(GM_{\mathrm{ADM}}/\kappa)$ and then quickly asymptotes to the Hawking value $F^{\mathrm{Haw}} = (\bar{N}\hbar\kappa^2/2)$. This constant flux is characteristic of thermal radiation at temperature $\kappa\hbar$ in two space-time dimensions. In our simulations (with $N = 24$, or) $\bar{N} = 1$ and $\hbar = \kappa = 1$, it corresponds to $F^{\mathrm{Haw}} = 0.5$.
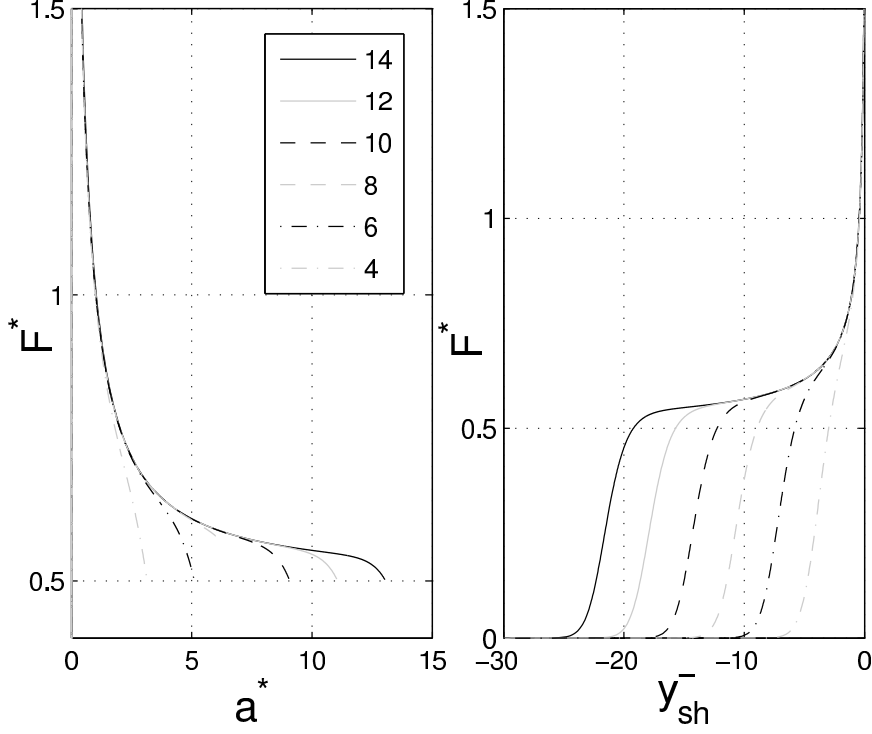
Figure 3.6: $F^\star = (F^{\mathrm{ATV}}/\bar{N})$ is plotted against the horizon area $\mathbf{a}^\star := (\mathbf{a}_{\mathrm{GDH}}/\bar{N})$ (left) and y_{sh}^- (right) for values of $M^\star$ from 4 to 14. For all $M^\star$ values, $F^\star$ starts at the value of 0 at the distant past ($\kappa y_{\mathrm{sh}}^- \ll -1$), and then joins a universal curve of $F^\star$. Note that once the GDH is formed, (the rightmost beginning of each curve on the left plot) $F^\star$ is already slightly larger in magnitude than the Hawking/thermal value 0.5 and it increases steadily as one approaches the last ray (i.e. as $\mathbf{a}_{\mathrm{GDH}}$ and y_{sh}^- approach 0.

In the mean-field theory, numerical simulations show that, for all initially macroscopic black holes, the energy flux $F^\star := (F^{\mathrm{ATV}}/\bar{N})$ is also negligibly small in the distant past and then rises steeply. But this rise is now associated with a clearly identifiable dynamical process: formation of the first marginally trapped surface. As we noted in section 1.3.4 , for a shell collapse, analytical calculations show that the area of this first surface is given by Eq. 1.36. Assuming that we have a macroscopic initial mass, $M^\star \gg \sqrt{G\hbar}\, M_{\mathrm{Pl}} =: \tilde{M}_{\mathrm{PL}}$, Eq. 1.36 simplifies:

$$\mathbf{a}_{\mathrm{initial}}^\star \approx G\hbar\Big[\frac{M^\star}{\tilde{M}_{\mathrm{Pl}}} - 1 + \frac{\tilde{M}_{\mathrm{Pl}}}{2M^\star} + \dots\Big] \tag{3.6}$$

This relation is borne out in simulations. Assuming that the black hole is very large at this stage, heuristically, one can equate the area of this new born GDH with the Bondi mass at
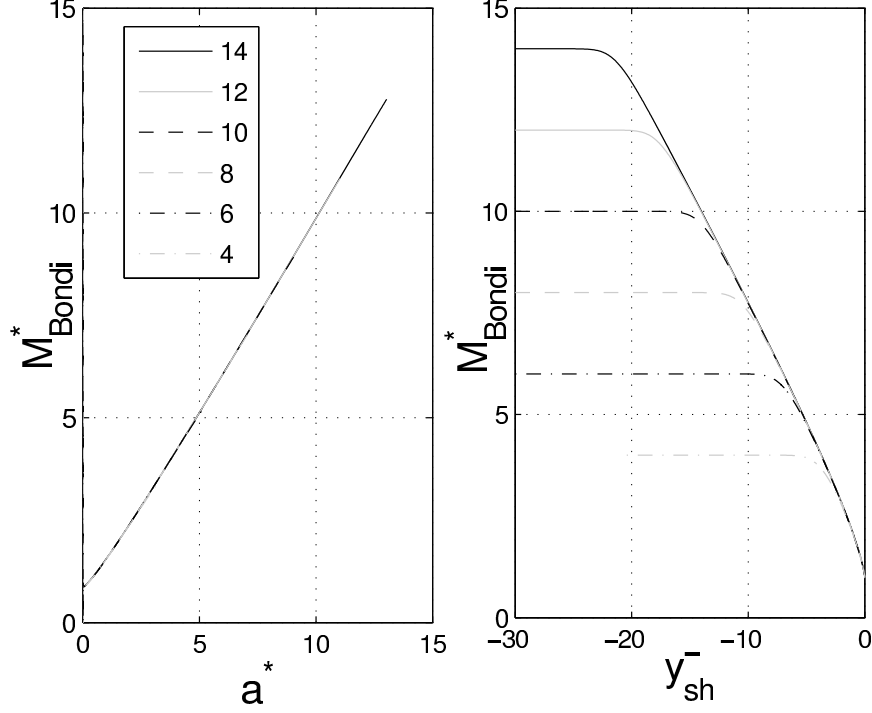
Figure 3.7: $M^\star_{\mathrm{Bondi}} = (M^{\mathrm{ATV}}_{\mathrm{Bondi}}/\bar{N})$ is plotted against the horizon area $\mathbf{a}^\star := (\mathbf{a}_{\mathrm{GDH}}/\bar{N})$ (left) and y^-_{sh} (right) for values of $M^\star$ from 4 to 14. For all these macroscopic $M^\star$, $M^\star_{\mathrm{Bondi}}$ starts at the value of M_{ADM} in the distant past ($\kappa y^-_{\mathrm{sh}} \ll -1$), and then joins a universal curve of $M^\star_{\mathrm{Bondi}}$. When the dynamical horizon first forms $M^\star_{\mathrm{Bondi}}$ is quite close to its initial value of $M^\star$, (This is difficult to see in the left plot where all the curves crowd.) This means that almost all of the evaporation occurs after the formation of the dynamical horizon.

the retarded instant of time, say $y^- = y^-_o$, at which it is born. This implies that, per scalar field, only ~ 1 Planck unit of $M^\star_{\mathrm{Bondi}}$ has been radiated over the long period of time from $y^- = -\infty$ till $y^- = y^-_o$. But once the GDH appears, the flux rises steeply to a value close to but higher than 0.5. Then, it joins a universal curve all the way to the last ray where the area $\mathbf{a}^\star$ shrinks to zero. Thus, after a brief transient phase around the time the GDH is first formed, the time-dependence of the Bondi flux is universal. Fig. 3.6, left shows this universal time dependence with $\mathbf{a}^\star$ as time and Fig. 3.6, right shows it with y^-_{sh} as time.

In virtue of the balance law (1.40) one would expect this universality to imply a universal time dependence also for the Bondi mass $M^\star_{\mathrm{Bondi}}$. This is indeed the case. At spatial infinity i^o_{R}, we have $M^\star_{\mathrm{Bondi}} = M^\star$. There is a transient phase around the birth of the GDH

in which the Bondi mass decreases steeply. Quickly after that, the time dependence of $M^{\star}_{\mathrm{Bondi}}$ follows a universal trajectory until the last ray. Fig. 3.7, left shows this universality with $\mathbf{a}^{\star}$ as time while Fig. 3.7, right shows it with y^{-}_{sh} as time.

To summarize, using either $\mathbf{a}^{\star}$ or y^{-}_{sh} as an invariant time coordinate, we can track the dynamics of $F^{\star}$ and $M^{\star}_{\mathrm{Bondi}}$. In each of the four cases, there is a universal curve describing these dynamics. For definiteness let us use $\mathbf{a}^{\star}$ as time and focus on $M^{\star}_{\mathrm{Bondi}}$ (the situation is the same in the other three cases). Since both quantities are positive, let us consider the time-mass quadrant they span. Fix a very large initial black hole with $M^{\star} = M^{\star}_o$ and denote by c_o the curve in the quadrant that describes its time evolution. Then, given any other black hole with $M^{\star} < M^{\star}_o$, the curve c describing the dynamical evolution of its $M^{\star}_{\mathrm{Bondi}}$ starts out at a smaller value of time (i.e. $\mathbf{a}^{\star}$) marking the birth of the GDH of that space-time and, after a brief transient phase, joins the curve c_o all the way until its horizon shrinks to zero. Here we have focused on the ATV flux and mass because their properties make them physically more relevant. But this universality holds also for the flux and mass expressions, F^{Trad}, $M^{\mathrm{Trad}}_{\mathrm{Bondi}}$ that have been traditionally used in the literature.

Curvature at the last ray: There has been considerable discussion on the nature of the geometry at the last ray. Since this ray starts out at the singularity, a natural question is whether a curvature singularity propagates out all along the last ray to $\mathcal{I}^{+}_{\mathrm{R}}$. This would be a 'thunderbolt' representing a singular Cauchy horizon [24]. If it were to occur, the evolution across the last ray would not just be ambiguous; it would be impossible. However, *a priori* it is not clear that a thunderbolt would in fact occur. For, the 'strength' of the singularity goes to zero at its right end point where the last ray originates.

Using numerical simulations, Hawking and Stewart [24] argued that a thunderbolt does occur in the semi-classical theory. But they went on to suggest that it could be softened by full quantum gravity, i.e., that full quantum gravity effects would tame it to produce possibly a very intense but finite burst of high energy particles in the full theory.

Our calculation of the Ricci scalar very close to the last ray shows that, except for a

small region near the singularity, the scalar curvature at the last ray is *not* large (Fig. 3.1). Thus, our more exhaustive and high precision calculations rule out a thunderbolt singularity in the original sense of the term. This overall conclusion agrees with the later results in [21]. (Both these calculations were done only for initially microscopic black holes while results hold also for macroscopic ones.) However, our calculations show that the flux F^{ATV} does increase very steeply near the last ray (see Fig. 3.6). Numerically, we could not conclude whether the flux remains finite at the last ray or diverges. However, the integrated flux which determines the change in $M^{\mathrm{ATV}}_{\mathrm{Bondi}}$ is indeed finite and in fact *not very significant* in the region very near the last ray. For macroscopic $M^{\star}$ values, the total radiated energy after the point when $F^{\star}$ reaches the value 1 is ~ 1 Planck mass. (see Figs. 3.6, 3.7). Thus, if we were to associate the thunderbolt idea to the steep increase of flux at the last ray, this would have to be in quite a weak sense; in particular, there is no singular Cauchy horizon.

Nature of the Bondi flux: Recall that in the external field approximation, the energy flux starts out very low, rapidly increases and approaches $(F^{\mathrm{Haw}}/\bar{N}) = \hbar\kappa^2/2$, the constant thermal value ($= 0.5$ in our simulations), from below [32, 12] (see Eq. 1.24). In the mean-field theory, the flux F^{ATV} also starts out very small and suddenly increases when the GDH is first formed. However, it overshoots the thermal value and ceases to be constant much before the black hole shrinks to Planck size (Fig. 3.6). During subsequent evolution, F^{ATV} monotonically increases in magnitude and is about 70% greater than the constant thermal value F^{Haw} when $M^{\mathrm{ATV}}_{\mathrm{Bondi}} \sim 2\bar{N}M_{\mathrm{Pl}}$: the standard assumption that the flux is thermal till the black hole shrinks to Planck size is not borne out in the mean field theory. (One's 4-dimensional intuition may lead one to think that the increase in the flux merely reflects that the black hole gets hotter as it evaporates; but this is not so because the temperature of a CGHS black hole is an *absolute constant*, $T_{\mathrm{Haw}} = \kappa\hbar$). In the interval between the formation of the GDH and the time when $M^{\mathrm{ATV}}_{\mathrm{Bondi}}$ approaches $\bar{N}M_{\mathrm{Pl}}$, the numerical flux is

well approximated by

$$F^{\text{ATV}} = F^{\text{Haw}} \left[1 - \ln \left(1 - \frac{\bar{N} M_{\text{Pl}}}{M_{\text{Bondi}}^{\text{ATV}}} \right) \right].$$ (3.7)

Thus, in this interval the flux is close to the constant thermal value only while the area **a** of the GDH is much greater than $\bar{N}$ Planck units.[5] We will give the details of the derivation of Eq. 3.7 in Appendix. A.

3.4 Universality beyond the shell collapse.

So far, we have focused our attention on a delta distribution shell collapse (Eq. 1.34). As we will discuss more in the following section, we expect the results to be robust for a large class of infalling profiles, so long as the GDH forms promptly. To test this conjecture, we evolved a 2-parameter family of initial data, parameterized by a characteristic initial mass M and width w. Now, it is clear from the form Eq. 1.32), 1.33 of initial data that what matters is not the profile $f_+^{(o)}$ itself but rather the integral of $(\partial_+ f_+^{(o)})^2$. We will specify it using two parameters, M and w:

$$\int_0^{\bar{x}^+} \mathrm{d}\bar{\bar{x}}^+ \, (\tfrac{\partial f_+^{(o)}}{\partial \bar{\bar{x}}^+})^2 = \begin{cases} \frac{M}{12N} \left(1 - e^{-\frac{\left(\kappa \bar{x}^+ - 1 \right)^2}{w^2}} \right)^4 & \bar{x}^+ > 1 \\[2mm] 0 & \bar{x}^+ < 1 \end{cases}$$ (3.8)

This choice is motivated by the following considerations. First, as in the shell collapse, there is a neighborhood of $\mathcal{I}_{\text{L}}^-$ in which the solution represents the vacuum of the theory. Second, the power 4 on the right side is chosen to ensure high differentiability at $x^+ = 1$

---

[5]The leading order correction $+ (\bar{N} M_{\text{Pl}}/M_{\text{Bondi}})$ to the Hawking flux was obtained by Ori by analytical approximation methods and served as the point of departure for obtaining the fit (3.7). Note also that if the fluxes differ over a significant time interval, it follows that the quantum radiation is not thermal. But the converse is not true as there are *pure* states in the outgoing Hilbert space for which the energy flux at $\mathcal{I}_{\text{R}}^+$ is extremely well approximated by the constant thermal value. For quantum states, what matters is the comparison between the function $y_{\text{sh}}^-(z^-)$ and its classical counterpart $\underline{y}^-(z^-)$ given by (3.1) [13, 17], and these two functions are very different. Finally, non-thermal fluxes were also observed in a quantum model of four-dimensional spherical shell collapse [33]
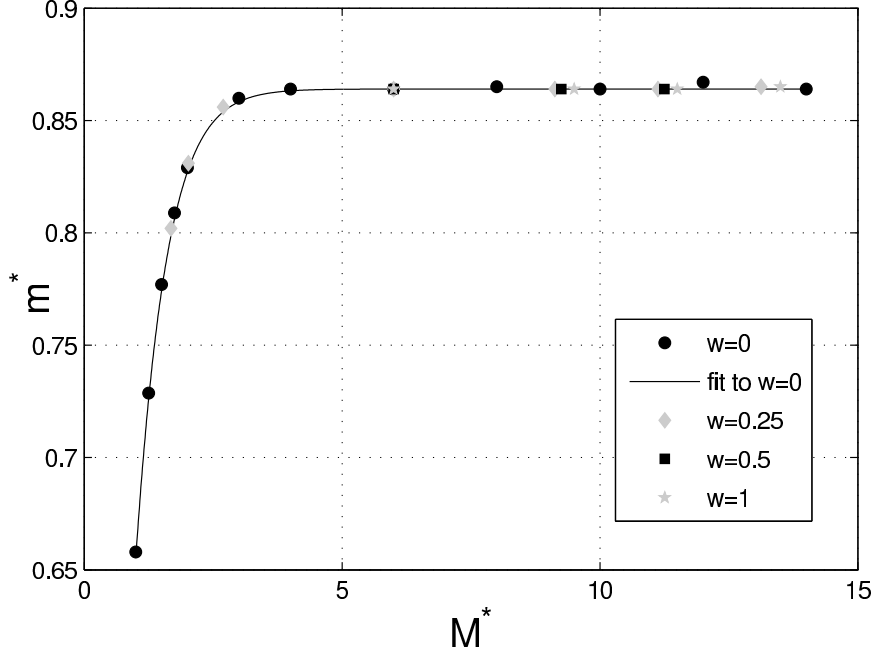
Figure 3.8: The value of $m^\star$ (i.e. $M_{\text{Bondi}}^{\text{ATV}}/\bar{N}$ at the last ray) plotted against $M^\star$ (which equals $M_{\text{ADM}}/\bar{N}$) for $M^\star \geq 1$. In addition to points corresponding to shell collapse ($w = 0$) the plot now includes points with more general profiles with $w = 0.25, 0.5, 1$. The universal value $m^\star \approx 0.864$ persists for $M^\star \geq 4$.

(i.e. $z^+ = 0$). Thus, $f_+^{(o)}$ is $\mathcal{C}^4$ and furthermore decays faster than $e^{-C\kappa z^+}$ for any C as $z^+ \to \infty$. Third, the parameter w provides a measure of the width of the matter profile in x^+ coordinates, which is roughly the width in z^+ for $w \lesssim 1$. Finally, note that we recover the shell profile in the limit $w \to 0$ and expect that the physical requirement of a 'prompt collapse' will be met for sufficiently small w. In the case of a shell profile Eq. 1.34, the parameter M represents the ADM mass. A simple calculation shows that for a general profile in family (3.8), M_{ADM} is given by a function of the two parameters: $M_{\text{ADM}} = M(1 + 1.39\, w)$. Thus, within this family, the issue of universality of a physical quantity boils down to the question of whether it depends only on the specific combination $M(1 + 1.39\, w)$ of the two parameters.

Numerical evolutions were carried out for $M^\star \approx 6, 9, 11, 13$ and $w = 0.25, 0.5, 1$. We find that universality is indeed retained for all these cases. Specifically, we repeated the following analysis of section 3.3 for various values of M and w:
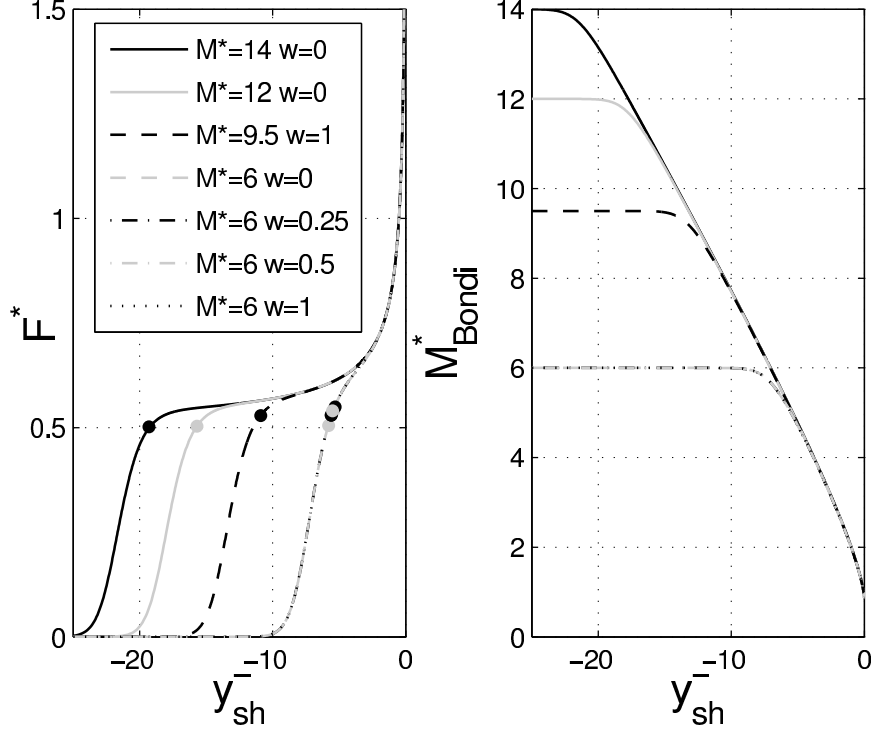
Figure 3.9: F^* (left) and M^*_{Bondi} (right) plotted against y^-_{sh}, for various incoming matter profiles (w and M_{ADM} values), including several shell ($w = 0$) cases. The time when the dynamical horizon first forms is marked on each flux curve (which is later for larger w). All the curves with the same M_{ADM} (6 in this example) are on top of each other and cannot be distinguished by the eye, showing that they have the same universal behavior throughout the evolution, including the early times. More generally all the asymptotic physical quantities depend only on the combination M_{ADM} of the profile parameters M and w as long as κw is small compared to the initial area of the GDH.

i) The relationship between the end-point values $m^\star$ of $M^\star_{\mathrm{Bondi}}$ against $M^\star$; see Fig. 3.8. For $M^\star \geq 4$, we again find $m^\star$ has the same universal value, $\sim .864 M_{\mathrm{Pl}}$.

ii) The relationship of y^- vs $\mathbf{a}^*$ (once GDH becomes time-like). As before, by an appropriate shift, we find a y^-_{sh} that can be used as a universal time coordinate for all cases.

iii) The dependence of $F^\star$ and $M^\star_{\mathrm{Bondi}}$ on $\mathbf{a}^*$ and y^-_{sh}; see Fig. 3.4. We still retain the same notion of universality from the shell collapse, that is, the time evolution of $F^\star$ (and $M^\star_{\mathrm{Bondi}}$) coincide for all values of M and w *at late times*, as long as M_{ADM} is macroscopic, and w is not too wide. Moreover, note that for a fixed value of M_{ADM} the plots are indistinguishable *all the time, including the early times before the formation of the GDH.* That is, asymptotic
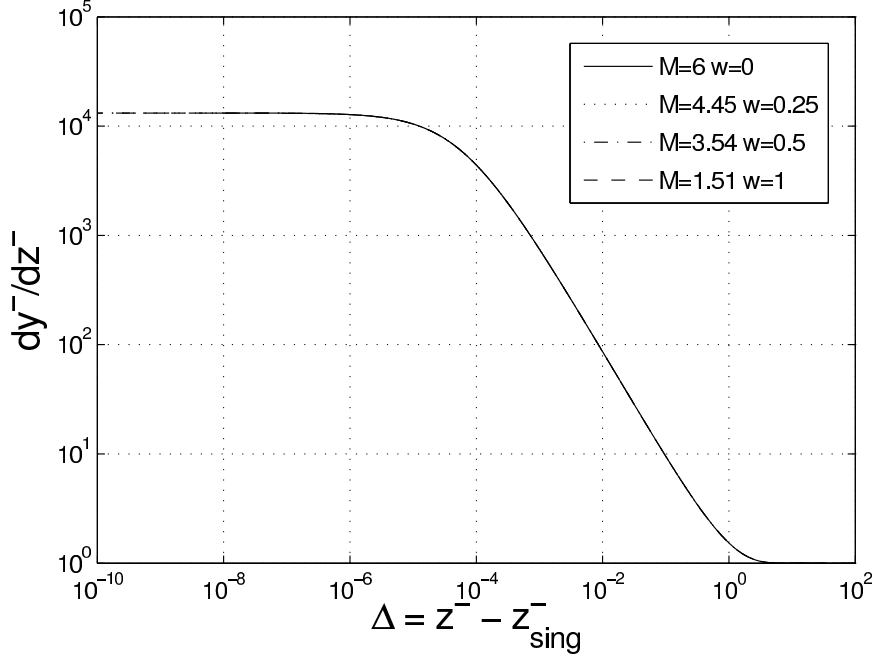
Figure 3.10: Plot of $\mathrm{d}y^-/\mathrm{d}z$ against the separation in z^- from the singularity for various values of M and w with a fixed ADM mass $M^\star = 6$. The functional dependence $y^-(z^-)$ determines the physics of the outgoing quantum state completely [13, 17]. Coincidence of these curves in the mean-field theory suggests that the outgoing quantum state is likely to be universal within the class of initial data with the same ADM mass, so long as the collapse is prompt.

physics near $\mathcal{I}_R^+$ only cares about the "total mass", not the shape of the collapsing energy profile. So, even for this broader class of matter profiles, there are two universal curves, one for the dynamics of $F^\star$ and the other for $M_{\mathrm{Bondi}}^\star$. In particular, for a given $w > 0$, the time evolution $F^\star$ and $M_{\mathrm{Bondi}}^\star$ is identical to that obtained with the shell collapse ($w = 0$).

In the classical theory, if the collapsing matter $f_+^{(o)}$ is compactly supported on $\mathcal{I}_R^-$, to the future of this support the geometry is universal, determined by the ADM mass M_{ADM}. This is because stationary, classical, CGHS black holes are characterized completely by M_{ADM}. Whether the situation would have a direct counterpart in the semi-classical theory is not *a priori* clear because the semi-classical solutions are not stationary and there is no reason to expect the solution to be characterized just by one or two parameters to the future of

the support of $f^{(o)}$. Our results provide a precise sense in which universality does persist. As long as the black hole is initially macroscopic and the collapse is prompt, we have : i) a universal asymptotic time translation $\partial/\partial y_{\mathrm{sh}}^{-}$ (Fig 3.10); and, soon after the formation of the GDH, ii) universal dynamics of physical observables with respect to the physical asymptotic time y_{sh}^{-}.

3.5 Discussion

The CGHS model provides a useful arena to explore the formation and quantum evaporation of black holes. For, the classical action is closely related to that governing the spherically symmetric gravitational collapse in 4 dimensions and, at the same time, the decoupling of matter and dilaton fields in the model introduces significant technical simplification. However, in this paper, we were not concerned with the *full* quantum theory of the CGHS model. Rather, we restricted ourselves to the mean-field equations of [13, 17] and explored their implications using high precision numerics.

Our analysis of universality was carried out in the same spirit that drove the investigation of critical phenomena in classical general relativity [15, 16]. There, one takes equations of general relativity seriously and shows, for example, that black holes can form with arbitrarily small mass. From a more complete physical perspective, these black holes would have enormous Hawking temperature, whence quantum effects would be crucial. To know whether black holes with arbitrarily small masses can form in Nature, one cannot really rely on the classical Einstein equations. The viewpoint in those investigations was rather that, since general relativity is a self-contained, well defined theory, it is interesting to explore what it has to say about such conceptual issues. The results of those explorations led to the discovery of critical behavior in gravitational collapse, which is of great interest from a theoretical and mathematical physics perspective. In the same vein, in the CGHS model, it is conceivable [17] that the relative quantum fluctuations of operators $\hat{\Theta}$, $\hat{\Phi}$, may

become of order 1 once the horizon mass is of the order of, say, $\sqrt{M^\star M_{\text{Pl}}}$.[6] Suppose this were to happen at a point p on the GDH. Then, to the future of the null ray from p to $\mathcal{I}_{\text{R}}^+$, solutions Θ, Φ to the mean-field equations discussed in this paper would be poor approximations of the expectation values of $\hat{\Theta}, \hat{\Phi}$ that result from full quantum equations. That is, our solutions to the mean-field equations would not be *physically* reliable in this future region. The scope of this study did not include this issue of the physical domain of validity of the mean-field approximation. As in much of the literature on semi-classical gravity, we considered the entire space-time domain where the mean-field equations have unambiguous solutions. And as in investigations of critical phenomena, our focus was on exploring non-trivial consequences of these equations. Specifically, we wished to explore two questions: *Are standard expectations about predictions of semi-classical gravity borne out? Do the mean-field dynamics exhibit any universal features?*

---

[6]Note incidentally that in 4 dimensions, when a black hole with $M_{\text{ADM}} = M_\odot$ has shrunk down through quantum radiation to mass $\sqrt{M_{\text{ADM}} M_{\text{Pl}}}$, its horizon radius is less than a fermi, and for a super-massive black hole with $M_{\text{ADM}} = 10^9 M_\odot$, this radius is a tenth of an angstrom.

Chapter 4

Further Discussions and Conclusion

4.1 Semiclassical Theory

We found that some of the standard expectations of semi-classical gravity are indeed borne out: The semi-classical space-time is asymptotically flat at $\mathcal{I}_{\mathrm{R}}^+$ as in the classical theory, but in contrast to the classical case $\mathcal{I}_{\mathrm{R}}^+$ is now *incomplete*. Thus, the expectation [4] that the full quantum space-time would be an extension of the semi-classical one is viable.

However, a number of other expectations underlying the standard evaporation paradigm turned out to be incorrect. Specifically:

a) The traditional Bondi mass $M_{\mathrm{Bondi}}^{\mathrm{Trad}}$ is large and negative at the end of the semi-classical evaporation rather than of Planck size and positive;

b) The recently introduced Bondi mass $M_{\mathrm{Bondi}}^{\mathrm{ATV}}$ remains positive but is large, rather than of Planck size at the end of evaporation;

c) The energy flux F^{ATV} of quantum radiation deviates from the Hawking flux corresponding to thermal radiation even when the black hole is macroscopic, the deviation becoming larger as the evaporation progresses; and,

d) Along the 'last ray' from the end of the singularity to $\mathcal{I}_{\mathrm{R}}^+$, curvature remains finite; there is no 'thunderbolt singularity' in the metric extending to $\mathcal{I}_{\mathrm{R}}^+$.

The analysis also brought out some unforeseen universalities. The most striking among them are:

i) If $M^* = M_{\mathrm{ADM}}/\bar{N}$ is macroscopic, at the end of semi-classical evaporation $m^\star :=$ $M_{\mathrm{Bondi}}^{\mathrm{ATV}}/\bar{N}$ assumes a universal value, $m^\star \approx .864 M_{\mathrm{Pl}}$;

ii) As long as $M^\star$ is greater than M_{pl}, there is a universal relation: $m^\star = \alpha(1 - e^{-\beta(M^\star)^\gamma}) M_{\mathrm{Pl}}$, with $\alpha \approx 0.864$, $\beta \approx 1.42$, $\gamma \approx 1.15$;

iii) An appropriately defined affine parameter y_{sh}^- along $\mathcal{I}_{\mathrm{R}}^+$ is a universal function of the area a_{GDH} of the generalized dynamical horizon;

iv) The evolution of the Bondi mass $M_{\mathrm{Bondi}}^{\mathrm{ATV}}$ with respect to an invariantly defined time parameter $\mathbf{a}_{\mathrm{GDH}}$ (or y_{sh}^-) follows a universal curve (and same is true for the energy flux F^{ATV}).

These results bring out a point that has not drawn the attention it deserves: the number N of fields plays an important role in distinguishing between macroscopic and Planck size quantities. If semi-classical gravity is to be valid in an interesting regime, we must have $N \gg 1$ and the ADM mass and horizon area are macroscopic if $M_{\mathrm{ADM}}/\bar{N} \geq 4 G\hbar M_{\mathrm{pl}}$ and $\mathbf{a}/\bar{N} \geq G\hbar$. (By contrast, it has generally been assumed that the external field approximation should hold so long as $M_{\mathrm{ADM}} > M_{\mathrm{Pl}}$ or $\mathbf{a} > G\hbar$.) Of course the ADM masses can be much larger and for analogs of astrophysical black holes we would have $M_{\mathrm{ADM}}/(\bar{N}M_{\mathrm{pl}}) \gg G\hbar$. After a brief transient period around the time the GDH is born, dynamics of various physical quantities exhibit universal behavior till the horizon area $\mathbf{a}$ goes to zero. If $M_{\mathrm{ADM}}/(\bar{N}M_{\mathrm{pl}}) \gg 1$, the universal behavior spans a huge interval of time, as measured by the physical affine parameter y_{sh}^- on $\mathcal{I}_{\mathrm{R}}^+$ or the horizon area $\mathbf{a}$.

All these features are direct consequences of the dynamical equations Eq. 1.26 and Eq. 1.27 for infalling profiles Eq. 3.8 characterized by two parameters M, w. Of course, with numerical analysis one cannot exhaustively cover the full range of solutions, and given the complete freedom to specify the incoming flux from $\mathcal{I}_{\mathrm{R}}^-$ one can always construct initial data that will not exhibit our universal dynamics —for example, after the GDH is formed,

send in a steady stream of energy with magnitude comparable to F^{ATV}. Here we have restricted attention to initial data for which the GDH forms *promptly*, and is then left to decay quantum mechanically without further intervention. Our intuition is that universality is associated with a *pure quantum decay* of a GDH, pure in the sense that the decay is uncontaminated by continued infall of classical matter carrying positive energy. Therefore, we conjecture that for macroscopic black holes formed by smooth infalling matter profiles of compact support, these universalities will continue to hold soon after the GDH turns time-like. More generally, for profiles in which the positive energy flux carried across the GDH by the classical fields $f_+^{(i)}$ is negligible compared to the negative quantum flux to the future of some ray $z^+ = z_o^+$, the universality should also hold in the future region $z^+ > z_o^+$. Our extended matter profile Eq. 3.8 was of this nature.

This scenario provides a number of concrete and interesting problems for the geometric analysis community. Start with initial data Eq. 1.32, Eq. 1.33 at $\mathcal{I}^-$ with $f_-^{(i)} = 0$ and a smooth profile f_+^o with compact support for each of the N fields $f_+^{(i)}$. Evolve them using Eq. 1.26 and Eq. 1.27. Then, we are led to conjecture that the resulting solution has the following properties:

1) The maximal solution is asymptotically flat at right future null infinity $\mathcal{I}_{\mathrm{R}}^+$;

2) $\mathcal{I}_R^+$ is future incomplete;

3) A positive mass theorem holds: The Bondi mass $M_{\mathrm{Bondi}}^{\mathrm{ATV}}$ is non-negative everywhere on $\mathcal{I}_R^+$;

4) So long as $M_{\mathrm{ADM}} \gg \bar{N} \sqrt{\hbar/G}\,\kappa$, the final Bondi mass (evaluated at the last ray) is given by $M_{\mathrm{Bondi}}^{\mathrm{final}} \approx 0.864 \bar{N} \sqrt{\hbar/G}\,\kappa$;

5) Fix a solution s_o with $M_{\mathrm{ADM}} = M_o \gg N_o \sqrt{\hbar/G}\,\kappa$ and consider the curve c_o describing the time evolution of the Bondi mass in the $\mathbf{a}_{\mathrm{GDH}}/N_o - M_{\mathrm{Bondi}}/N_o$ plane it defines. Then the corresponding curve c for a solution with $M/N < M_o/N_o$ coincides with c_o soon after its GDH becomes time-like.

4.2 Quantum Theory

Although the mean-field approximation ignores quantum fluctuations of geometry, nonetheless our results provide some intuition on what is likely to happen near $\mathcal{I}_{\mathrm{R}}^{+}$ in the full quantum theory. First, because there is no thunderbolt singularity along the last ray, the semi-classical solution admits extensions in a large neighborhood of $\mathcal{I}_{\mathrm{R}}^{+}$ to the future of the last ray. In the mean-field approximation the extension is ambiguous because of the presence of a singularity along which the metric is C^0 but not C^1. But it is plausible that these ambiguities will be resolved in the full quantum theory and there is some evidence supporting this expectation [17, 34]. What features would this quantum extension have? Recall that the model has N scalar fields and the black hole emits quantum radiation in each of these channels. The Bondi mass that is left over at the last ray is $M_{\mathrm{Bondi}} \approx 0.864 \bar{N} M_{\mathrm{Pl}}$. So we have $(0.864/24) M_{\mathrm{Pl}}$ units of mass left over *per channel*. It is generally assumed that this tiny remainder will be quickly radiated away across $\bar{\mathcal{I}}_{\mathrm{R}}^{+}$, the right future null infinity of the quantum space-time that extends beyond the last ray. Suppose it is radiated in a finite affine time. Then, there is a point p on $\bar{\mathcal{I}}_{\mathrm{R}}^{+}$ beyond which $M_{\mathrm{Bondi}}^{\mathrm{ATV}}$ and F^{ATV} both vanish. The expression Eq. 1.42 of F^{ATV} now implies that $\bar{\mathcal{I}}_{\mathrm{R}}^{+}$ is 'as long as' $\mathcal{I}_{\mathrm{L}}^{-}$. This is sufficient to conclude that the vacuum state (of right moving fields $\hat{f}_{-}^{(i)}$) on $\mathcal{I}_{\mathrm{L}}^{-}$ evolves to a pure state on $\bar{\mathcal{I}}_{\mathrm{R}}^{+}$ (because there are no modes to trace over). This is precisely the paradigm proposed in [13]. Thus, the semi-classical results obtained in this paper provide concrete support for that paradigm and re-enforce the analogous 4-dimensional paradigm of [35] (which was later shown to be borne out also in the asymptotically AdS context in string theory [36]).

All our analysis was restricted to the 2-dimensional, CGHS black holes. As we mentioned in Sec. 1.3, while they mimic several features of 4-dimensional black holes formed by a spherical symmetric collapse of scalar fields, there are also some key differences. We will conclude with a list of the most important of these differences and briefly discuss their consequences. (For a more detailed discussion, see [17].)

First, for CGHS black holes, surface gravity κ and hence, in the external field approx-

imation, the Hawking temperature T_{Haw}, is a constant of the theory; it does not depend on the specific black hole under consideration. In 4 dimensions, by contrast, κ and T_{Haw} depend on the black hole. In the spherical case, they go inversely as the mass so one is led to conclude that the black hole gets hotter as it evaporates. A second important difference is that, in the CGHS black hole, matter fields $f^{(i)}$ are decoupled from the dilaton and their propagation is therefore decoupled from the dynamics of the geometric sector. This then implies that the right and left moving modes do not talk to one another. In 4 dimensions, the $f^{(i)}$ are directly coupled to the dilaton and their dynamics cannot be neatly separated from those of geometric fields Φ, Θ. Hence technically the problem is much more difficult. Finally, in 4 dimensions there is only one $\mathcal{I}^+$ and only one $\mathcal{I}^-$ while in 2 dimensions each of them has two distinct components, right and left. Conceptually, this difference is extremely important. In 2 dimensions the infalling matter is only in the plus modes, $f_+^{(i)}$, and its initial state is specified just on $\mathcal{I}_R^-$ while the outgoing quantum radiation refers to the minus modes, $f_-^{(i)}$, and its final state has support only on $\mathcal{I}_R^+$. In 4 dimensions, there is no such clean separation.

What are the implications of these differences?

Because of the first two differences, analysis of CGHS black holes is technically simpler and this simplicity brings out some features of the evaporation process that can be masked by technical complications in 4 dimensions. For instance, since the Hawking temperature T_{Haw} is an absolute constant ($\hbar\kappa$) for CGHS black holes, the standard paradigm that the quantum radiation is thermal till the black hole has shrunk to Planck size leads to a clean prediction that the energy flux should be constant, $F^{\text{Haw}} = \hbar\kappa^2/48$. We tested this simple prediction in the mean field approximation and found that it does not hold even when the horizon area is macroscopic. In 4 dimensions, since the temperature varies as the black hole evaporates, testing the standard paradigm is much more delicate. Similarly, thanks to the underlying technical simplicity in the CGHS case, we were able to discover scaling properties and universalities. We believe that some of them, such as the 'end point

universality', will have counterparts in 4 dimensions but they will be harder to unravel. The CGHS results provide hints to uncover them.

The third difference has deeper conceptual implications which we will now discuss in some detail. In 4 dimensions, since there is a single $\mathcal{I}^-$ and a single $\mathcal{I}^+$, unitarity of the quantum S-matrix immediately implies that all the information in the incoming state can be recovered in the outgoing state. In 2 dimensions, on the other hand, there are two distinct questions: i) is the S-matrix from $\mathcal{I}_{\mathrm{L}}^-$ to $\mathcal{I}_{\mathrm{R}}^+$ unitary? and ii) is the information about the infalling matter on $\mathcal{I}_{\mathrm{R}}^-$ recovered in the outgoing state at $\mathcal{I}_{\mathrm{R}}^+$? As discussed above, results of this paper strongly support the paradigm of [13, 17] in which the answer to the first question is in the affirmative; information on $\mathcal{I}_{\mathrm{L}}^-$ is faithfully recovered on $\mathcal{I}_{\mathrm{R}}^+$. However, this does *not* imply that all the infalling information at $\mathcal{I}_{\mathrm{R}}^-$ is imprinted on the outgoing state at $\mathcal{I}_{\mathrm{R}}^+$.

In the early CGHS literature, this second issue was often mixed with the first one. Because it was assumed that all (or at least most) of the ADM mass is evaporated away through quantum radiation, it seemed natural to consider seriously the possibility that all the information in the infalling matter at $\mathcal{I}_{\mathrm{R}}^-$ can be recovered from the outgoing quantum state at $\mathcal{I}_{\mathrm{R}}^+$. The key question was then to find mechanisms that make it possible to transfer the information in the *right-moving* infalling modes $f_+^{(i)}$ to the *left-moving* modes $f_-^{(i)}$ going out to $\mathcal{I}_{\mathrm{R}}^+$. In [22], for example, the 2-dimensional Schwinger model with a position dependent coupling constant was discussed in some detail to suggest a possible mechanism.

However, our universality results strongly suggest that these attempts were misdirected. The physical content of the outgoing *quantum* state is encoded entirely in the function $y_{\mathrm{sh}}^-(z^-)$ [13, 17] on $\bar{\mathcal{I}}_{\mathrm{R}}^+$, the right future null infinity of the quantum extension of the semi-classical space-time. In the family of profile functions $f_+^{(o)}$ we analyzed in detail, the function $y_{\mathrm{sh}}^-(z^-)$ on $\mathcal{I}_{\mathrm{R}}^+$ has universal behavior, determined just by the total ADM mass. Since only a tiny fraction of Planck mass is radiated per channel in the portion of $\bar{\mathcal{I}}_{\mathrm{R}}^+$ that is not already in $\mathcal{I}_{\mathrm{R}}^+$, it seems highly unlikely that the remaining information can be encoded in

the functional form of $y^-_{\mathrm{sh}}(z^-)$ in that portion. Thus, at least for large $M^\star$ we expect the answer to question ii) to be in the negative: information contained in the general infalling matter profile on $\mathcal{I}^-_{\mathrm{R}}$ will *not* be fully recovered at $\mathcal{I}^+_{\mathrm{R}}$. From our perspective, this is not surprising because the structure of null infinity in the CGHS model is rather peculiar from the standpoint of 4 dimensions where much of our intuition is rooted. In 2-dimensional models, $\bar{\mathcal{I}}^+_{\mathrm{R}}$ is not the *full* future boundary of space-time. Yet discussions of CGHS black holes generally ignore $\mathcal{I}^{o+}_{\mathrm{L}}$ because, as we saw in section 1.3.4, even in the classical theory the black hole interpretation holds only with reference to $\mathcal{I}^+_{\mathrm{R}}$. Indeed, for this reason, investigations of quantum CGHS black holes have generally focused on the Hawking effect and question i) of unitarity, both of which involve dynamics only of $\hat{f}^{(i)}_-$ for which $\bar{\mathcal{I}}^+_{\mathrm{R}}$ does effectively serve as the complete future boundary.

In 4 dimensions, the situation is qualitatively different in this regard: in particular, the outgoing state is specified on all of future null infinity $\mathcal{I}^+$, not just on half of it. Therefore, if the singularity is resolved in the full quantum theory, $\bar{\mathcal{I}}^+_{\mathrm{R}}$ *would* be the complete future boundary of the quantum space-time and there would be no obstruction for the S matrix to be unitary and hence for the full information on $\mathcal{I}^-$ to be imprinted in the outgoing state on $\mathcal{I}^+$.

Appendix A

Mass dependence of the energy flux

A.1 Flux-Mass Relationship

In Sec. 3.3, we gave a formula that connects the ATV definition of the energy flux with the Bondi mass, namely

$$F^{\text{ATV}} = F^{\text{Haw}} \left[1 - \ln \left(1 - \frac{\bar{N} M_{\text{Pl}}}{M_{\text{Bondi}}^{\text{ATV}}} \right) \right]. \tag{A.1}$$

Recall that Eq. A.1 only holds in the interval between the formation of the GDH and the time when $M_{\text{Bondi}}^{\text{ATV}}$ approaches $\bar{N} M_{\text{Pl}}$, that is not too early on and not too close to the last ray. Let us briefly explain how this formula, or rather, conjecture, was devised.

We start with the idea that F^{ATV} can be expressed as a series in inverse Bondi mass

$$F^{\text{ATV}} = F^{\text{Haw}} \left[1 + \sum_{i=1}^{\infty} a_i \left(\frac{\bar{N} M_{\text{Pl}}}{M_{\text{Bondi}}^{\text{ATV}}} \right)^i \right]. \tag{A.2}$$

The $i = 1$ term was suggested to us by Amos Ori in a private communication, and was soon confirmed by our numerical results. We found the higher order coefficients term by term. Once the nth order term (in the expansion parameter $\frac{\bar{N} M_{\text{Pl}}}{M_{\text{Bondi}}^{\text{ATV}}}$) is determined, let us call the approximation to F^{ATV} that contains these n terms F_n^{ATV}. We plot

$\bar{a}_i = \left(\frac{\bar{N} M_{\text{Pl}}}{M_{\text{Bondi}}^{\text{ATV}}} \right)^{n+1} \left[F^{\text{ATV}} - F_{(n)}^{\text{ATV}} \right]$, which should be roughly constant in the range where the series expansion holds, and this was confirmed in our numerical studies.

For up to $i = 4$ we made the observation that $\bar{a}_i \approx \frac{1}{i}$. Based on this, rather than going through a detailed numerical analysis, which is further complicated by the fact that the formula holds only in a certain interval, we conjectured that $a_i = \frac{1}{i}$, not only for the first few terms, but in general. This is simply the series expansion of Eq. A.1. In summary, Eq. A.1 is a combination of concrete numerical results up to $i = 4$, and a conjecture based on these results for the full series expansion. We should note that relative error grows as one tries to determine a_i for higher i. $i = 4$ was the highest value where we could discern a_i.

A.2 Flux-Mass Relationship for the "Traditional" Definitions

Dori and Ori (DO from here on) recently gave a series expansion very similar to eq. A.2, but instead of the ATV definitions, they used the traditional definitions of the Bondi mass and the energy flux [37]. In this section, we show that their results can be analytically obtained from Eq. A.1

Before we proceed, let us simplify our notation to avoid any confusion that might arise due to the differences between our approach and that of DO. We will work with dimensionless quantities and also scale them with the number of quantum fields present, $\bar{N} = N/24$,

as before

$$
\begin{aligned}
m &= M_{\text{Bondi}}^{\text{ATV}}/(\bar{N}M_{\text{Pl}}), \\
f &= F^{\text{ATV}}/(\bar{N}F_{\text{Pl}}), \\
m_{Trad} &= M_{\text{Bondi}}^{\text{Trad}}/(\bar{N}M_{\text{Pl}}), \\
f_{Trad} &= F^{\text{Trad}}/(\bar{N}F_{\text{Pl}}), \tag{A.3}
\end{aligned}
$$

where F_{Pl} is the Planck flux given by $\hbar\kappa^2$. Using these quantities, eq. A.1 now reads as

$$
f = \frac{1}{2}\left[1 - \ln\left(1 - m^{-1}\right)\right] = \frac{1}{2}\left[1 + \sum_{i=1}^{\infty} \frac{1}{i\,m^i}\right]. \tag{A.4}
$$

The result of DO is given by

$$
f_{Trad} = \frac{1}{2}\left[1 + \sum_{i=1}^{\infty} c_i \left(\frac{1}{m_{Trad}}\right)^i\right] \tag{A.5}
$$

where they numerically found that $c_2 = 0$ and $c_3 \approx -0.4$, the latter with 25% error. We will call this the DO formula.

Since the "traditional" and ATV definitions of the Bondi mass and the energy flux are related by analytic expressions, any c_i in A.5 can be, in principle, calculated from A.4. At the base of converting the DO formula to ours is the formula

$$
\begin{aligned}
f_{Trad} &= f + \sqrt{2}\frac{\mathrm{d}\sqrt{f}}{\mathrm{d}y^-} \\
&= f - \frac{1}{\sqrt{2}}\sqrt{f}\frac{df}{dm} \\
&= f + \frac{1}{2^{3/2}}\sqrt{f}\frac{\left(1 - e^{1-2f}\right)^2}{e^{1-2f}}. \tag{A.6}
\end{aligned}
$$

The first line is a trivial observation on Eq.1.42 and Eq. 1.45, on the second line we used eq. 1.43.

Since in both cases, the Bondi mass is given by integrating the corresponding flux, and both the "Traditional" and ATV Bondi masses agree at the infinite past ($z^- \to -\infty$), simple integration of the first line of Eq. A.6 gives

$$
\begin{aligned}
m_{Trad} &= m - \sqrt{2}\sqrt{f} \\
&= m - \left[1 - \ln\left(1 - m^{-1}\right)\right]^{1/2} ,
\end{aligned}
\tag{A.7}
$$

where we used Eq. A.1 in the second line. Thus, "Traditional" quantities can be expressed in terms of their ATV versions by inverting Eq. A.6 and Eq. A.7. Functions that relate the traditional and ATV quantities do not have trivial inverses, so we will invert their series expansion order by order up to m_{Trad}^{-4}.

We first express m^{-1} in terms of m_{Trad}^{-1}, using Eq. A.7

$$
m^{-1} = m_{Trad}^{-1} - m_{Trad}^{-2} + \frac{3}{8}m_{Trad}^{-3} - \frac{53}{48}m_{Trad}^{-4} + \mathcal{O}(m_{Trad}^{-5})
\tag{A.8}
$$

Using Eq. A.6, we can write f_{Trad} in terms of m, since f is known in terms of m:

$$
f_{Trad} = \frac{1}{2}\left[1 + m^{-1} + m^{-2} + \frac{13}{12}m^{-3} + \frac{17}{16}m^{-4} + \mathcal{O}(m^{-5})\right] .
\tag{A.9}
$$

Inserting Eq. A.8 into Eq. A.9, we finally reach

$$
f_{Trad} = \frac{1}{2}\left[1 + m_{Trad}^{-1} - \frac{5}{12}m_{Trad}^{-3} + \frac{3}{16}m_{Trad}^{-4} + \mathcal{O}(m_{Trad}^{-5})\right] ,
\tag{A.10}
$$

which recovers $c_2 = 0$ and $c_3 = -5/12 \approx -0.4$, results of DO. We should emphasize that, even though we only performed our calculation up to the 4th order, the coefficient at any order can be calculated with ease. On the other hand, one should also remember that only terms up to the 4th order are based on numerical results, higher terms are part of a conjecture.

Quantitative relations between the energy flux and the mass is important in establishing the fact that the energy flux is not thermal, and might be useful in finding quantitative measures of the difference from the thermal case in the mean-field approximation.

Bibliography

[1] A. Ashtekar, F. Pretorius and F. M. Ramazanoğlu, Evaporation of 2-Dimensional Black Holes, *Phys. Rev.* D83:044040 (2011)

[2] A. Ashtekar, F. Pretorius and F. M. Ramazanoğlu, Surprises in the Evaporation of 2-Dimensional Black Holes, *Phys. Rev. Lett.* 106:161303 (2011)

[3] F. M. Ramazanoğlu and F. Pretorius, Two-dimensional quantum black holes: Numerical methods, *Class. Quantum Grav.* 27:245027 (2010)

[4] S. W. Hawking, Particle creation by black holes, *Commun. Math. Phys.* 43:199-220 (1975)

[5] V. Mukhanov, S. Winitzki, Introduction to Quantum Effects in Gravity, Cambridge University Press (2007)

[6] N. D. Birrell, P. C. W. Davies, Quantum Fields in Curved Space, Cambridge University Press (1984)
R. M. Wald, Quantum Field Theory in Curved Spacetime and Black Hole Thermodynamics, University of Chicago Press (1994)

[7] J. D. Brown, Lower dimensional gravity, World Scientific (1988)

[8] C. G. Callan, S. B. Giddings, J. A. Harvey and A. Strominger, Evanescent black holes, *Phys. Rev.* D45, R1005-R1009 (1992).

[9] S. B. Giddings and A. Strominger, Dynamics of extremal black holes, *Phys. Rev.* D46:627 (1992); Quantum theories of dilaton gravity, *Phys. Rev.* D47:2454(1993);

J. G. Russo, L. Susskind and L. Thorlacius, Black hole evaporation in 1+1 dimensions, *Phys. Lett.* B292:13 (1992);

A. Strominger, Faddeev-Popov ghosts and $(1 + 1)$-dimensional black-hole evaporation, *Phys. Rev.* D46:4396 (1992);

S. P. de Alwis, Black hole physics from Liouville theory, *Phys. Lett.* B300:330 (1993); *Phys. Rev.* D46:5429 (1992)

G. Mandal, A. M. Sengupta and S. R. Wadia, Classical solutions of 2-dimensional string theory, *Mod. Phys. Lett.* A6:1685-1696 (1991)

E. Witten, String theory and black holes, *Phys. Rev.* D44:314-324 (1991)

[10] T. Piran and A. Strominger, Numerical analysis of black hole evaporation, Phys. Rev. D **48**, 4729-4734 (1993)

[11] D. A. Lowe, Semiclassical approach to black hole evaporation, *Phys. Rev.* D47:2446 (1993);

[12] S. B. Giddings, Quantum mechanics of black holes, `arXiv:hep-th/9412138`; A. Strominger, les Houches lectures on black holes, `arXiv:hep-th/9501071`

[13] A. Ashtekar, V. Taveras and M. Varadarajan, Infornmation is not lost in the evaporation of 2-dimensional black holes, *Phys. Rev. Lett.* 100:211302 (2008)

[14] R. P. Geroch and G. T. Horowitz, Asymptotically simple does not imply asymptotically Minkowskian, *Phys. Rev. Lett.* 40:203-206 (1978)

[15] M. Choptuik, Universality and scaling in gravitational collapse of a massless scalar field, *Phys. Rev. Lett.* 70:9 (1993).

[16] C. Gundlach and J. M. Martin-Garcia, Critical phenomena in gravitational collapse, *Living. Rev. Rel.* 10:5 (2007)

[17] M. Varadarajan, A. Ashtekar and V. Taveras (pre-print, 2010)

[18] S. Hayward, Cosmic censorship in 2-dimensional dilaton gravity, *Class. Quant. Grav.* 10:985-994 (1993).

[19] A. Ashtekar and B. Krishnan, Isolated and dynamical horizons and their applications, *Living. Rev. Rel.* 7:10 (2004)

[20] A. Ashtekar and B. Krishnan, Dynamical horizons: Energy, angular momentum and balance laws, *Phys. Rev. Lett.* 89:261101 (2002); Dynamical horizons and their properties, *Phys. Rev.* D68:104030 (2003)

[21] D. A. Lowe, Semiclassical approach to black hole evaporation, *Phys. Rev.* D47:2446-2453 (1993)

[22] L. Susskind and L. Thorlacius, Hawking radiation and back reaction, *Nucl. Phys.* B382:123-147 (1992)

[23] T. Tada and S. Uehara, Consequences of Hawking radiation from 2-d dilaton black holes, *Phys. Rev.* D51:4259-4264 (1995)

[24] S. W. Hawking and J. M. Stewart, Naked and thunderbolt singularities in black hole evaporation, *Nucl. Phys.* B400:393-415 (1993)

[25] A. Ori, Approximate solution to the CGHS field equations for two-dimensional evaporating black holes, *Phys. Rev.* D82:104009 (2010)

[26] D. Yeom and H. Zoe, Semi-classical black holes with large N re-scaling and information loss problem `arXiv:0907.0677v1`.

[27] J. Winicour, Characteristic Evolution and Matching, *Living. Rev. Rel.* 1:5 (1998) [arXiv:gr-qc/0102085].

[28] J. G. Russo, L. Susskind and L. Thorlacius, The Endpoint of Hawking radiation, *Phys. Rev.* D46:3444 (1992)

[29] A. Bilal and C. G. . Callan, Liouville models of black hole evaporation, *Nucl. Phys.* B394:73 (1993)

[30] A. Strominger, Unitary rules for black hole evaporation, `arXiv:hep-th/9410187`

[31] H. Bondi, M. G. J. Van den Berger, and A. W. K. Metzner, Gravitational waves in general relativity VIII. Waves from axi-symmetric islated systems, *Proc. Roy. Soc.* (London) A269:21-52 (1962)

[32] S. B. Giddings and W. M. Nelson, Quantum emission of 2-dimensional black holes, *Phys. Rev.* D46:2486-2496

[33] T. Vachaspati and D. Stojkovic, Quantum radiation from quantum gravitational collapse, *Phys. Lett.* B663:107 (2008)

[34] D. Levanony and A. Ori, Interior design of a two-dimensional semiclassical black hole: Quantum transition across the singularity, *Phys. Rev.* D81:104036 (2010)

[35] A. Ashtekar and M. Bojowald, Black hole evaporation: A paradigm, *Class. Quant. Grav.* 22:3349-3362 (2005)

[36] G. Horowitz, A. Lawrence and E. Silverstein, Insightful D-branes, *JHEP* 0907:057 (2009)

[37] L. Dori and A. Ori, Finite-mass correction to 2D black-hole evaporation rate, `arXiv:1201.6386v1`